Predictions of helical twisting powers and molecular chirality

Earl, David James

Predictions of Helical Twisting Powers and Molecular Chirality

David James Earl

Ph.D. Thesis

University of Durham

Chemistry Department

September 2003

Submitted in partial fulfilment of the requirements

for the degree of Doctor of Philosophy

Abstract

Predictions of helical twisting powers and molecular chirality

David James Earl

Ph.D. 2003

When chiral molecules are added to an achiral nematic liquid crystalline solvent, they can transmit their molecular chirality to the whole system over distances many times their molecular length. The helical twisting power, β_M, is a measure of the degree of twist a chiral molecule can induce in a nematic liquid crystal. The work in this thesis is primarily concerned with calculating helical twisting powers for a variety of chiral molecules using computational and theoretical methods.

The first technique used to calculate β_M employed Monte Carlo simulations of an atomistic chiral dopant molecule in a chiral liquid crystal phase composed of generic liquid crystalline molecules. The method was found to be computationally expensive, but provided reasonable predictions of β_M when compared with experimental results. Prior to these calculations, a liquid crystal solvent for use in this method was studied. Computer simulations of $L/D = 4$ soft repulsive spherocylinder (SRS) molecules were performed and two liquid crystalline phases were found in the SRS phase diagram.

The scaled chiral index and the chirality order parameter are quantitative measures of molecular chirality. Both of these methods have been found to show a good correlation with experimentally determined helical twisting powers of relatively rigid chiral molecules. The chiral measures have also been incorporated in Monte Carlo simulations of flexible chiral molecules. This method has been successful in predicting β_M for flexible chiral dopants, in predicting the temperature dependence of β_M, has demonstrated a temperature induced helical twist inversion, and has been used in a predictive study to aid in future synthetic strategies.

The final part of the thesis uses Monte Carlo simulations of a chiral molecule in an achiral liquid crystal phase. These simulations have shown that it is possible to relate the torque the chiral molecule induces in the solvent to β_M.

Declaration

The material contained within this thesis has not previously been submitted for a degree at the University of Durham or any other university. The research within this thesis has been conducted by the author unless indicated otherwise.

David James Earl

September 2003

Acknowledgments

I have a great many people to thank for the help and support I have received over the last three years. Firstly, I would like to thank the Engineering and Physical Sciences Research Council (EPSRC) for a quota award and Merck NB-C for a CASE award, thus allowing the research to take place. I would like to gratefully acknowledge funding from the Royal Society of Chemistry and the British Liquid Crystal Society to enable me to attend many interesting conferences and to give me the opportunity to meet and talk with fellow researchers. I am particularly grateful for the valuable discussions I have had with Prof. Maureen Neal (Coventry and Manchester Metropolitan), Prof. John Goodby (Hull) and Prof. Mike Allen (Warwick) during my PhD.

Within the University of Durham I must thank Dr Lydia Heck, Dr Karen Brazier, Dr Duncan Rand and the Information Technology Service for computational support. For help in the production of this thesis, I acknowledge M. Imran for the original Lyx template and Lorna Stimson for answering my many and varied questions on word-processing related topics.

Dr Dorothy Catling deserves a special mention for the support, friendship and encouragement she has given me during my six years in Durham.

Dr Mark Wilson, my PhD supervisor, deserves the greatest thanks here. I have enormous respect for Mark as a scientist and as a friend. Mark has created a research group in Durham that has a fantastic atmosphere, produces good science, and is a great pleasure to work in. Within Mark's Computational Chemistry group, I would like to thank all of my colleagues over the last three years including Lorna Stimson, Jaroslav Ilnytskyi, Dave Cheung, Phil Anderson, Melanie Cook and Zak Hughes.

I have a great many friends that I have shared happy times with during my time at Durham and at home in Leicester growing up. Among others, these include Alex, Paul, Tim, Kev, Dave, G'Dave, Jane, Dan, Caz, Tom, Graeme, Jim and Rich, and all the members of Trevelyan College football and cricket teams over the years. Leicester City also deserve a mention for taking me through many highs and lows including League Cup triumph (twice!), relegation and, most recently, promotion back to the Premiership.

All of my family have provided constant love and support during my life, especially Mum, Dad, Jon, my Grandparents, Sandra and Haydn, Gary, and my cousins Rebecca and Nicholas, and with her love, friendship, support and consideration, my wife, Kath, has made the last few years the most wonderful of my life.

Computers are incredibly fast, accurate, and
stupid. People are incredibly, slow,
inaccurate, and brilliant.
Together, they are just incredible!

Albert Einstein

Contents

List of Figures

List of Tables

Chapter 1

Introduction to Liquid Crystals and Chirality

1.1 Liquid Crystals

Liquid crystalline phases occur between the solid crystalline state and the isotropic liquid state. In a crystalline solid, the molecules are arranged at regular, repeating lattice points and the degree of both orientational and positional order is high. In contrast, in an isotropic liquid, the molecules are free to rotate and translate and have no orientational or positional order. In liquid crystalline materials, one or several intermediate phases (or mesophases) exist between the solid and the liquid phase. While being less dense than the solid state, these phases retain a certain degree of ordering. However, they also share some of the disordered, fluid-like properties of liquids and so they are known as liquid crystalline phases.

1.1.1 Historical Context

The discovery of liquid crystals is generally credited to Friedrich Reinitzer, an Austrian botanist, who in 1888 published work describing the "double melting" behaviour of cholesteryl benzoate.[1] Upon melting the crystal at 145.5°C, Reinitzer observed that a cloudy fluid was formed (a cholesteric or chiral nematic phase) and that at 178.5°C the fluid became clear (an isotropic liquid). Reinitzer sent his sam-

ples to Otto Lehmann, a German physicist, who in 1889 confirmed the existence of this new phase of matter.[2] Lehmann wrote that "it is of great interest for the physicist that crystals can exist with a softness, being so considerable that one could call them nearly liquid." In his work of 1889,[2] Lehmann used the term liquid crystal to describe the intermediate phase for the first time.

Following the discovery, many more materials were found to display liquid crystalline phases.[3,4] However, some scientists doubted that these were new phases and instead suggested that they were colloidal suspensions or mixtures of tautomers, until the important contributions to the subject made by Georges Friedel. Published in 1922, his work was the first to classify liquid crystals into different types; namely nematic, smectic and cholesteric (chiral nematic) phases.[5] Around the same time, synthetic studies of new liquid crystalline materials were being made[6] which, coupled with Friedel's work, put an end to doubts as to the existence of liquid crystalline phases.

1.1.2 Classification of Liquid Crystals

Liquid crystalline materials can be divided into two main classes; namely thermotropic and lyotropic materials. In thermotropic liquid crystals the phase transition from a non-liquid crystal phase to a liquid crystal phase is the result of a thermal process whereas in lyotropic liquid crystals the liquid crystal phases result from the addition of a solvent, usually water, to a solute, usually an amphiphile. The transitions in lyotropic liquid crystals are strongly dependent on the concentration of the solvent as well as on the temperature.

Thermotropic Liquid Crystals

Thermotropic liquid crystals are generally formed by rod-shaped (calamitic) and discotic molecules. Following Friedel's classification,[5] liquid crystal phases formed by rod-like molecules can be grouped into three main categories: nematic, chiral nematic (cholesteric) and smectic phases.

Nematic Phase

In the nematic liquid crystalline phase the orientations of the long molecular axes of the constituent molecules are preferentially aligned. This direction of preferential alignment is known as the director and is denoted by **n**, a unit vector (see figure 1.1). This phase has a high degree of orientational order but contains no long-range translational order, and thus nematics are fluid and have viscosities of approximately the same magnitude as the isotropic liquid phase. The degree of orientational order

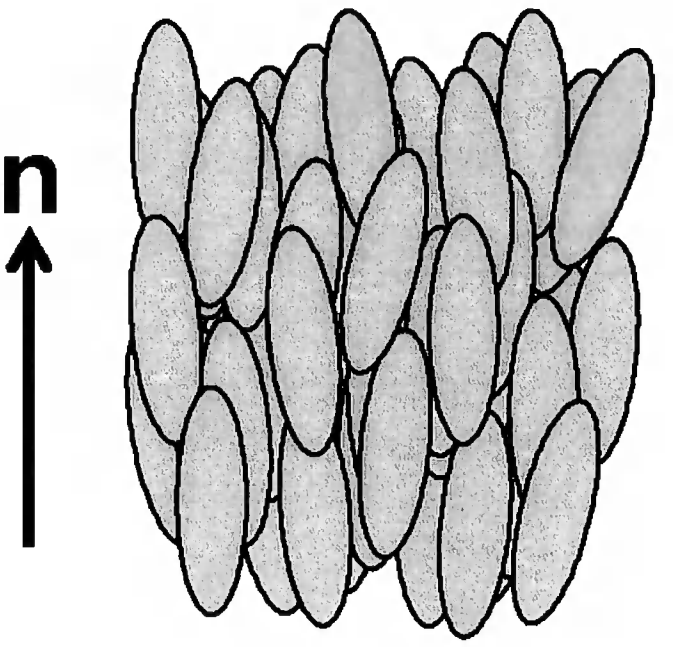

Figure 1.1: Schematic diagram of a typical nematic phase where **n** is the director. Molecular shape is approximated by an ellipsoid.

can be characterised by the order parameter, S_2, given by

$$S_2 = \left\langle \frac{3}{2}\cos^2\theta - \frac{1}{2} \right\rangle, \tag{1.1}$$

where θ is the angle the long molecular axis of each molecule makes with the director, **n** (see figure 1.2), and the angular brackets denote an average over all the molecules. Typical nematic order parameters are in the region of $S_2 \approx 0.4$-0.8. An isotropic liquid phase with no orientational order has $S_2 = 0$.

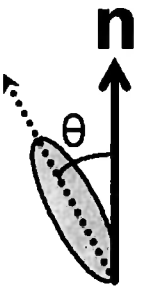

Figure 1.2: Relationship between the director, **n**, and θ in equation 1.1.

Chiral Nematic Phase

The chiral nematic (or cholesteric) phase is locally similar to the nematic phase. However, the structure undergoes a periodic helical distortion which results in the director, **n**, varying in space about a helical axis (by convention the z-axis) with a pitch of $P = \frac{2\pi}{k}$ (see figure 1.3) such that **n** takes the form

$$\mathbf{n} = \begin{pmatrix} \cos\theta(z) \\ \sin\theta(z) \\ 0 \end{pmatrix},$$

where

$$\frac{d\theta}{dz} = k, \tag{1.2}$$

and k is a constant denoted as the wavevector of the chiral nematic phase. Chiral nematics are discussed further in section 1.2.3.

Smectic Phases

Smectic mesophases contain both orientational order and a degree of translational order.[7] Smectic phases are layered structures and display a greater degree of orientational order than the nematic phase (for smectic phases $S_2 > 0.8$), but the molecules have no translational periodicity between the layers and in the planes of the layers. There are a number of different classes of smectic phase structures such as A, B, C, F and I. These classes vary in the degree of order they possess and in the

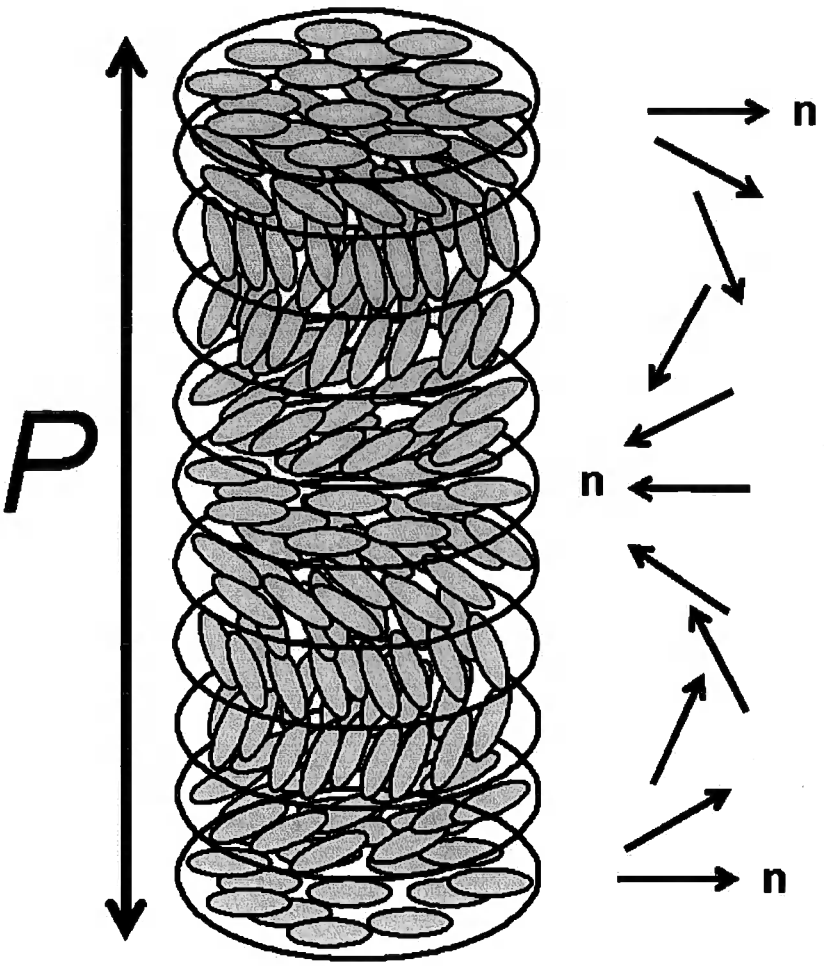

Figure 1.3: Schematic diagram of a chiral nematic phase with a pitch of P.

tilt angle of the individual layers. In the smectic-A phase (see figure 1.4a) the long axes of each of the molecules are aligned approximately perpendicular to the layers while the layers themselves are disordered. In the smectic-C phase the molecules are aligned at a temperature dependent tilt angle (θ in figure 1.4b) to the normal of the layer planes. As in the smectic-A phase, the layers are diffuse.

Order of Phase Transitions in Rod-Shaped Molecules

In rod-shaped molecules, upon melting the solid by increasing the temperature, liquid crystalline phases occur with decreasing order (and hence order parameter) until the transition to the completely disordered isotropic liquid phase occurs. Figure 1.5 shows the melting process for a rod-shaped liquid crystalline material. The figure shows three liquid crystalline phases for a material with solid, smectic-C, smectic-A, nematic and isotropic phases (K-SmC-SmA-N-I). Some materials may not possess all or any of these phases and some of these cases are also shown in the figure (K-SmA-N-I, K-N-I and for a non-liquid crystalline material K-I).

Discotic Liquid Crystal Phases

Liquid crystalline phases can also be formed by disc-like particles.[8] Discotic molecules can form nematic discotic (see figure 1.6a), chiral nematic discotic and columnar (see figure 1.6b) phases. In the columnar phase, the discs within the columns are disordered while the columns form a two-dimensional lattice.

Lyotropic Liquid Crystals

Lyotropic liquid crystals are formed when amphiphiles are mixed with a polar solvent, which is usually water.[9] Amphiphiles are normally composed of a hydrophilic polar head-group and a hydro-phobic non-polar alkyl tail (see figure 1.7). The concentration of the amphiphile and the solvent, and also the temperature of the system determine phase transitions. The major classes of lyotropic liquid crystal phases are the lamellar, hexagonal and the cubic phase (see figure 1.8a-c). Lyotropic liquid crystals find applications in everyday use such as in detergents, soaps, shampoos, cosmetic items such as skin cream, and in food products such as in frozen desserts.

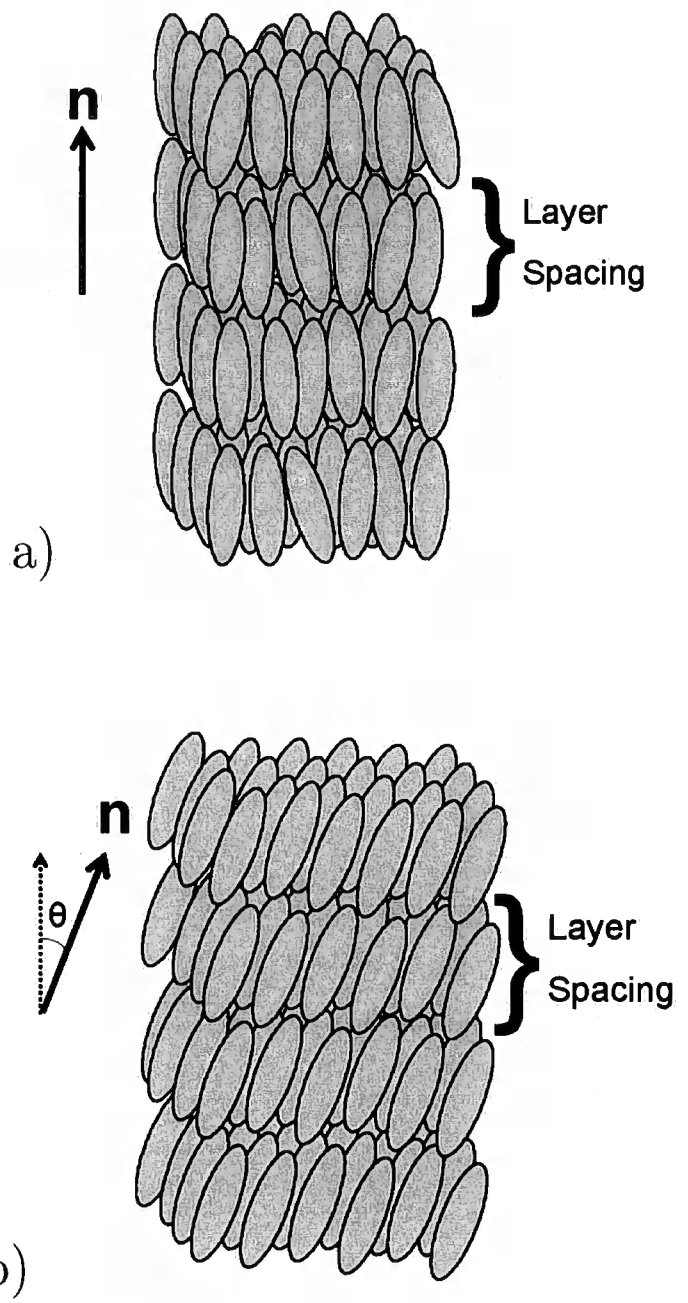

Figure 1.4: Schematic diagrams of a) the smectic-A phase and b) the smectic-C phase where θ is the tilt angle.

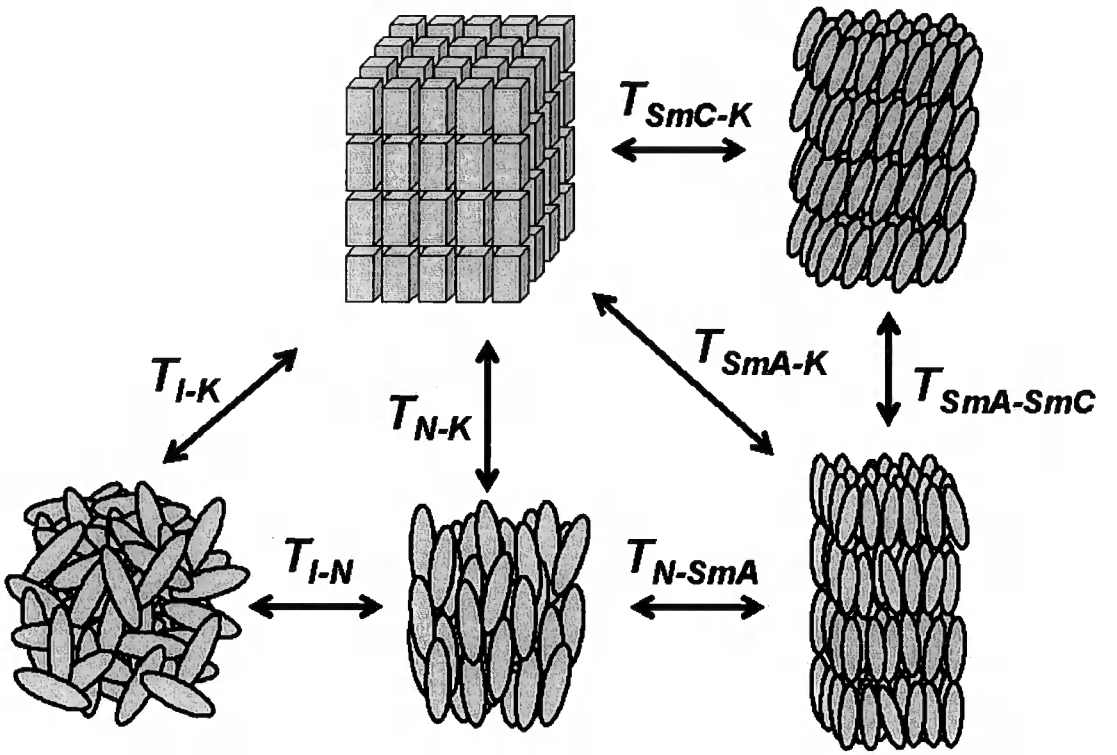

Figure 1.5: Typical melting process for various liquid crystalline and non-liquid crystalline rod-shaped molecules. T_{A-B} denotes the transition temperature for the transition from phase A to phase B.

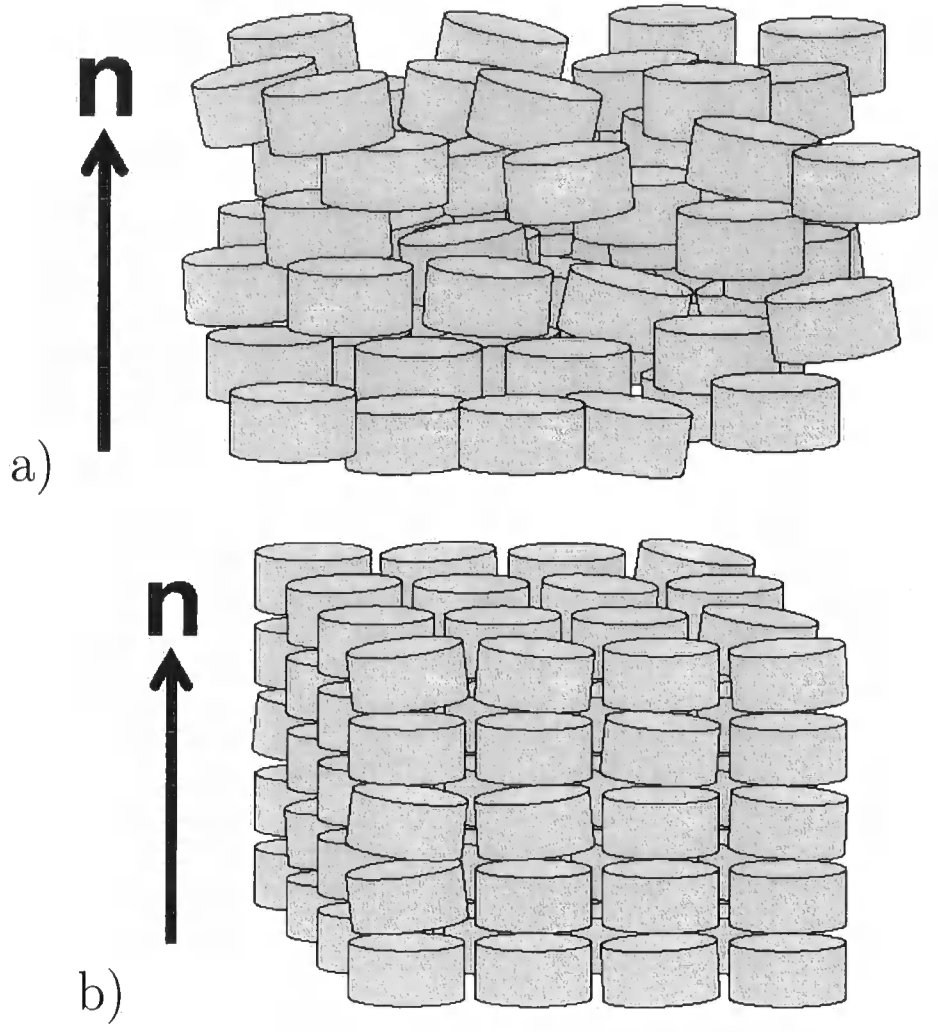

Figure 1.6: Schematic diagrams of a) the nematic discotic phase and b) the columnar phase.

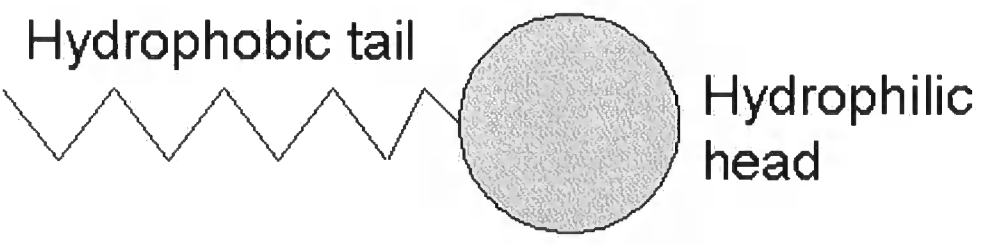

Figure 1.7: General form of an amphiphile.

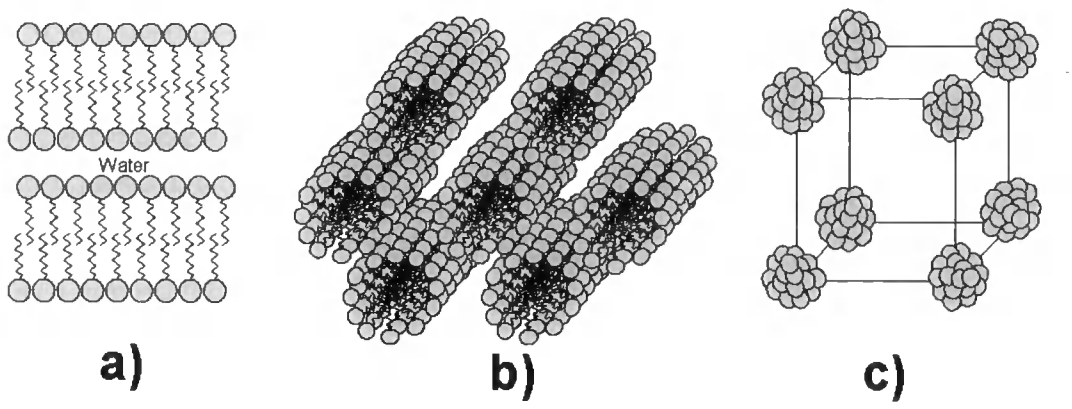

Figure 1.8: Examples of lyotropic liquid crystal phases a) lamellar b) hexagonal and c) cubic.

1.2 Chirality

1.2.1 Historical Context

In his *Baltimore Lectures on Molecular Dynamics and the Wave Theory of Light*, Lord Kelvin defined chirality[10] when he said, "I call any geometrical figure, or group of points, chiral, and say that it has chirality if its image in a plane mirror, ideally realized, cannot be brought to coincide with itself." One hundred years later, this is still the most commonly used definition of chirality. Lord Kelvin was certainly not the first scientist to observe chirality though. In 1811 Francois Arago[11] discovered the rotation of the polarization of light by quartz crystals and in 1835 Jean-Baptiste Biot[12] discovered the same phenomenon by a sugar solution. Louis Pasteur probably made the most significant early observation of chirality in 1848 when he noticed that a salt of tartaric acid formed two different types of crystal that were mirror images of each other.[13] Pasteur was able to separate the two different types into solutions and he found that one of the solutions rotated plane polarized light clockwise while the other solution rotated it anti-clockwise.

Although these were the first scientific observations of chirality, it is interesting to note that the chiral properties of structures had been utilised for many centuries prior to these discoveries. For example, Archimedes of Syracuse used the chiral

properties of spiral structures in the design of his famous water screw in approximately 250 BC. Also, medieval architects were well aware of the practical uses of chiral structures when they designed left-handed helical staircases in turrets and towers. They realised that soldiers defending the staircase from above could strike their opponents with weapons in their right-hands whereas the attackers climbing the staircase would have to use their left-hands to strike giving the defenders both a height and strength advantage.

1.2.2 Chiral Molecules

Molecules can be chiral if they possess a carbon atom that is bonded to four different groups/ligands. Figure 1.9 shows a simple example of a chiral molecule and its mirror image (enantiomer). It is impossible for either structure to be super-imposed upon the other and so, following Lord Kelvin's definition, the molecules are chiral.

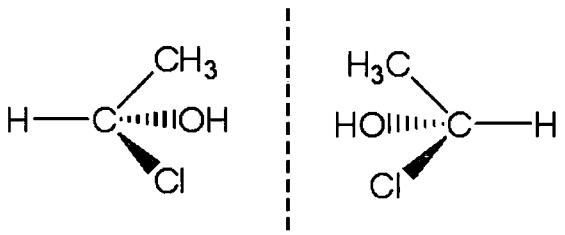

Figure 1.9: Diagram of a simple chiral molecule and its enantiomer.

Chiral molecules of this type can be characterised using the chirality rule of Cahn, Ingold and Prelog.[14] Using this rule the four groups bonded to the carbon atom are arranged in an order of priority, with higher priority given to groups with higher atomic numbers. For example Cl>OH>CH_3>H (or more generally A>B>D>E). Looking down the bond between the carbon and the atom of the lowest priority (E) and counting clockwise, if the groups appear in the order A, B, D then the molecule is labelled *R* for rectus (Latin for right), and if the order is A, D, B then the molecule is labelled *S* for sinister (Latin for left) (see figure 1.10). Optically, molecules are also labelled by the direction that they rotate plane polarized light.

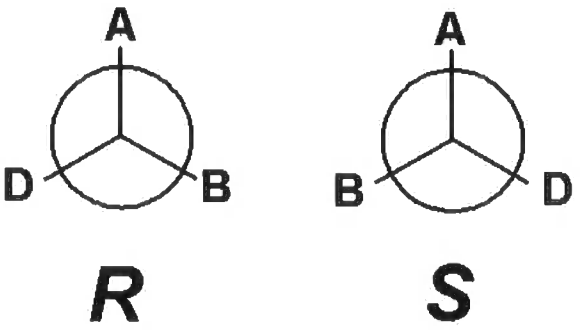

Figure 1.10: General definition of R (rectus, left) and S (sinister, right) enantiomers where the order of priority using the Cahn, Ingold and Prelog rule is A>B>D>E (diagram shown looking down the C-E bond).

If a molecule rotates it clockwise then it has positive optical activity (+), and if it rotates it anti-clockwise it has negative optical activity (-).

Molecules can be chiral even if they do not possess a chiral carbon atom. Other types include axially chiral molecules, and some examples are shown in figure 1.11.

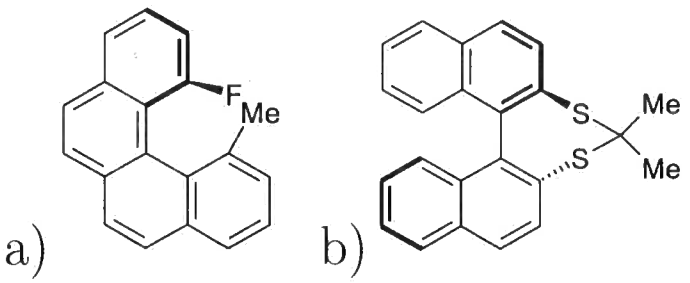

Figure 1.11: Examples of axially chiral molecules a) helicene derivative and b) bridged-biaryl derivative.

It should be noted that almost all achiral molecules can adopt chiral conformations. These molecules do not display any optical activity as the number of right-handed and left-handed conformations that are sampled are the same.

1.2.3 Chiral Mesophases

Chiral liquid crystalline phases are generally formed by chiral liquid crystalline molecules. The phases that can be formed include the chiral nematic phase (see section 1.1.2 and figure 1.3), the smectic-C* phase (see figure 1.12), blue phases[15] and twist grain boundary phases.[16,17]

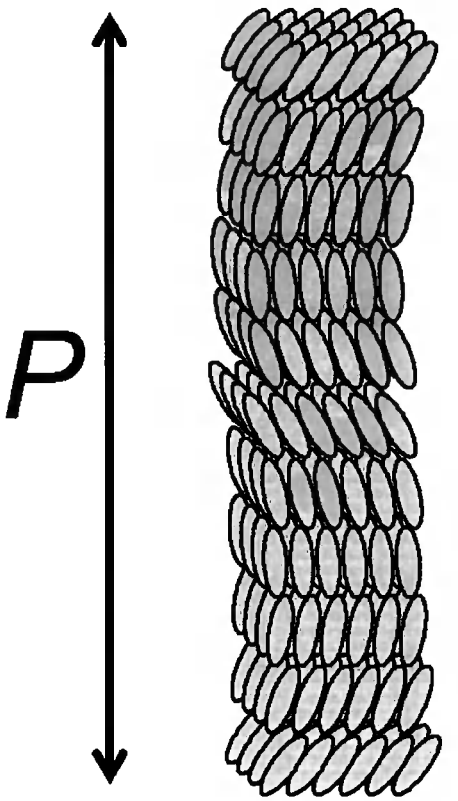

Figure 1.12: Schematic diagram of the chiral smectic-C* phase with a helical pitch of P (the pitch shown is considerably smaller than that of a real smectic-C*, where P is typically $>1\mu$m, and the helix is made up of thousands of molecular layers).

A pure compound cannot undergo a phase transition from a nematic to a chiral nematic phase. However, the two phases are completely miscible and the addition of chiral additives to a nematic can induce chirality in the phase to form a chiral nematic. A measure of the degree of chirality that a molecule can induce in the phase is known as the helical twisting power (see section 1.3). A material that forms a chiral nematic phase may also form a non-chiral smectic-A phase as well as a chiral smectic-C* phase. It is also possible for achiral molecules to form chiral phases. Bent-

core (banana-shaped) molecules have recently been found to form liquid crystalline supramolecular chiral structures (the so-called B phases).[18–21] Intriguingly, achiral banana-shaped molecules have been found to act as chiral dopants when added to cholesteric phases, increasing the twist of the system even when added in only small concentrations.[22] This process is not fully understood at the present time.

1.3 Helical Twisting Powers (HTPs)

When a nematic liquid crystal is doped with a low concentration of chiral solute molecules a chiral nematic (cholesteric) phase is induced in the system (as described in section 1.2.3). The helical twisting power (HTP) of a liquid crystal chiral dopant is a measure of the degree of twist the dopant can induce. The macroscopic HTP, β_M, is defined as

$$\beta_M = (Pc_w r)^{-1}, \tag{1.3}$$

where c_w is the weight concentration of the chiral dopant molecules and r is the enantiomeric purity of the chiral dopant. β_M is positive for induced right hand helical twists and negative for induced left hand helical twists. Enantiomers have HTPs of exactly the same magnitude but of an opposite sign.

There are important technological uses for chiral dopants materials. They are used in low concentrations in twisted nematic displays, and in chiral films for use with displays. They can also be used in polarization sensitive polymer films[23] and thermally addressed display materials.[24] In many applications however, limits on solubility of the dopant, or specific material requirements mean that only small concentrations of chiral dopants can be employed. Consequently, there has been considerable interest in the synthesis of materials with high β_M values. However, this can be an extremely difficult task to achieve. It is often difficult to predict how the molecular structure of a chiral dopant is related to the helical twisting power it induces. Small changes in structure can lead to large changes in β_M.[25,26] This means that expensive and time-consuming synthetic projects are undertaken with no guarantee of producing dopants with the required properties. Clearly a theoretical method that could predict helical twisting powers reliably would be extremely

valuable. It would improve the scientific understanding of why some molecules have large HTPs and some do not, and it could be used as a way of sifting through many trial molecular structures prior to attempting a difficult synthetic pathway. The prediction of key material properties based only on a prior knowledge of chemical structure and molecular interactions is also one of the key aims of theoretical chemistry.

1.3.1 Calculating the Helical Twisting Power

A number of workers have attempted to provide a theoretical framework for predicting HTPs. There are five main methods that have so far been proposed in the literature and they are summarised below.

Surface Chirality Model and the Chirality Order Parameter

Nordio, Ferrarini and co-workers have produced an interesting theoretical model for predicting HTPs based on a mean field description of the interactions between a chiral solute molecule and a liquid crystal solvent.[27–30] Their model has shown considerable success and has been applied to a number of different types of molecule.

Chemical Potential Difference between Enantiomers

Cook and Wilson[31] recently formulated a different technique for obtaining HTPs of chiral dopants based on some earlier work by Allen.[32] This method involves simulations of a chiral dopant molecule in a twisted nematic solvent using an efficient Monte Carlo (MC) simulation program. The MC simulations are used to compute the difference in chemical potential, $\Delta\mu$, between a chiral solute and its enantiomer immersed in the same *twisted nematic* solvent. $\Delta\mu$ is directly proportional to β_M, and, given a value for the twist elastic constant, K_2, an absolute value for β_M can be predicted.

Scaled Chiral Index

The scaled chiral index is based upon an intrinsic measure of molecular chirality proposed by Osipov and co-workers.[33] Neal *et al.*[34] extended the formulation to

a scaled chiral index. This index has been applied to a number of different chiral dopant molecules and has been found to show good agreement with experimental helical twisting powers.[35,36]

Mean Field Approximation Linking Helical Twisting Powers to Circular Dichroism Measurements

Osipov and Kuball[37] have derived explicit expressions for the helical twisting power of a chiral dopant in the nematic phase by using a mean field approximation that takes into account chiral dispersion intermolecular interactions. The theory has only been applied to one test molecule, an aminoanthraquinone, but has been successful in explaining correlations between the signs of helical twisting power and circular dichroism measurements.

Intermolecular Torques

Germano *et al.*[38] recently presented a method that provides a quantitative calculation of chiral strength by the measurement of intermolecular torques in a system. The method was applied to a system consisting of chiral mesogenic particles but it could be adapted to measure helical twisting powers for the addition of chiral molecules to a liquid crystalline phase.

1.4 Scope of thesis

The main aim of this thesis is to use computational and theoretical techniques to provide predictions of molecular chirality and helical twisting powers for liquid crystalline chiral dopant molecules and materials. The thesis is arranged as follows: in chapter 2 the computational techniques and methods employed in the work are presented. In chapter 3 computer simulations of soft repulsive spherocylinders with a total length to breadth ratio of 5:1 are carried out. These liquid crystalline molecules are used in chapter 4 in Monte Carlo free energy calculations that are used to calculate the helical twisting powers (HTPs) of liquid crystal chiral dopants. The work is based on an original computational technique proposed by Cook and Wilson,[31,39]

which involved simulating a chiral nematic phase using a Gay-Berne solvent in a simulation box subject to twisted periodic boundary conditions. A series of Monte Carlo simulations were used to grow an atomistic model of a chiral dopant into this solvent and statistical perturbation theory was used to measure the free energy change for this process. Comparison of the free energy difference obtained from this calculation for a particular enantiomer and its mirror image allows a calculation of the HTP of the chiral dopant to be made. This chapter includes work that has been conducted on improving the accuracy and efficiency of the free energy calculations used in the technique and details the results of the simulations using a SRS and Gay-Berne solvent.

In chapter 5, the chirality order parameter and the scaled chiral index are applied to a number of chiral dopant molecules and systems. These are single molecule techniques that, for a given molecular conformation, can provide a rapid calculation of chirality. These methods are of great interest due to their computational cheapness. In the future, it may be possible to use these methods to screen large numbers of chiral molecules for high HTP values prior to synthesis. The chirality order parameter and the scaled chiral index are also incorporated in Monte Carlo simulations to study flexible chiral molecules, liquid crystalline materials, and to investigate the temperature dependence of the HTP in chapter 6. In chapter 7, an approach is used that directly measures the impact of a chiral molecule on a liquid crystal solvent. Using statistical mechanics it is possible to relate the torque the chiral molecule induces in the solvent, as chirality is transferred to the system, to the helical twisting power. Finally in chapter 8, conclusions are drawn.

Chapter 2

Computer Simulations and Computational Techniques

2.1 Introduction to Computer Simulation

Computer simulations, or computational experiments, are now considered to be the main tool in testing scientific theory. For a given model system, a computer simulation can provide an exact result for a property of interest and allows for a direct comparison with experimental findings. Computer simulation is used in chemistry to study the microscopic properties of atoms, molecules and bulk systems. Either classical or quantum mechanical energy minimisation techniques can be used to calculate important properties for single molecules. These include preferred chemical conformations and dipole moments. In addition, computer simulation can be used for bulk systems to calculate key macroscopic properties of experimental interest, such as heat capacities, enthalpy changes and free energy differences. The two main simulation methods used to study bulk systems are molecular dynamics (MD) and Monte Carlo (MC).

2.1.1 Computer Simulation of Liquid Crystals

Liquid crystals continue to be of great interest to theoreticians as well as experimentalists due to their rich phase behaviour as well as their many applications and

potential uses. At present, computer simulation of a large number of liquid crystal molecules (>1000) is only realistically possible for simplified models of liquid crystals. There are many different potentials and models used to simulate the behaviour of liquid crystals. These include the Gaussian Overlap potential,[40] the Gay-Berne potential,[41–43] hard spherocylinders[44–47] and soft repulsive spherocylinders[48–51] (see chapter 3). Although these models are simplified they allow for the investigation of structure-property relationships in liquid crystalline molecules. However, with recent increases in computational power, fully atomistic studies of liquid crystalline systems are beginning to become more accessible.[52–55]

2.2 Model Potentials

In computer simulations, the interactions between particles are determined by the potentials used to model them. A potential can be used to represent individual atoms in a molecule, for example a Lennard-Jones type potential (see section 2.2.3) can be employed. Alternatively, a potential can be used to represent a part of or the whole of a molecule, for example the Gay-Berne potential (see section 2.2.4) or the soft-repulsive spherocylinder potential (see chapter 3) can be employed. Potentials used in computer simulations are generally pair potentials, although it is possible to include three-body terms at additional computational expense (this is rarely done due to sums over triplets of particles being computationally very time consuming). Some of the more well used and popular pair potentials are summarised below.

2.2.1 Hard Potentials

Hard potentials are very simple, idealised potentials. In hard potentials, particles are not allowed to overlap with each other. The simplest possible form is the hard sphere potential where the pair potential, $U(r)$, at an inter-particle distance of r is given by

$$U(r) = \begin{cases} \infty & (r < \sigma) \\ 0 & (r \geq \sigma) \end{cases}, \tag{2.1}$$

where σ is the diameter of the spheres (see figure 2.1). Hard sphere simulations have

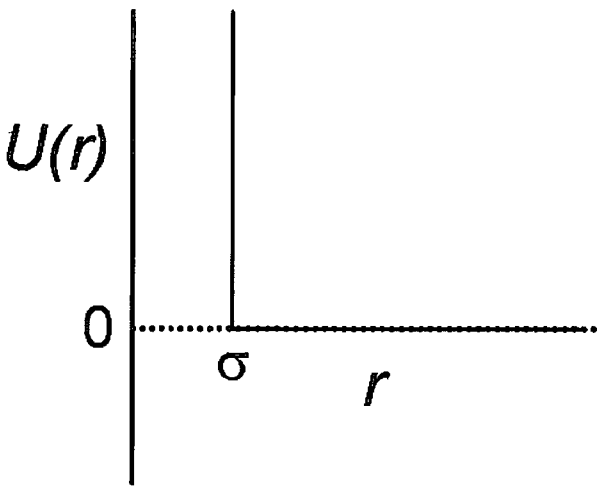

Figure 2.1: Hard sphere potential, $U(r)$, as a function of interatomic distance, r.

been used to provide quantitative comparison with liquid-state theory.[56] Physically, the potential corresponds to the highly repulsive short-range interactions between particles due to the overlap of electron clouds. As a result, the physics of hard particle systems depends purely on the shape of the particles and the density of the system, and not on factors such as the temperature.

Hard models of liquid crystalline molecules are also of interest. Onsager theory predicts liquid crystalline ordering for rod-shaped hard bodies.[57] Subsequent simulations of hard spherocylinder molecules found isotropic, nematic, smectic-A and solid ordering in the phase diagrams of these molecules.[44–47] In this theory, the isotropic to nematic liquid crystalline phase transition is driven by the competition between orientational entropy and the contribution to entropy from the excluded volume of the molecular cores. When the particles are aligned, the entropic contribution from the latter is maximised.

2.2.2 Soft Potentials

In real molecules short-range repulsive and longer-range attractive forces contribute to the interactions between particles. A large number of soft pair potentials have

been suggested in the theoretical and computational community, varying from simple soft-sphere potentials to more complicated Lennard-Jones and anisotropic potentials such as the Gay-Berne.

2.2.3 Lennard-Jones Potential

The Lennard-Jones (LJ) potential is a continuous, isotropic potential that can be used to model spherical atoms. The potential has been applied extensively in liquid state theory.[56] The pair potential takes the following form:

$$U_{ij}(r) = 4\varepsilon\left[\left(\frac{\sigma}{r_{ij}}\right)^{12} - \left(\frac{\sigma}{r_{ij}}\right)^{6}\right], \tag{2.2}$$

where r_{ij} is the separation between the centre of masses of the two particles, ε is the well depth of the potential and σ is the separation at which $U_{ij}(r) = 0$. Figure 2.2 shows a typical LJ potential along with each of the parameters defined above. In the potential the r_{ij}^{-12} term models the short-range repulsive force due to the overlap of electron clouds and the r_{ij}^{-6} term models long-range attractive forces between atoms.

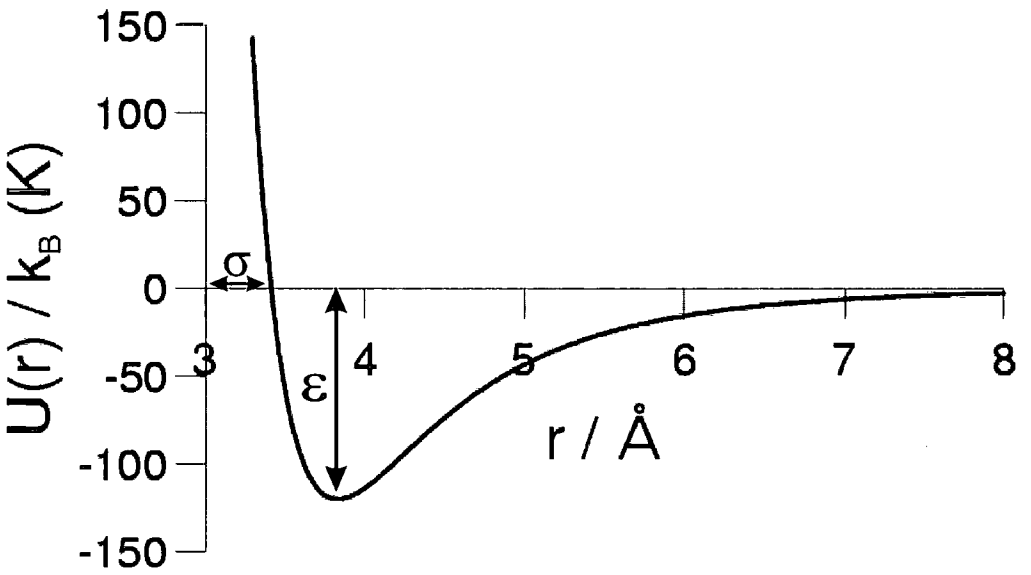

Figure 2.2: Lennard-Jones pair potential for Ar.

The LJ potential is frequently used in atomistic simulations of molecules where appropriate values of ϵ and σ are assigned to each atom in the molecules studied. It should be noted that these are effective pair potentials that have been adjusted to give, for example, correct experimental densities for these atoms. Therefore the potential takes into account three body forces, but in an averaged way. Values of ε and σ for interactions between pairs of identical atoms in different molecules, found from simulation studies, are given in table 2.1.

Atom	ε/k_B	σ/Å
H	8.6	2.81
He	10.2	2.28
C	51.2	3.35
N	37.3	3.31
O	61.6	2.95
S	183.0	3.52
F	52.8	2.83
Cl	173.5	3.35
Ne	47.0	2.72
Ar	119.8	3.41
Kr	164.0	3.83

Table 2.1: Atom-atom interaction parameters for the Lennard-Jones potential, taken from reference.[58]

2.2.4 Gay-Berne Potential

The Gay-Berne potential[41] is based on the Lennard-Jones potential and is frequently used for the simulation of liquid crystalline systems. Each Gay-Berne particle represents a mesogenic molecule (or a rigid mesogenic part of a molecule in more sophisticated studies). The main feature of the pair potential is that it is anisotropic and depends not only on the intermolecular separation, $\mathbf{r}_{ij}$, but also on the relative orientations of the two Gay-Berne particles, $\mathbf{u}_i$ and $\mathbf{u}_j$ (see figure 2.3). Gay-Berne particles are ellipsoidal, and their exact shape is defined by the shape anisotropy parameter χ:

$$\chi = \frac{\kappa^2 - 1}{\kappa^2 + 1}, \tag{2.3}$$

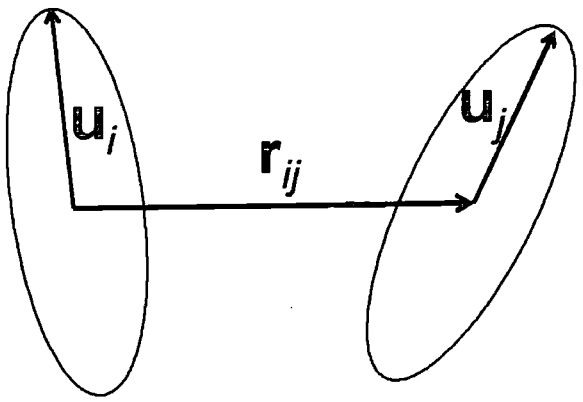

Figure 2.3: Intermolecular separation, $\mathbf{r}_{ij}$, between two Gay-Berne particles with orientations $\mathbf{u}_i$ and $\mathbf{u}_j$.

where $\kappa = \sigma_{ee}/\sigma_{ss}$, σ_{ee} is the end to end contact distance and σ_{ss} is the side to side contact distance. For the limiting cases, a sphere corresponds to $\chi = 0$, an infinitely long rod to $\chi = 1$, and an infinitely thin disc to $\chi = -1$.

The intermolecular potential takes the form:

$$\begin{aligned} U_{ij}^{GB} &= 4\epsilon^{GB}(\mathbf{r}_{ij}, \mathbf{u}_i, \mathbf{u}_j) \\ &\times \left[\left(\frac{\sigma_0^{GB}}{r_{ij} - \sigma(\mathbf{r}_{ij}, \mathbf{u}_i, \mathbf{u}_j) + \sigma_0^{GB}} \right)^{12} - \left(\frac{\sigma_0^{GB}}{r_{ij} - \sigma(\mathbf{r}_{ij}, \mathbf{u}_i, \mathbf{u}_j) + \sigma_0^{GB}} \right)^{6} \right] \end{aligned}$$

where the orientationally dependent well depth is given by

$$\epsilon^{GB}(\mathbf{r}_{ij}, \mathbf{u}_i, \mathbf{u}_j) = \epsilon_0^{GB} \left[\epsilon^{GB}(\mathbf{u}_i.\mathbf{u}_j) \right]^{\nu} \left[\epsilon'^{GB}(\mathbf{u}_i, \mathbf{u}_j, \mathbf{r}_{ij}) \right]^{\mu},$$

and

$$\epsilon^{GB}(\mathbf{u}_i.\mathbf{u}_j) = \left[1 - \chi^2 (\mathbf{u}_i.\mathbf{u}_j)^2 \right]^{\frac{1}{2}},$$

and

$$\epsilon'^{GB}(\mathbf{u}_i, \mathbf{u}_j, \mathbf{r}_{ij}) = \left[1 - \frac{\chi'}{2} \left(\frac{(\mathbf{r}_{ij}.\mathbf{u}_i)^2 + (\mathbf{r}_{ij}.\mathbf{u}_j)^2 - 2\chi'(\mathbf{r}_{ij}.\mathbf{u}_i)(\mathbf{r}_{ij}.\mathbf{u}_j)(\mathbf{u}_i.\mathbf{u}_j)}{1 - \chi^2(\mathbf{u}_i.\mathbf{u}_j)^2} \right) \right].$$

χ' is the well depth anisotropy parameter given by

$$\chi' = \frac{\kappa'^{\frac{1}{\mu}} - 1}{\kappa'^{\frac{1}{\mu}} + 1},$$

where $\kappa' = \epsilon_{ss}/\epsilon_{ee}$ and ϵ_{ss} and ϵ_{ee} are the well depths when the molecules are respectively side to side and end to end. $\sigma(\mathbf{r}_{ij}, \mathbf{u}_i, \mathbf{u}_j)$ is the anisotropic contact distance:

$$\sigma(\mathbf{r}_{ij}, \mathbf{u}_i, \mathbf{u}_j) = \sigma_0^{GB}\left[1 - \chi\left(\frac{(\mathbf{r}_{ij}.\mathbf{u}_i)^2 + (\mathbf{r}_{ij}.\mathbf{u}_j)^2 - 2\chi(\mathbf{r}_{ij}.\mathbf{u}_i)(\mathbf{r}_{ij}.\mathbf{u}_j)(\mathbf{u}_i.\mathbf{u}_j)}{1 - \chi^2(\mathbf{u}_i.\mathbf{u}_j)^2}\right)\right],$$

and σ_0^{GB} and ϵ_0^{GB} are constants. The exact form of the Gay-Berne potential is determined by the four parameters κ, κ', μ and ν. Various forms of the potential have been studied. These include the Gay-Berne particles of de Miguel *et al.*[59] with $\kappa = 3$, $\kappa' = 5$, $\mu = 2$ and $\nu = 1$, which form stable nematic and smectic-B phases, of Luckhurst *et al.*[43] with $\kappa = 3$, $\kappa' = 5$, $\mu = 1$ and $\nu = 2$, which form stable nematic, smectic-A and smectic-B phases, and of Berardi *et al.*[60] with $\kappa = 3$, $\kappa' = 5$, $\mu = 1$ and $\nu = 3$, that form stable nematic and smectic-B phases. The simulation work conducted in chapters 4 and 7 of this thesis use the parameters $\kappa = 3$, $\kappa' = 5$, $\mu = 2$ and $\nu = 1$ and the exact form of this potential (along with two other potentials with different values of κ and κ') can be seen in figure 2.4.

A large body of work has been conducted with the Gay-Berne potential and several interesting extensions to the model have been studied such as Gay-Berne particles with dipoles[62–64] and quadrupoles,[65,66] discotic GBs,[67] biaxial GBs,[68] and chiral GBs.[69] For an excellent review see references.[70,71]

2.3 Molecular Mechanics

The molecular mechanics technique[72,73] uses a classical force-field to calculate the energy of a particular conformation of a molecule. Force-fields represent a molecule as a collection of atoms which are coupled to each other by elastic restoring forces.

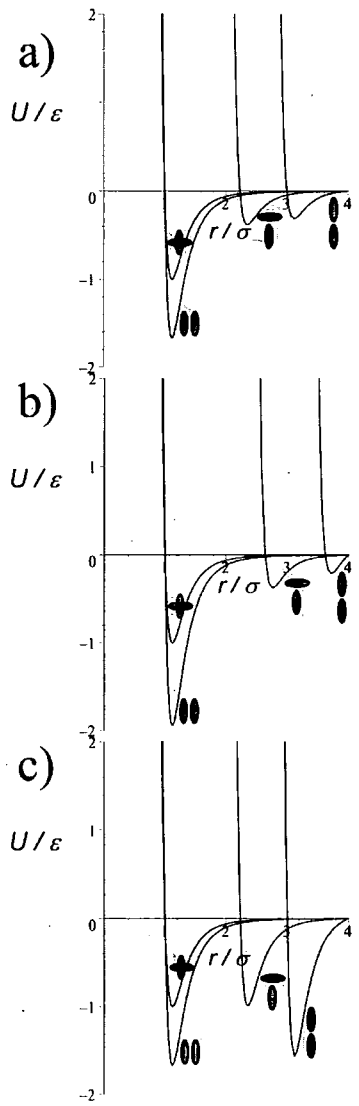

Figure 2.4: Gay-Berne potential for particles in crossed, side-by-side, end-to-side and end-to-end configurations for the parameters $\mu = 2$, $\nu = 1$ and a) $\kappa = 3$, $\kappa' = 5$, b) $\kappa = 3.6$, $\kappa' = 5$ and c) $\kappa = 3$, $\kappa' = 1$ (reproduced from reference[61]).

They typically take the form

$$E = \sum_{bond} E_{bond} + \sum_{angle} E_{angle} + \sum_{dihedral} E_{dihedral} + \sum_{non-bonded} E_{non-bonded} + \ldots, \quad (2.4)$$

where E is the total configurational energy of a particular conformation. By minimising the energy of the molecule in the force-field the lowest energy conformation can be found. For large molecules this minimisation process can be difficult on account of the complex form of the potential energy surface produced by the force-field used and the number of different variables involved. There will often be a large number of local minima on the potential surface with energies close to the overall 'global' energy minimum making it difficult to find.

A number of different force-fields and minimisation techniques have been developed. Among the best and most frequently used classical force-fields are the MM1-4 series,[74–78] AMBER,[79] CHARMM[80,81] and OPLS.[82,83] The choice of the force-field used depends on factors such as the system being studied, the accuracy, and the computational efficiency of the methods. Molecular mechanics techniques are most frequently used to calculate optimised geometries of molecules and torsional barriers for rotations around particular dihedral angles.[74–77,79,80,82–85] They can also be used to predict vibrational frequencies,[76,77] heats of formation,[74–76,86,87] heats of vaporization,[82,83,85] and reaction rates[88] (for a review see reference[73]). One of the main advantages of molecular mechanics techniques is their computational speed. For more detailed studies, quantum mechanical *ab initio*/density functional theory calculations are more appropriate. Calculations of this type are used and described in chapter 6 to calculate the energy of rotation about a bond that the MM2 force-field does not model correctly.

2.3.1 MM2 and MM3 Force-Fields

The MM2 force-field of Allinger[75] is a good example of a molecular mechanics force-field. It is used in chapters 4 and 7 of this thesis to determine energy minimised structures of molecules and in chapter 6 to calculate conformational energies of molecules in flexible molecular Monte Carlo simulations.

The energy of a molecule within the MM2 force-field is given by:

$$
\begin{aligned}
U_{MM2} &= \sum_{bond}^{stretching} k_b^s (l - l_0)_{ij}^2 (1 - 2(l - l_0)_{ij}) \\
&+ \sum_{angle}^{bending} k_\theta^b (\theta - \theta_0)_{ijk}^2 (1 + SF.(\theta - \theta_0)_{ijk}^4) \\
&+ \sum_{angle}^{stretch-bend} k_\theta^{s-b} (\theta - \theta_0)_{ijk} ((l - l_0)_{ij} + (l - l_0)_{jk}) \\
&+ \sum_{torsions} \frac{V_1}{2}(1 + \cos\omega) + \frac{V_2}{2}(1 - \cos 2\omega) + \frac{V_3}{2}(1 + \cos 3\omega) \\
&+ \sum_{non-bonded}^{vdW} \epsilon(2.90 \times 10^5 \exp(-12.50/P) - 2.25P^6) \\
&+ \sum_{non-bonded}^{electrostatic} \frac{3\mu_i\mu_j(\cos X_{ij} - 3\cos a_i \cos a_j)}{2r^3}.
\end{aligned}
\tag{2.5}
$$

In the bond stretching term, k_b^s is the bond stretching constant and l and l_0 are the actual and natural bond lengths of the bond between atoms i and j in the molecule. In the angle bending term, k_θ^b is the angle bending constant, θ and θ_0 are the actual and natural bond angles of the bond angle between atoms i, j and k in the molecule, and SF is the quartic bending term. k_θ^{s-b} is the angle stretch-bend constant and the energy of a torsional angle ω is defined in terms the V_1, V_2 and V_3 torsional constants in the Fourier expansion. In the non-bonded van der Waals term, $\epsilon = (\epsilon_i \epsilon_j)^{\frac{1}{2}}$ where ϵ_i and ϵ_j are the van der Waals well depths of atoms i and j respectively, and P is the sum of van der Waals radii of i and j, divided by the distance between interacting atom centers, r. For the electrostatic term, μ_i and μ_j are bond dipoles, X is the angle between the dipoles, r is the distance between the mid-point of the bonds, and a_i and a_j are the angles between the dipole axes and the line along which r is measured.

The MM2 force-field is a good, computationally cheap force-field for calculating energy minimised structures of molecules. However, there are certain deficiencies in MM2 which led to the development of more sophisticated molecular mechanics force-fields, such as MM3[76] and MM4,[77,78,89–91] to deal more effectively with ring structures, hydrogen-hydrogen nonbonded repulsions, and bond lengths of eclipsed

bonds to name just a few. The MM3 force-field is used in chapter 5 of this thesis to calculate energy minimised structures of a number of relatively rigid chiral molecules.

2.3.2 Energy Minimisation

The computational determination of an equilibrium minimum energy geometry for a molecule is an iterative process. In simple search techniques, such as the *steepest descent* method,[92] the slope of the potential energy surface (first derivative) is used to calculate potential minima. In more complex methods, such as the *Newton-Raphson* approach,[93,94] both the slope and the curvature of the potential surface (second derivative) are used. In large molecules, the search procedure can become very complex due to the large number of local minima with energies close to the overall global minimum.

2.4 Simulation Methods

In order to calculate useful properties of a given system, computer simulations must sample all of phase space. By generating many different configurations, Γ, of a given system in terms of the spatial positions and orientations of the constituent particles in the system, averages may be calculated. These averages can be computed by time averaging (the molecular dynamics approach) or by ensemble averaging (the Monte Carlo approach).

2.4.1 Monte Carlo

The Monte Carlo simulation method was formulated by Metropolis.[95] The aim of the simulation is to calculate an ensemble average of a property, A, by properly exploring phase space and evaluating the expression

$$< A >= \frac{\int A(\Gamma) \exp\left[\frac{-E(\Gamma)}{k_B T}\right] d(\Gamma)}{\int \exp\left[\frac{-E(\Gamma)}{k_B T}\right] d(\Gamma)}, \tag{2.6}$$

where the denominator term is the configurational integral, $E(\Gamma)$ is the internal energy and $A(\Gamma)$ is the value of the property in question in the configuration Γ. These integrals in equation 2.6 cannot be evaluated analytically and so a statistical approach must be used. The main difficulty with Monte Carlo simulations is the proper sampling of phase space. In a simple minded approach one could make random changes to the positions and orientations of particles in the system and calculate $E(\Gamma)$ and $A(\Gamma)$ in each configuration. However, the problem with this approach is that only a very small number of the configurations that we would sample would have meaningful physical significance (the Boltzmann factor $\exp\left(\frac{-E(\Gamma)}{k_B T}\right)$ will be zero for almost all of the configurations), especially in the simulation of condensed matter phases. Therefore, not only would this approach be time consuming, it would also be subject to large statistical errors. In order to properly sample phase space we must use importance sampling, by implementing the Metropolis Monte Carlo method.

Metropolis Monte Carlo

In Metropolis Monte Carlo, physically realistic low energy configurations are more frequently sampled due to the introduction of biasing. In this approach, configurations are sampled from a Boltzmann distribution and the simulation proceeds along an iterative path in the following way:

i) From an initial configuration with a configurational energy of E_{old} an atom/particle is randomly moved by a displacent δr and rotated by an angle $\delta\phi$. For non-rigid particles a change in conformation is also performed.

ii) The energy of this new configuration is calculated as E_{new}.

iii) If $E_{new} < E_{old}$ then this new configuration is accepted and becomes the starting point for the next Monte Carlo sweep.

iv) If $E_{new} > E_{old}$ then a random number is generated with a value between 0 and 1.

v) If $\exp\left[\frac{-(E_{new}-E_{old})}{k_B T}\right]$ is greater than the random number then the new configuration is accepted and becomes the starting point for the next Monte Carlo sweep.

vi) If $\exp\left[\frac{-(E_{new}-E_{old})}{k_BT}\right]$ is less than the random number then the new configuration is rejected and the old configuration is used as the starting point for the next Monte Carlo sweep.

In this way, configurations are randomly generated with the probability density:

$$N(\Gamma) = \frac{\exp\left[\frac{-E(\Gamma)}{k_BT}\right]}{\int \exp\left[\frac{-E(\Gamma)}{k_BT}\right] d(\Gamma)}.$$

In the equilibration stage of a simulation, the maximum displacement, δr_{max}, and maximum rotation, $\delta\phi_{max}$, can be adjusted so that between 35 and 55% of the trial moves are accepted. This is necessary because, if δr_{max} and $\delta\phi_{max}$ are chosen to be too small then almost all of the trial moves are accepted but phase space is explored very slowly and, if δr_{max} and $\delta\phi_{max}$ are chosen to be too large then hardly any moves will be accepted and once again phase space will not be explored correctly.

When handling a flexible molecule it is useful to work in the internal co-ordinate system of the molecule. In every Monte Carlo cycle, changes can be made to bond lengths, bond angles and torsional angles, and moves are accepted with the correct Boltzmann probability using the method described above. However, ring systems cannot be dealt with in this manner as one change in a bond length, angle or torsional angle causes large changes in other bond lengths, angles and torsional angles within the ring. For this reason, ring systems generally remain rigid in flexible simulations.

In this thesis, Monte Carlo simulations are performed in chapters 4 and 7 on systems of rigid particles, and in chapter 6 on flexible molecules in the gas phase.

2.4.2 Molecular Dynamics

In the molecular dynamics (MD) approach to computer simulation all atoms/particles are subject to the laws of Newtonian mechanics. For a system of N atoms/particles with Cartesian coordinates, $\mathbf{r}_i$, Newton's second law is given by:

$$m_i \frac{d^2\mathbf{r}_i}{dt^2} = \mathbf{F}_i, \tag{2.7}$$

where m_i is the mass of atom/particle i and $\mathbf{F}_i$ is the force on atom/particle i. The usual method of solving these coupled second order differential equations for each atom/particle in the system is to use a finite difference method (integration algorithm). In this approach a discrete timestep, δt, is used to advance the simulation. The basic idea behind the finite difference technique is that, given the positions, velocities, accelerations and other dynamical information about the atoms/particles in a system at a time, t, we are able to predict the new positions, velocities, accelerations etc. at a time $t + \delta t$. From these new positions one can then calculate the new force on each atom/particle. Using these new forces one can then repeat the process of calculating the new positions, velocities, accelerations etc. at time $t + 2\delta t$. The timestep that is used must be small enough to allow for acceptable solutions of the equations of motion and ensure that energy is conserved in the simulation. However, the simulation will proceed at a faster rate if a longer timestep is used so it is essential to use a 'good' algorithm that incorporates reasonable energy conservation with a fairly long timestep.

Force Calculation

The calculation of the forces acting on each particle in a system is the most computationally expensive part of a MD simulation (between 80-95% of the simulation time). The force acting on particle i is determined as:

$$\mathbf{F}_i(t) = - \bigtriangledown_{\mathbf{r}_i} V(\mathbf{r}_i(t)), \tag{2.8}$$

where $V(\mathbf{r}_i(t))$ is the potential energy calculated from the co-ordinates at time, t. The total force on each particle, F_i, will be composed of a sum of the contributions to the force on particle i from each of its neighbours. For a system of N particles this calculation scales as N^2, but with the use of a cut-off length and efficient computational techniques, such as the use of a Verlet neighbour list (see reference[96] for a review), the calculation can scale as N. Once the force on each particle at time t and position $\mathbf{r}(t)$ is calculated, the finite difference integration algorithm is used to progress the simulation to time $t + \delta t$ and positions $\mathbf{r}(t + \delta t)$. The new forces are

then recalculated from the new positions and the process repeats itself.

Integration algorithms

There are numerous integration algorithms that can be used in MD work. A short review of some of the more popular finite difference integration algorithms now follows.

Verlet algorithm

One of the original and simplest integration algorithms is the *Verlet* algorithm[97] which advances the positions of the atoms/particles using

$$\mathbf{r}(t+\delta t) = 2\mathbf{r}(t) - \mathbf{r}(t-\delta t) + \mathbf{a}(t)\delta t^2 + ... \tag{2.9}$$

$\mathbf{a}(t)$ is the acceleration at time t and there is an error of δt^4 in the calculation of the new positions if we truncate the expansion at the δt^2 term (this is called the *Euler* algorithm). Although the velocitites are not required to calculate the trajectories they can be found from

$$\mathbf{v}(t) = \frac{\mathbf{r}(t+\delta t) - \mathbf{r}(t-\delta t)}{2\delta t}, \tag{2.10}$$

and are subject to errors of order δt^2. Due to the truncation of equation 2.9 the *Euler* algorithm is non-reversible and large energy drifts result from long simulations making it an undesirable algorithm to use. However, there are several useful algorithms based on the *Verlet* scheme, the most popular of which are detailed below.

Velocity Verlet algorithm

A version of the *Verlet* algorithm which stores the positions, velocities and accelerations of particles at the same time is the *velocity Verlet* algorithm,[98] which is of the form:

$$\mathbf{r}(t+\delta t) = \mathbf{r}(t) + \mathbf{v}(t)\delta t + \frac{1}{2}\mathbf{a}(t)\delta t^2, \tag{2.11}$$

$$\mathbf{v}(t+\delta t) = \mathbf{v}(t) + \frac{1}{2}\left[\mathbf{a}(t) + \mathbf{a}(t+\delta t)\right]\delta t. \tag{2.12}$$

Thus, the new velocities are calculated after the new positions and the new forces (and therefore accelerations) have been found. In chapter 3 the *velocity Verlet* algorithm is used in MD simulations of soft repulsive spherocylinder molecules.

Leap-frog algorithm

The *leap-frog* algorithm[99] is another prominent algorithm which is commonly used in MD simulations. The *leap-frog* method uses the mid-step velocities in order to calculate the positions at time $t + \delta t$. The mid-step velocities are defined as:

$$\mathbf{v}(t - \delta t/2) = \frac{\mathbf{r}(t) - \mathbf{r}(t - \delta t)}{\delta t}, \tag{2.13}$$

$$\mathbf{v}(t + \delta t/2) = \frac{\mathbf{r}(t + \delta t) - \mathbf{r}(t)}{\delta t}. \tag{2.14}$$

Rearranging equation 2.14 gives the expression for the new positions:

$$\mathbf{r}(t + \delta t) = \mathbf{r}(t) + \mathbf{v}(t + \delta t/2)\delta t, \tag{2.15}$$

and the updated velocities are found from

$$\mathbf{v}(t + \delta t/2) = \mathbf{v}(t - \delta t/2) + \mathbf{a}(t)\delta t. \tag{2.16}$$

To allow for the simultaneous calculation of the kinetic and potential energies of the system in question, the velocities at each step can be found from:

$$\mathbf{v}(t) = \frac{\mathbf{v}(t + \frac{1}{2}\delta t) - \mathbf{v}(t - \frac{1}{2}\delta t)}{2}. \tag{2.17}$$

Other notable integration algorithms include predictor-corrector algorithms[100] and Beeman's algorithm.[101]

2.4.3 Ensembles

A variety of different ensembles are used in computer simulation work, including the canonical (constant number of particles, N, volume, V and temperature, T), micro-

canonical (constant N, V and total energy, E), isothermal-isobaric (constant N, pressure, p and T) and grand-canonical (constant chemical potential, μ, V and T). All of the Monte Carlo simulations in this thesis (chapters 4, 6 and 7) are conducted in the NVT ensemble whilst the molecular dynamics simulations in chapter 3 are conducted in the NVT, NVE and NpT ensembles.

MD as described in section 2.4.2 corresponds to the NVE ensemble as new trajectories are generated with the same constant energy. However, it is often more convenient or desirable to conduct simulations in other ensembles in order to study different effects and to expand the applicability of simulations. A short overview of the techniques used to conduct MD simulations at constant temperature and pressure follows.

Constant Temperature

As temperature is directly related to the average kinetic energies of all the particles in the system, and hence the velocities, constant temperature simulations can be carried out by scaling the velocities of the particles. There are a number of different thermostats that can be used to do this.

Using the Andersen thermostat,[102] the simulation system is coupled to a heat bath (reservoir) that is at the desired temperature for the simulation. The strength of the coupling between the heat bath and the simulation can be determined by the frequency of stochastic collisions, ω (which can be selected by the simulator). During the simulation, particles are randomly selected (with a probability in a timestep of length δt of $\omega\delta t$) and their velocities are set at a value that is drawn from the Maxwell-Boltzmann distribution corresponding to the temperature of the heat bath.

In the approach proposed by Nosé,[103] the reservoir is represented by including an extra degree of freedom in the simulation. Energy can dynamically flow between the reservoir and the simulation system with a thermal inertia of Q (Q controls the thermal fluctuations in the system). Hoover simplified the approach by introducing a thermodynamic friction coefficient ξ. The resulting Nosé-Hoover thermostat[104] equations of motion are:

$$\dot{\mathbf{r}}_i = \mathbf{p}_i/\mathrm{m}_i, \tag{2.18}$$

$$\dot{\mathbf{p}}_i = \mathbf{f}_i - \xi \mathbf{p}_i, \tag{2.19}$$

$$\dot{\xi} = \frac{(\sum_i \mathrm{p}_i^2/\mathrm{m}_i - g k_B T)}{Q}, \tag{2.20}$$

where g is the number of degrees of freedom.

An alternative method for rescaling the velocities is the approach proposed by Berendsen.[105] At every time-step the old velocities $\mathbf{v}$ are rescaled to new velocities, $\mathbf{v}'$, by $\mathbf{v}' = \chi\mathbf{v}$ where

$$\chi = \left(1 + \frac{\delta t}{t_T}\left(\frac{T}{T_0} - 1\right)\right)^{\frac{1}{2}}, \tag{2.21}$$

and t_T is a time constant, T is the current temperature of the system and T_0 is the desired temperature of the system. The Berendsen method is very robust and can be used to steer the temperature to the desired value during the initial starting phase of a MD simulation, when energy can be poorly distributed between different degrees of freedom. However, it does not correctly sample the canonical ensemble.

In the MD simulations conducted in the NVT ensemble in chapter 3, the Nosé-Hoover thermostat is used.

Constant Pressure

Ensembles that work in the constant pressure regime all allow the size of the simulation box to change during the course of the simulation. The box may be allowed to change shape isotropically or anisotropically depending on the method used and the system that is being studied.

In the Berendsen approach,[105] the system is coupled to a pressure bath and obeys the equation:

$$\dot{P} = \frac{P_0 - P}{t_P}, \tag{2.22}$$

where P is the pressure of the system, P_0 is the desired pressure, and t_P is a time constant. At each time step the volume of the box is scaled by a factor of ξ and so the co-ordinates are scaled by a factor of $\xi^{\frac{1}{3}}$ where

$$\xi = 1 - \lambda_T \frac{\delta t}{t_P}(P_0 - P), \tag{2.23}$$

and λ_T is a compressibility factor.

Nosé-Hoover barostats can also be used. In the form proposed by Toxvaerd[106] the co-ordinates $\mathbf{q}^N$ are scaled to $\mathbf{r}^N = \mathbf{q}^N V^{-\frac{1}{3}}$. Introducing a friction ζ the equations of motion become:

$$\dot{\mathbf{r}}_i = \mathbf{p}_i/(\mathrm{m}_i V^{\frac{1}{3}}), \tag{2.24}$$

$$\dot{\mathbf{p}}_i = \mathbf{f}_i - (\dot{\zeta} + \xi)\mathbf{p}_i, \tag{2.25}$$

$$\dot{\zeta} = \dot{V}/(3V), \tag{2.26}$$

$$\ddot{\zeta} = \frac{(P - P_0)V}{Nk_BTt_P^2}, \tag{2.27}$$

where ξ is given by equation 2.20.

In the *NPT* ensemble MD simulations in chapter 3, the Hoover barostat in the Toxvaerd form (shown above) is utilised.

2.4.4 Parallel Molecular Dynamics

Molecular dynamics simulations can easily be parallelised so that the computational work-load is shared between a number of processors. By using efficient parallelisation techniques simulation times can be reduced by almost a factor of N_p, where N_p is the number of processors used. Parallelisation is useful due to the speed-ups in simulation time allowing longer runs and because it makes feasible the study of very large systems. The two techniques that are most frequently used to parallelise computer simulation codes are the replicated data (RD) method and the domain decomposition (DD) method (for reviews see references[107,108]).

In the RD method, each processor stores the positions of all the molecules/sites in the system, and at certain points in the simulation (such as a force calculation) performs its own portion of the overall calculation. When each processor needs to know the value of a quantity, whose calculation has been split over a number of different processors, a global sum operation must be performed. In the master/slave approach to a global sum, each processor communicates to a master computer that combines the information from each of the nodes (slaves). The master then recommunicates the combined information back to the slaves and the simulation can continue. A

more efficient way of carrying out a global sum uses the hypercube approach.[107] This type of parallelisation is very easy to implement but it does have certain drawbacks. As the number of processors used increases the communication time increases. For a large enough number of processors the simulation will become communications bound and the simulation will slow-down as more processors are added.

For the DD method the simulation time scales much more efficiently with the number of processors used but the implementation of the method is more complex. The DD algorithm splits the simulation box into equal sizes and assigns each sub-domain to an individual processor. The sub-domains must communicate with adjacent boxes in order to exchange information about particles on the edges of the sub-domains, but otherwise each sub-domain is free to compute the forces/potentials completely in parallel with the other processors. The DD method is especially efficient for short-range interactions where the range of the interaction is smaller than the size of the sub-domains. In chapter 3 the simulation code GBMOLDD,[109,110] which uses the domain decomposition algorithm, is used to simulate spherocylinders that have a short range, repulsive potential. Figure 2.5 shows a graph comparing the performance of the GBMOLDD simulation code with a RD code for simulations of a system made up of Gay-Berne/Lennard-Jones dimers for different numbers of processors. For these systems the DD algorithm scales much more efficiently with N_p than the RD algorithm.

2.5 Practicalities and Analysis

2.5.1 Periodic Boundary Conditions

One problem that must be overcome in computer simulations of bulk phases is how to deal with particles at the surface/boundary of a simulation box. If the simulation box was just an isolated system then particles at the edges of the box would experience a completely different environment to particles at the centre of the simulation. For small system sizes (simulations are often limited in size due to computational cost), these effects would have a very large effect on the properties of the system. For example, in a cubic crystal of 1000 atoms, approximately 49% of the atoms are at the

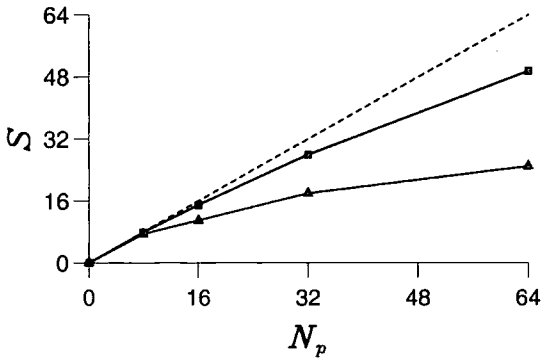

Figure 2.5: The speed up in terms of simulation time, S, for increasing number of processors, N_p, used to simulate a system of Gay-Berne/Lennard-Jones dimer molecules using GBMOLDD (squares) and a replicated data based simulation code[111] (triangles) on 8, 16, 32 and 64 nodes of a Cray T3E. The dashed line is the ideal, linear speed-up.

surface. In order to solve this problem, periodic boundary conditions are used, where the simulation box is repeated throughout space to effectively form an infinite bulk surrounding the original simulation box. When a molecule moves out of the original simulation box, so do the corresponding molecules in the neighbouring simulation boxes, and the identical image of the molecule re-appears at the opposite face of the simulation box. Thus, the number of particles in the simulation box always remains constant. This process is demonstrated in figure 2.6. The co-ordinates of the particles are only needed to be stored for the particles in the simulation box, and not for all of the images, due to the wrap-around nature of the system. Periodic boundary conditions have been found to be an extremely effective simulation tool, although there are certain side-effects of using them. For example, periodic boundary conditions cannot contain wavelength fluctuations that are longer than the length of the periodic box. This can be particularly trouble-some close to continuous phase transitions such as near to the gas-liquid critical point.

Three-dimensional periodic boxes are usually cubic or cuboidal in shape. However, a variety of other space-filling shapes, including truncated octahedrons and rhombic dodecahedrons, can also be employed. The simulations conducted in this

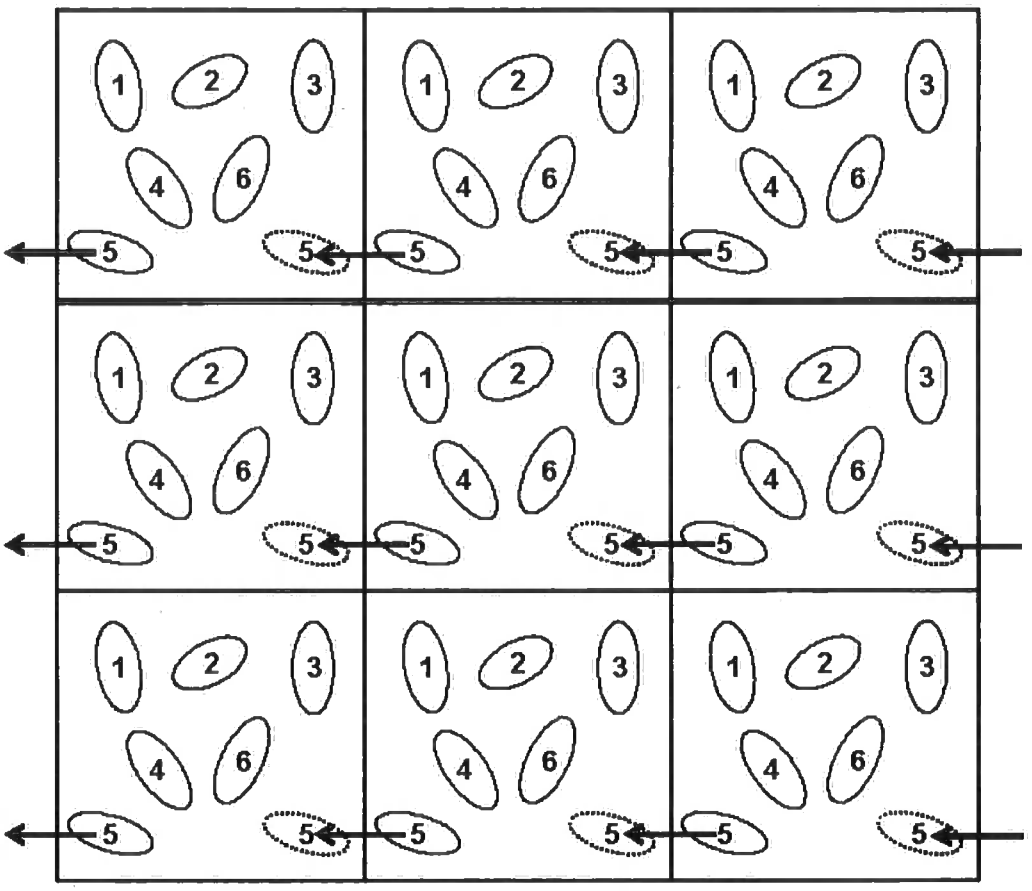

Figure 2.6: Schematic diagram showing periodic boundary conditions for a two-dimensional system. Particle 5 moves out of the simulation box to the left and reappears on the right of the box.

thesis in chapters 3 and 7 use periodic boundary conditions. In chapter 4, a special form of twisted periodic boundary conditions are required and are described in section 4.2.2.

2.5.2 Truncation of Intermolecular Interactions

In systems where short-range interactions constitute the dominant part of the total potential energy of a particle, the computational efficiency of a simulation can be vastly improved by introducing a cut-off in the pair potential so that each particle can only interact with other particles within a distance r_{cut} (the cut-off distance). In simulations using periodic boundary conditions (section 2.5.1), r_{cut} is typically chosen to be less than half the length of the periodic box so that a particle cannot interact with a periodic image of itself. There are several methods that can be used to truncate the potential. One method is to simply cut the potential at r_{cut} and set it to zero at longer distances:

$$U^{truncated}(r) = \begin{cases} U(r) & r \leq r_{cut} \\ 0 & r > r_{cut} \end{cases}, \tag{2.28}$$

although this results in a discontinuity in the potential at r_{cut}. Another approach is to truncate and shift the potential:

$$U^{trunc-shift}(r) = \begin{cases} U(r) - U(r_{cut}) & r \leq r_{cut} \\ 0 & r > r_{cut} \end{cases}. \tag{2.29}$$

This results in a continuous potential which is much more suitable for molecular dynamics simulations than the truncation in equation 2.28.

Typical values of r_{cut} used for the potentials described in section 2.2 are $2.5\sigma_0$ for the Lennard-Jones potential and $4\sigma_0$ for the Gay-Berne potential. Truncated and shifted potentials are used for the Gay-Berne simulations conducted in chapters 4 and 7 of this thesis.

2.5.3 Radial Distribution Functions

Radial distribution functions are used to characterise the structures of phases in computer simulation. They can also be obtained from neutron scattering data (requiring a Fourier transform of the structure factor) for experimental systems. The simplest distribution function is the pair distribution function, known as $g_2(\mathbf{r}_i, \mathbf{r}_j)$ or just $g(r)$. $g(r)$ is defined as the probability of finding a pair of atoms at a distance r apart, relative to the probability that would be expected in an ideal gas (completely random distribution) at the same density. It is defined as:

$$g(r) = \frac{V}{N^2} \left\langle \sum_i \sum_{j \neq i} \delta(\mathbf{r} - \mathbf{r}_{ij}) \right\rangle, \tag{2.30}$$

where V is the volume and N is the number of particles. In computer simulations the δ function is replaced by a non-zero function in a small range of separations, δr, and histograms are compiled for each separation. The radial distribution function for a Lennard-Jones liquid close to its triple point is shown in figure 2.7.

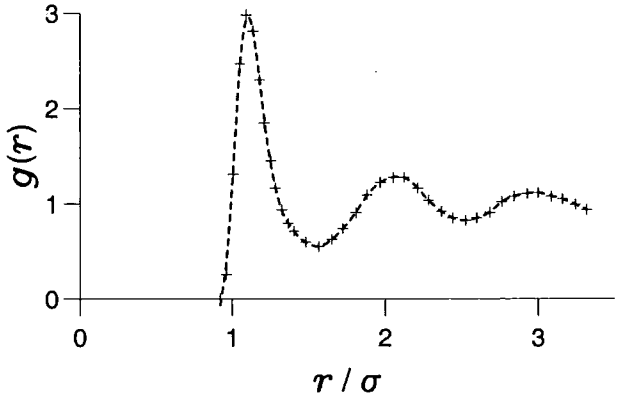

Figure 2.7: The pair distribution function for a Lennard-Jones fluid close to the triple point (adapted from reference[112]).

It can also be useful to resolve the distribution into parts that are parallel, $g_{\parallel}(r)$, and perpendicular, $g_{\perp}(r)$, to the director in the study of liquid crystalline materials. Peaks in $g_{\parallel}(r)$ indicate that layers have formed in the structure (useful for identifying

smectic phase formation) while $g_{\perp}(r)$ can be used to monitor the ordering within layers (useful to differentiate between smectic-A layers and soft-crystalline layers).

Orientational correlation functions (OCFs) can also be used to calculate structural features. The OCF of rank l is defined as:

$$g_l(r) = 1 + \frac{1}{N}\left\langle \sum_i \sum_{j \neq i} P_l(\cos \gamma_{ij}) \right\rangle, \tag{2.31}$$

where P_l is the lth Legendre polynomial and γ_{ij} is the angle between the orientational vectors of molecules i and j. The OCF of rank 2 can be used as a measure of the distance dependence of the order parameter.

Chapter 3

Computer Simulations of Soft Repulsive Spherocylinders (SRS)

3.1 Introduction

Recent years have seen substantial progress in the simulation of liquid crystal systems.[113–115] Such simulations frequently require large numbers of mesogenic molecules. This is particularly true for the calculation of material properties, such as elastic constants that require the computation of a wavevector-dependent ordering tensor in the low-k limit,[116,117] or for the study of smectic phases where many particles are required to represent individual smectic layers. In these cases it is desirable to use models that are cheap, in terms of computer power, but which still capture the essential physics of real mesogenic molecules.

The most commonly studied model systems are the hard spherocylinder model[46,47] and the soft-particle Gay-Berne mesogen[41–43] (see section 2.2.4). In this chapter, computer simulations of a "hybrid" system of soft repulsive spherocylinders (SRS), which have only been briefly examined in the past,[49–51] are carried out in order to determine the phase behaviour of the system. The computational model is appealing due to its relative cheapness but in this work is shown to be rich in phase behaviour, exhibiting both the nematic and smectic liquid crystalline phases. In addition the short-range nature of this potential makes it highly suitable for use with parallel domain decomposition algorithms[109,110,118] (see section 2.4.4), which can provide for

the simulation of extremely large systems of mesogenic molecules.[119]

3.2 Model and Simulation Details

We consider a system of 675 spherocylinder molecules with a purely repulsive short range pair potential of the form

$$U_{ij} = \begin{cases} 4\varepsilon \left[\left(\frac{\sigma_0}{d_{ij}} \right)^{12} - \left(\frac{\sigma_0}{d_{ij}} \right)^{6} + \frac{1}{4} \right], & d_{ij} < d_{cut} \\ 0, & d_{ij} \geq d_{cut} \end{cases} \tag{3.1}$$

where $\sigma_0 = D$, the diameter of the spherocylinder, d_{ij} is the shortest separation between hard lines of length L that run through the middle of each spherocylinder (figure 3.1) and $d_{cut} = 2^{\frac{1}{6}}\sigma_0$. In this study spherocylinders with aspect ratio $\frac{L}{D} = 4$ (total length-to-breadth ratio of 5:1) were used. Hard spherocylinder particles have already been shown to form nematic and smectic phases for this aspect ratio. Figure

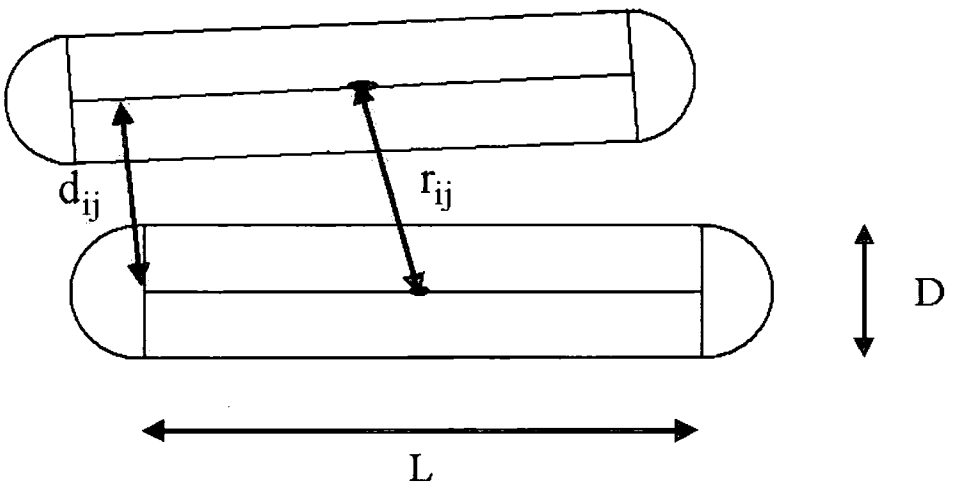

Figure 3.1: Schematic diagram defining distances r_{ij}, d_{ij}, D and L for spherocylinders.

3.2 shows the form of the potential as a function of intermolecular separation, r_{ij}, for different fixed orientations of pairs of spherocylinders, and figure 3.3 shows a three dimensional contour plot of the potential energy for a pair of spherocylinders constrained to lie parallel.

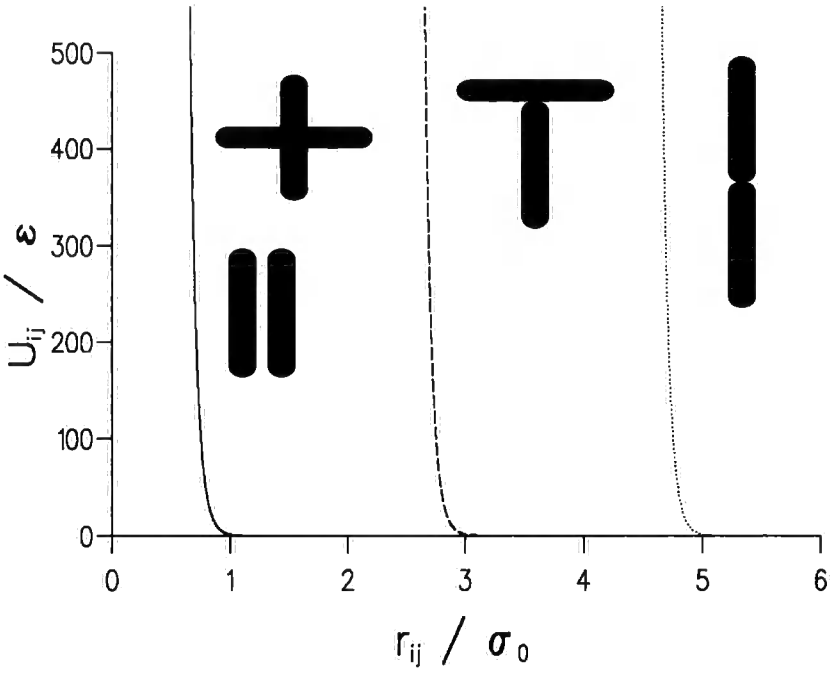

Figure 3.2: The spherocylinder pair potential, U_{ij}, as a function of the fixed relative orientations of two particles at separation r_{ij}.

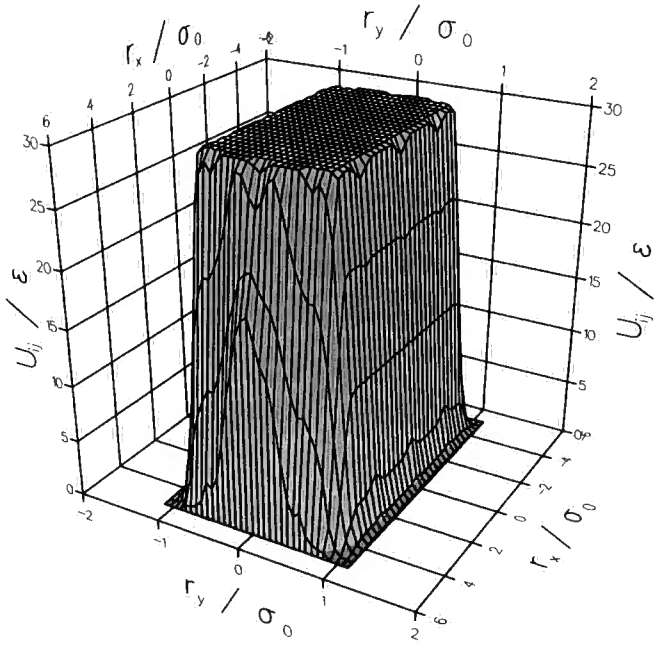

Figure 3.3: 3-D contour plot of the pair potential, U_{ij}, for two spherocylinders constrained to lie parallel to the y-axis at separation $(r_x, r_y, 0)$, $r_{ij} = \sqrt{r_x^2 + r_y^2}$.

The spherocylinder molecules were initially placed, completely aligned, in a simulation box of cubic dimensions subject to periodic boundary conditions. A molecular dynamics (MD) simulation using a Nosé-Hoover thermostat NVT ensemble was used to 'melt' the system until the isotropic phase was obtained. The NVT ensemble was then used to sequentially reduce the temperature of the system to desired levels. Equilibration was generally achieved at each temperature after 1-5 $\times$ 10^5 steps. Finally, MD simulations in the NVE ensemble were used to equilibrate the sample at each state point and to find the average temperature, pressure and order parameter, S_2, for the system over a production run (0.5-2 $\times$ 10^5 steps) where S_2 is defined as

$$S_2 = \frac{1}{N}\sum_{i=1}^{N} P_2(\widehat{\mathbf{u}}_i.\mathbf{n}), \tag{3.2}$$

where $\widehat{\mathbf{u}}_i$ is the unit vector that specifies the orientation of the long axis of molecule i, $\mathbf{n}$ is the director which is a unit vector specifying the average alignment of the long molecular axes and P_2 is the second Legendre polynomial $P_2(\cos\theta) = \frac{1}{2}(3\cos^2\theta - 1)$. S_2 was calculated as the largest eigenvalue obtained through diagonalization of the ordering tensor

$$Q_{\alpha\beta} = \frac{1}{N}\sum_{i=1}^{N}(\frac{3}{2}\widehat{u}_{i\alpha}\widehat{u}_{i\beta} - \frac{1}{2}\delta_{\alpha\beta}), \tag{3.3}$$

where δ is the Kronecker δ and $\alpha, \beta = x, y, z$ refer to the space fixed axes. Uncertainties were found by performing standard error calculations on the data collected during these production runs. The system generally took longer to equilibrate near phase boundaries, especially when close to the isotropic-nematic transition (typically 1-1.5 $\times$ 10^5 steps longer).

A *velocity Verlet* algorithm was used for integration of the equations of motions using a reduced time-step of $0.0003 < \delta t^* \leq 0.001$ ($t^* = (\epsilon/(m\sigma^2))^{1/2}t$). The actual time-step used for each state point depended on the temperature and density of the system studied, with higher temperature state points requiring shorter time-steps. In each case the stability of the integration algorithm was checked and no significant drift in the total energy was seen in the NVE ensemble. The spherocylinder system was studied at a number of different densities to allow an approximate phase

diagram of the system to be mapped out. All the MD simulations conducted in this study were done with the MD program GBMOLDD,[109,110,118] which uses the domain decomposition algorithm for parallelisation. Runs were carried out on single workstations and on eight processors of a SUN system. (GBMOLDD is efficient for both single processor systems (single domain) or parallel computer systems. Parallel performance improves with the number of domains. However, the relatively small system size used in this work limits the maximum number of domains to eight.)

To characterize highly ordered systems that form at high densities and/or low temperatures, NpT ensemble (Nosé-Hoover thermostat and Hoover barostat[103,120] in the form proposed by Toxvaerd[106]) simulations were performed on selected state points with $S_2 > 0.8$. This removes problems of two-phase coexistence by not constraining the density of the system and checks whether the presence of smectic phases is influenced by the fixed periodic boundary conditions of the NVE ensemble. In addition, NpT simulations (as previously specified) were carried out for three reduced temperatures ($T^* = 0.5, 1.0, 1.5$) covering a range of reduced pressures from $P^* \approx$1.5-12.5 (see below), which covers the whole phase diagram. In these simulations the SRS system was equilibrated at a low pressure in order to form a disordered isotropic phase. The pressure of the system was then sequentially increased. At each state point the system was equilibrated for approximately 1×10^5 steps and system averages were taken over a further 1×10^5 steps.

The reduced units convention is used throughout this chapter. For the reduced density, $\rho^* = \rho\sigma_0^3$, the reduced temperature, $T^* = \frac{kT}{\varepsilon}$ and the reduced pressure, $P^* = \frac{\nu_0 P}{kT}$, where ν_0 is the volume of a spherocylinder.

3.3 Results and Discussion

The NVE results for the $\frac{L}{D} = 4$ system of soft repulsive spherocylinders are summarized in Table 3.1. For each state point in Table 3.1 the phase has been identified from the degree of orientational order, given by S_2, and the degree of translational order, given by the centre of mass pair distribution function resolved parallel and perpendicular to the direction of orientational order (these functions are described

in chapter 2). In the case of each isochore, reduction in temperature results in the formation of a nematic liquid crystal phase. Figure 3.4 shows the time evolution of the order parameter, S_2, during a typical simulation run ($\rho^* = 0.131857$, $T^* = 1.404$) where the nematic phase is grown directly from the isotropic phase. For $\rho^* = 0.131857$ the nematic phase typically required 1.5-2 $\times$ 10^5 steps to grow completely from the liquid but the number of simulation steps needed for equilibration was highly dependent on the density and temperature at which the simulation was conducted.

Table 3.1: Results for a series of isochores studied in the *NVE* ensemble.

ρ^*	$\langle T^* \rangle$	$\langle P^* \rangle$	$\langle S_2 \rangle$	Phase
0.130	13.892±0.014	5.290±0.024	0.070±0.017	I
0.130	6.943±0.004	6.085±0.032	0.084±0.016	I
0.130	2.798±0.028	7.225±0.119	0.143±0.021	I
0.130	2.100±0.001	7.457±0.011	0.290±0.019	I/N
0.130	1.394±0.001	7.880±0.031	0.296±0.013	I/N
0.130	0.694±0.001	8.329±0.011	0.354±0.013	I/N
0.130	0.345±0.001	8.416±0.069	0.512±0.018	N
0.131857	13.951±0.016	5.512±0.006	0.067±0.020	I
0.131857	7.006±0.006	6.292±0.023	0.063±0.019	I
0.131857	2.791±0.003	7.346±0.027	0.203±0.025	I
0.131857	2.064±0.002	7.844±0.033	0.299±0.015	I/N
0.131857	1.404±0.001	7.966±0.029	0.553±0.018	N
0.131857	1.051±0.001	8.029±0.017	0.724±0.011	N
0.131857	0.685±0.001	7.959±0.015	0.811±0.006	N/Sm-A
0.131857	0.343±0.001	8.275±0.023	0.840±0.004	Sm-A
0.135	13.864±0.012	5.836±0.012	0.079±0.019	I
0.135	6.850±0.004	6.764±0.011	0.103±0.020	I
0.135	3.532±0.026	7.466±0.028	0.351±0.026	I/N
0.135	2.814±0.003	7.595±0.029	0.488±0.034	N
0.135	2.095±0.003	7.927±0.037	0.567±0.015	N

ρ^*	$\langle T^* \rangle$	$\langle P^* \rangle$	$\langle S_2 \rangle$	Phase
0.135	1.410±0.002	7.868±0.045	0.752±0.018	N
0.135	1.052±0.001	7.928±0.026	0.805±0.006	N
0.135	0.679±0.001	7.962±0.031	0.844±0.008	Sm-A
0.135	0.345±0.001	8.465±0.013	0.877±0.003	Sm-A
0.140	13.897±0.008	6.451±0.017	0.077±0.019	I
0.140	7.420±0.009	7.272±0.020	0.134±0.037	I
0.140	5.000±0.006	7.675±0.020	0.269±0.024	I/N
0.140	3.547±0.004	8.054±0.029	0.463±0.018	N
0.140	2.780±0.003	8.358±0.021	0.480±0.020	N
0.140	2.436±0.003	8.494±0.032	0.548±0.020	N
0.140	2.124±0.003	8.296±0.018	0.664±0.011	N
0.140	1.755±0.003	8.085±0.055	0.786±0.005	N/Sm-A
0.140	1.421±0.001	7.840±0.028	0.872±0.003	Sm-A
0.140	0.692±0.001	8.454±0.021	0.890±0.004	Sm-A
0.145	17.070±0.012	6.746±0.013	0.093±0.009	I
0.145	8.918±0.007	7.624±0.013	0.127±0.025	I
0.145	6.205±0.007	7.989±0.016	0.341±0.022	I/N
0.145	4.823±0.007	8.176±0.035	0.567±0.018	N
0.145	3.416±0.003	8.376±0.025	0.755±0.020	N
0.145	2.087±0.005	8.181±0.063	0.862±0.013	Sm-A
0.145	0.693±0.001	9.025±0.030	0.925±0.002	K
0.150	20.765±0.027	7.019±0.014	0.087±0.016	I
0.150	11.198±0.014	7.818±0.023	0.151±0.026	I
0.150	9.285±0.019	7.973±0.040	0.454±0.022	N
0.150	7.008±0.008	8.356±0.030	0.504±0.012	N
0.150	5.676±0.007	8.391±0.028	0.682±0.009	N
0.150	4.198±0.007	8.578±0.045	0.787±0.011	N/Sm-A
0.150	2.833±0.006	8.338±0.052	0.877±0.008	Sm-A
0.150	1.388±0.001	9.005±0.020	0.916±0.004	K
0.160	40.908±0.032	7.156±0.017	0.116±0.012	I

ρ^*	$\langle T^* \rangle$	$\langle P^* \rangle$	$\langle S_2 \rangle$	Phase
0.160	28.207±0.025	7.688±0.023	0.216±0.038	I/N
0.160	18.402±0.021	8.206±0.025	0.403±0.031	I/N
0.160	14.322±0.024	8.406±0.042	0.584±0.059	N
0.160	10.668±0.019	8.726±0.033	0.696±0.013	N
0.160	8.449±0.017	9.064±0.031	0.746±0.018	N
0.160	6.839±0.028	8.897±0.060	0.827±0.006	N/Sm-A
0.160	3.448±0.004	8.983±0.023	0.917±0.005	K

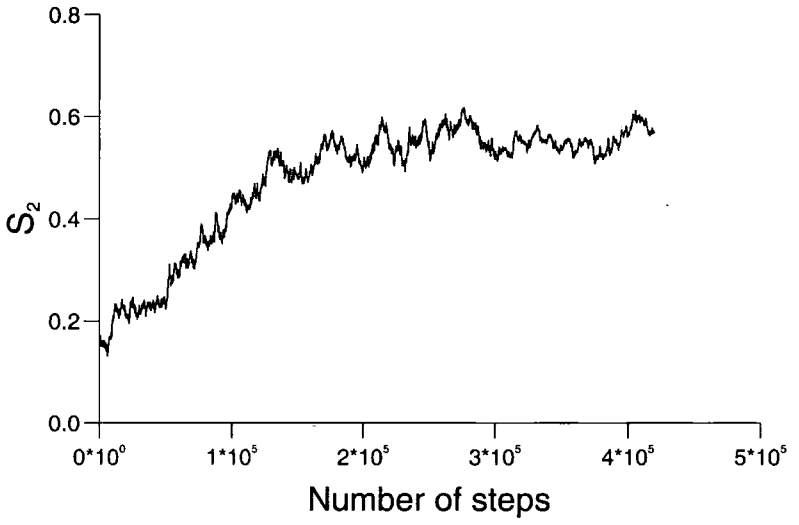

Figure 3.4: A typical S_2 vs. simulation time plot showing the growth of an orientationally ordered nematic phase from an isotropic liquid (for $T^* = 1.404, \rho^* = 0.131857$).

The T^* dependence of S_2 for different reduced densities is plotted in figure 3.5. As density is increased, it is evident that a nematic phase forms at increasingly high temperatures, or conversely, increases in density at fixed temperature lead to nematic formation as predicted by Onsager theory. This behaviour is expected from earlier studies of hard spherocylinder models.[46,47] The work of McGrother *et al.*[46] predicts an isotropic-nematic (I-N) phase transition for aspect ratios of just less than $\frac{L}{D} = 4$, and we would expect the SRS system to exhibit similar trends. In the absence of attractive forces in these models, orientational order is primarily

influenced by the competition between rotational and translational entropy. At higher densities the loss in rotational entropy induced by orientational ordering is more than compensated for by the gain in translational entropy caused by the molecules aligning.

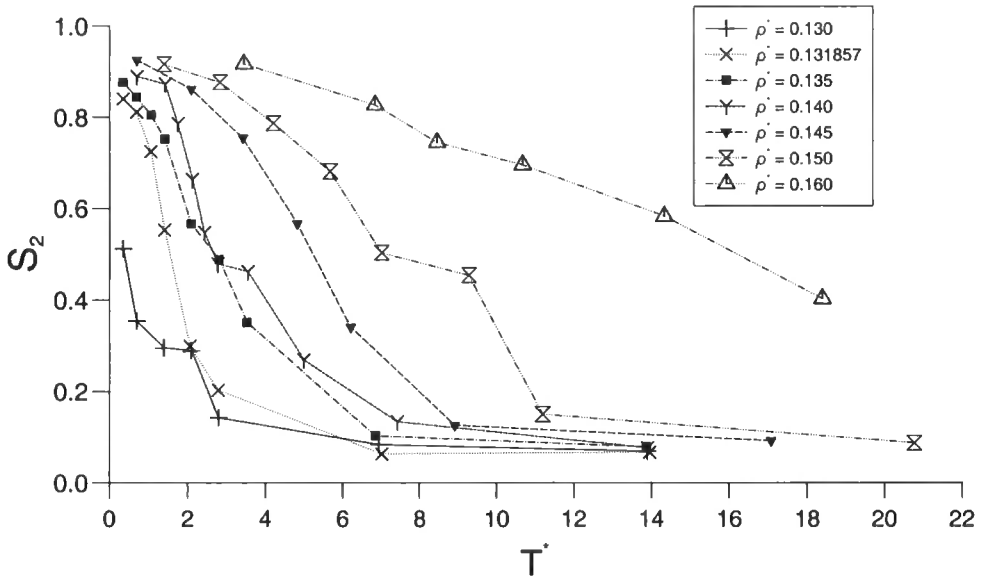

Figure 3.5: S_2 as a function of reduced temperature, T^*, for seven fixed reduced densities, ρ^*, in the NVE ensemble.

With the exception of the lowest density studied, the formation of smectic layers was able to be seen at low temperatures for each of the isochores studied in table 3.1. For fixed periodic boundary conditions the possibility arises that smectic layers can form with a layer structure than is incommensurate with the box dimensions. Consequently, constant pressure runs for some of the low temperature state points from table 3.1 were carried out, to produce the NpT results listed in table 3.2.

The layer ordering was monitored through the behaviour of the radial distribution function $g(r)$, and its components parallel, $g_{\parallel}(r)$, and perpendicular, $g_{\perp}(r)$, to the director (as shown in figure 3.6 for selected state points) and the centre of mass structure factor $S(k)$, where $S(k) = N^{-1} \langle \rho(k)\rho(-k) \rangle$ and $\rho(k) = \sum_{i=1}^{N} \exp(i\mathbf{k}.\mathbf{r}_i)$. The simulations clearly demonstrate the formation of smectic layers with the layer normal parallel to the director resulting in oscillations in $g_{\parallel}(r)$, as shown in figure 3.6b. On cooling from the nematic, the in-plane ordering represented by $g_{\perp}(r)$ is liquid like (as shown in the figure 3.6c), which confirms that the initial phase formed

on cooling the nematic is a smectic-A phase, rather than a smectic-B phase. Again, this result is expected from the behaviour of hard spherocylinders,[46,121] where a smectic-A phase is seen for elongations of $\frac{L}{D} > 3.2$. In table 3.1, it is noted that the transition from a nematic to a smectic-A (N-SmA) phase at constant volume is accompanied by a small drop in pressure. This is indicative of a first order phase transition, again, similar to the behaviour of hard spherocylinder models.[46]

Table 3.2: Results for selected state points in the NpT ensemble.

$\langle\rho^*\rangle$	T^*	P^*	$\langle S_2\rangle$	Phase
0.1301±0.0001	0.6848	7.967	0.753±0.007	N
0.1314±0.0002	0.6850	7.960	0.801±0.016	N
0.1328±0.0002	0.3433	8.264	0.859±0.005	Sm-A
0.1352±0.0002	0.6790	7.963	0.869±0.007	Sm-A
0.1361±0.0001	0.6783	7.967	0.874±0.003	Sm-A
0.1353±0.0001	0.3448	8.470	0.877±0.005	Sm-A
0.1383±0.0002	1.4210	7.841	0.834±0.011	Sm-A
0.1423±0.0002	1.4076	8.049	0.882±0.007	Sm-A
0.1405±0.0001	0.6913	8.470	0.904±0.007	Sm-A
0.1478±0.0002	2.0837	8.238	0.896±0.003	Sm-A
0.1450±0.0001	0.6934	9.039	0.923±0.004	K
0.1477±0.0003	2.8329	8.339	0.865±0.008	Sm-A
0.1531±0.0001	2.8254	8.420	0.902±0.008	Sm-A
0.1506±0.0001	1.3877	9.011	0.917±0.006	K
0.1613±0.0003	6.8333	8.890	0.849±0.018	Sm-A
0.1605±0.0001	3.4434	9.017	0.910±0.006	K

Visualization of snapshots from the simulation also confirm that isotropic, nematic and smectic-A phases were formed (see figure 3.7). However, the simulations are not sufficiently detailed to confidently determine the nature of the highest density phase formed in these systems (where $S_2 > 0.9$). This may be either a smectic-B phase or a solid. An accurate determination of this phase requires free-energy calculations to be performed along with further NpT ensemble simulations on much larger system sizes. Identification of the high density phase is not the main aim of the current work. However, by comparison with hard spherocylinders it is likely that this high density phase is solid.

To aid detailed comparison with previous isothermal-isobaric Monte Carlo work

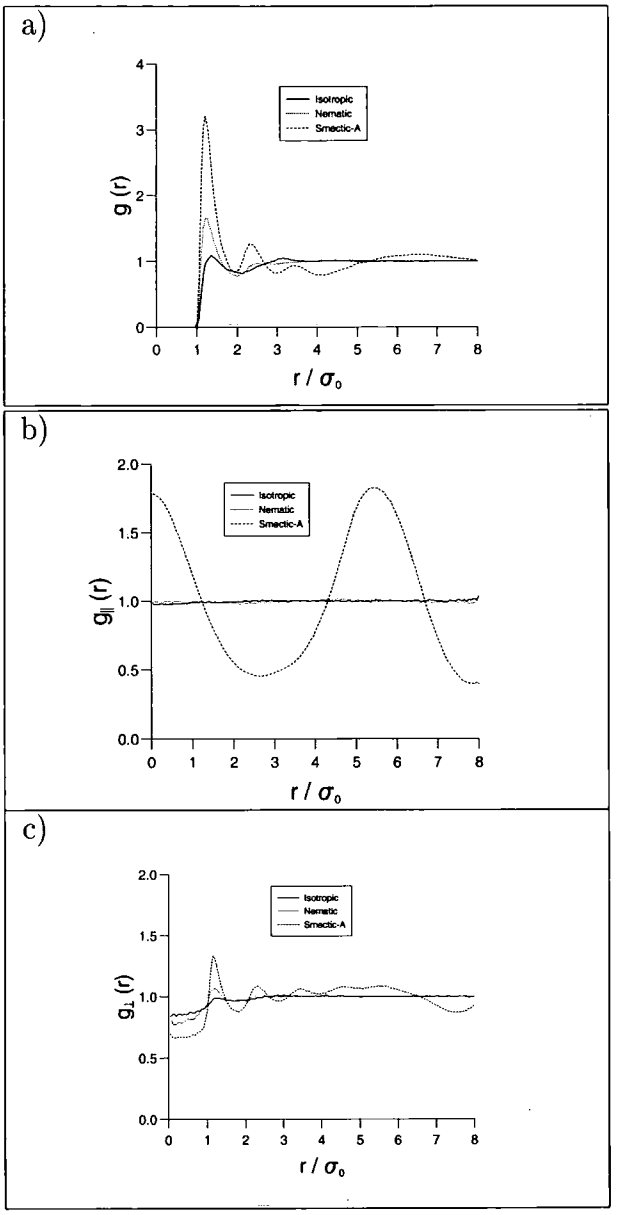

Figure 3.6: Graphs of the pair distribution functions a) $g(r)$, b) $g_{\parallel}(r)$ and c) $g_{\perp}(r)$ in the isotropic phase ($T^* = 0.500, \rho^* = 0.0988, P^* = 4.40$), nematic phase ($T^* = 0.500, \rho^* = 0.1188, P^* = 7.04$) and smectic-A phase ($T^* = 0.500, \rho^* = 0.1302, P^* = 7.77$).

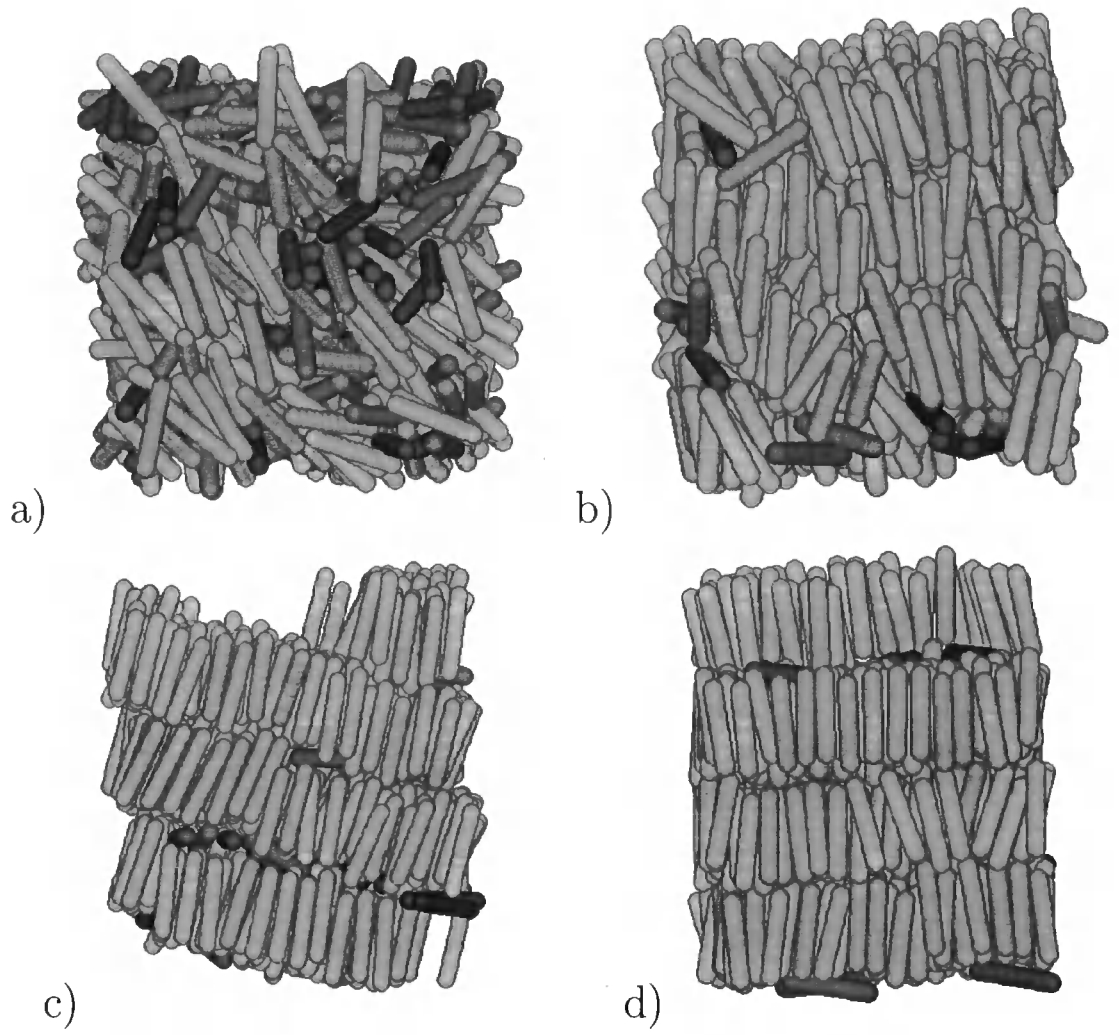

Figure 3.7: Snapshots taken from the a) isotropic ($T^* = 13.95, \rho^* = 0.131857, P^* = 5.51$), b) nematic ($T^* = 1.05, \rho^* = 0.131857, P^* = 8.03$), c) smectic-A ($T^* = 0.345, \rho^* = 0.135, P^* = 8.47$) and d) solid ($T^* = 0.693, \rho^* = 0.145, P^* = 9.03$) phases.

on hard spherocylinders with the same aspect ratio, an additional set of simulations for three isotherms in the NpT ensemble (table 3.3) were carried out. The hard spherocylinder system was found to exhibit a weakly first-order transition from an isotropic phase ($\rho^* \approx 0.129$, $P^* = 7.75$) to a nematic phase ($\rho^* \approx 0.131$, $P^* = 7.80$), and then a transition from a nematic phase ($\rho^* \approx 0.133$, $P^* = 8.00$) to a smectic-A phase ($\rho^* \approx 0.144$, $P^* = 8.20$). In the SRS system at $T^* = 1.0$, there is a transition from the isotropic phase ($\rho^* \approx 0.113$, $P^* = 5.86$) to a nematic phase ($\rho^* \approx 0.119$, $P^* = 6.60$), and then a transition from a nematic phase ($\rho^* \approx 0.129$, $P^* = 7.70$) to a smectic-A phase ($\rho^* \approx 0.137$, $P^* = 8.06$). So in comparison to the hard system, in the SRS fluid at $T^* = 1.0$ the nematic phase is stabilized slightly with-respect-to the isotropic liquid, but destabilized with respect to the smectic-A phase. These results are not surprising because, in comparison to a hard spherocylinder with a cutoff at σ_0, the *soft shoulders* of the SRS mesogen make it slightly larger.

Table 3.3: Results for a series of isotherms studied in the NpT ensemble.

$\langle\rho^*\rangle$	T^*	$\langle P^*\rangle$	$\langle S_2\rangle$	Phase
0.0771±0.0007	0.500	2.200 ±0.122	0.041±0.015	I
0.0928±0.0006	0.500	3.666±0.171	0.050±0.015	I
0.0988±0.0007	0.500	4.398±0.194	0.041±0.015	I
0.1043±0.0006	0.500	5.132±0.210	0.083±0.031	I
0.1078±0.0007	0.500	5.572±0.225	0.210±0.097	I
0.1102±0.0006	0.500	5.865±0.234	0.336±0.073	I
0.1135±0.0006	0.500	6.305±0.240	0.401±0.058	N
0.1148±0.0010	0.500	6.598±0.266	0.369±0.087	N
0.1188±0.0008	0.500	7.038±0.277	0.575±0.049	N
0.1235±0.0013	0.500	7.331±0.293	0.736±0.029	N
0.1302±0.0010	0.500	7.771±0.311	0.817±0.012	Sm-A
0.1339±0.0009	0.500	8.065±0.317	0.855±0.008	Sm-A
0.1362±0.0008	0.500	8.358±0.326	0.873±0.005	Sm-A
0.1384±0.0007	0.500	8.797±0.329	0.856±0.006	Sm-A
0.1430±0.0008	0.500	9.530±0.374	0.885±0.007	K

$\langle\rho^*\rangle$	T^*	$\langle P^*\rangle$	$\langle S_2\rangle$	Phase
0.1461±0.0008	0.500	10.264±0.367	0.890±0.007	K
0.1529±0.0007	0.500	11.730±0.418	0.899±0.004	K
0.0736±0.0007	1.000	1.833±0.095	0.042±0.015	I
0.0883±0.0007	1.000	2.938±0.138	0.044±0.014	I
0.0958±0.0007	1.000	3.666±0.158	0.058±0.017	I
0.1022±0.0007	1.000	4.399±0.177	0.084±0.028	I
0.1079±0.0007	1.000	5.132±0.202	0.074±0.029	I
0.1133±0.0007	1.000	5.865±0.208	0.113±0.069	I
0.1194±0.0007	1.000	6.598±0.240	0.380±0.049	N
0.1258±0.0007	1.000	7.331±0.259	0.619±0.037	N
0.1294±0.0009	1.000	7.698±0.259	0.702±0.043	N
0.1374±0.0010	1.000	8.064±0.281	0.837±0.010	Sm-A
0.1438±0.0009	1.000	8.797±0.328	0.865±0.006	Sm-A
0.1480±0.0008	1.000	9.530±0.342	0.829±0.027	Sm-A
0.1526±0.0008	1.000	10.264±0.337	0.894±0.005	K
0.1561±0.0008	1.000	10.996±0.401	0.885±0.019	K
0.1644±0.0016	1.000	12.462±0.425	0.901±0.028	K
0.0840±0.0008	1.500	2.444±0.118	0.035±0.013	I
0.0954±0.0007	1.500	3.421±0.143	0.045±0.014	I
0.1081±0.0007	1.500	4.887±0.184	0.051±0.015	I
0.1158±0.0008	1.500	5.865±0.215	0.156±0.050	I
0.1198±0.0009	1.500	6.354±0.230	0.262±0.070	I
0.1240±0.0007	1.500	6.843±0.237	0.429±0.039	N
0.1278±0.0009	1.500	7.331±0.255	0.500±0.074	N
0.1325±0.0010	1.500	7.820±0.282	0.671±0.037	N
0.1438±0.0010	1.500	8.309±0.281	0.863±0.008	Sm-A
0.1534±0.0009	1.500	9.776±0.515	0.886±0.007	K
0.1607±0.0008	1.500	10.753±0.410	0.890±0.005	K

In figure 3.8 the nematic order parameter for the isotherms $T^* = 0.5, 1.0$ and

1.5 are plotted. As the temperature is increased both transitions are pushed to higher densities. However, unlike Gay-Berne particles where attractive forces exist, the extent of the nematic range is not influenced strongly by moving to higher temperature isotherms (for a comparison see figure 13 of reference[122] for isotherms of an elongated Gay-Berne potential (4:1)). From estimates obtained from table 3.3 and the work in reference,[122] it appears that the density change at the phase transition is smaller for the SRS system than for a 4:1 Gay-Berne potential. This is encouraging because typical experimental density changes at a phase transition are usually small in comparison to those predicted by simulations of single site models.

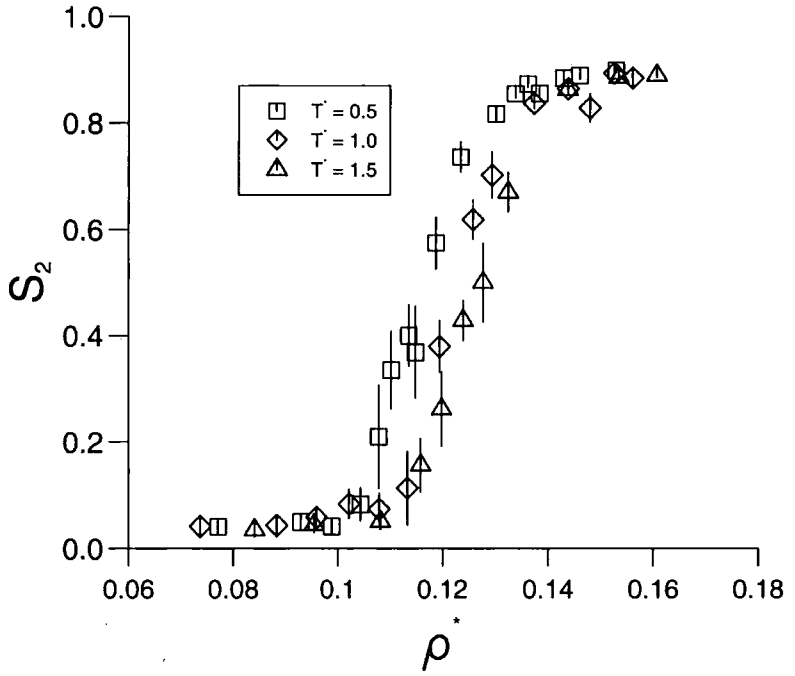

Figure 3.8: S_2 as a function of reduced density, ρ^*, for isotherms at $T^* = 0.5, 1.0, 1.5$ in the NpT ensemble.

Other variations of the spherocylinder model have also been looked at.[123–125] One notable study involved the simulation of dipolar hard spherocylinder (DHSC) systems.[123] A detailed comparison of the SRS and DHSC models is difficult, because there is no published data for DHSCs with an aspect ratio of 4. However, it is interesting to note that dipoles were found to destabilize the nematic phase with respect to both the isotropic and smectic-A phases in contrast to the work described in the current study.

In view of the interest in the SRS potential as a reference system for the large scale simulation of liquid crystal phases, it is of some curiosity to compare the computational cost of the SRS potential with other well-known continuous single-site potentials. The most common of these, in recent years, has been the Gay-Berne potential. However, a detailed comparison with this potential is extremely difficult because the speed of the program depends upon the time-step used, the cutoff employed, whether or not the potential is shifted (such that corrections are computed at the cutoff), the density of the system and the phase the system is in (for example the SRS requires less computational effort for a time-step in the nematic phase than in the isotropic phase). In turn the phase behaviour, the time-step and the cutoff are all governed by the length of the molecule. Despite these provisos it is noted that for the program GBMOLDD, the SRS potential is approximately two to three times faster to compute than the commonly used 3:1 Gay-Berne potential of de Miguel *et al.*[42] for a typical nematic.

After this study was completed further work based on this model system, at the same aspect ratio, was conducted by Cuetos *et al.* at $T^* = 20$[126] and $T^* = 5$.[127] At these higher temperatures both the I-N and N-SmA transitions were found to be shifted towards higher densities with respect to the hard spherocylinder fluid in contrast to the results presented in this chapter for $T^* = 1$. This can be explained by considering the effective size of the molecules at different temperatures. At $T^* = 1$ the molecules are effectively larger and at $T^* > 5$ they are effectively smaller in comparison to a hard spherocylinder molecule. Thus, at higher temperatures the magnitude of the entropic excluded volume effects are smaller than in the hard spherocylinder fluid.

3.4 Conclusion

In this work the results of computer simulations of soft repulsive spherocylinders of aspect ratio $\frac{L}{D} = 4$ using the molecular dynamics program GBMOLDD have been presented. The results show that systems of soft repulsive spherocylinders can form stable nematic and smectic-A liquid crystalline phases. The relative cheapness of

the computational model used make soft repulsive spherocylinders an ideal reference system for future work. In addition, the continuous nature of the potential and the lack of long-range attraction makes it a highly suitable model for use in parallel domain decomposition molecular dynamics programs,[109,110,118] thereby facilitating the simulation of large numbers of particles on multi-processor computers. The SRS solvent system is implemented in helical twisting power (HTP) calculations in chapter 4 of this report.

Chapter 4

Helical Twisting Power (HTP) Calculations from Chemical Potential Differences Between Enantiomers

4.1 Introduction

In section 1.3 the helical twisting power, β_M, for liquid crystalline chiral dopants is introduced. The first technique that is used to calculate helical twisting powers (HTPs) for chiral molecules in this thesis, uses a method originally proposed and applied by Cook and Wilson[31] that was based on some earlier work by Allen.[32] This method involves simulations of a chiral dopant molecule in a twisted nematic solvent using an efficient Monte Carlo (MC) simulation program. The MC simulations are used to compute the difference in chemical potential, $\Delta\mu$, between a chiral solute and its enantiomer immersed in the same twisted nematic solvent. $\Delta\mu$ is directly proportional to β_M, and, given a value for the twist elastic constant, K_2, an absolute value for β_M can be predicted.

The work presented in this chapter is mainly based upon the Cook/Wilson method with the main difference being the use of a generic solvent composed of soft repulsive spherocylinder (SRS) molecules (see chapter 3), as well as Gay-Berne[41] molecules (see section 2.2.4), and the investigation of the optimum pathway of carrying out the calculation. The SRS potential is computationally efficient, usually

requiring 2-3 times less computer power than the more familiar single-site Gay-Berne model. It is therefore a useful solvent to employ in the calculation of helical twisting powers. Also, in many cases HTP values do not depend critically on the nature of the solvent. To try and improve on the original free energy difference (chemical potential) calculations of Cook and Wilson,[31] investigations into different methods of calculating free energy differences have been undertaken and are presented in section 4.4.2.

4.2 Theory

4.2.1 Derivation of the microscopic HTP, β

When the concentration of chiral dopant is small, then, following the de Gennes definition,[128] the equilibrium wavevector, k_0, of the twisted phase is linearly dependent on the concentration of solute molecules

$$k_0 = \frac{2\pi}{P_0} = 4\pi\beta\rho. \tag{4.1}$$

Here, $\rho = N/V$ is the number density of dopant molecules and the constant of proportionality β is defined as the *microscopic* helical twisting power.[128] (It should be noted that de Genne's definition of β is not the same as that of the usual quantity β_M of equation 1.3 that is measured experimentally, but β can easily be converted into β_M using equation 4.5 below.) If a uniformly twisted nematic with wavevector $k = 2\pi/P$ is doped with small numbers (N_+ and N_-) of a chiral dopant (with a microscopic HTP of $\pm\beta$), then there will be an elastic contribution to the free energy that arises from distortions from the uniformly twisted state[32]

$$F = \frac{1}{2}VK_2\left(k - \frac{4\pi\beta}{V}\left[N_+ - N_-\right]\right)^2, \tag{4.2}$$

where V is the volume of the system and K_2 is the twist elastic constant. Following Allen,[32] in the limit of infinite dilution ($N_-, N_+ \to 0$),

$$\mu_- - \mu_+ = \frac{\partial F}{\partial N_-} - \frac{\partial F}{\partial N_+} = 8\pi\beta K_2 k, \tag{4.3}$$

so that

$$\beta = \frac{\Delta\mu}{8\pi K_2 k}. \tag{4.4}$$

Hence, (for low values of k) in the low concentration limit, β can be obtained from a measurement of the chemical potential difference between two enantiomers in a uniformly twisted nematic solvent with a twist elastic constant of K_2.

The microscopic HTP, β, is related to the macroscopic HTP, β_M, by combining equations 1.3, 4.1 and 4.4:

$$\beta_M = \frac{2\rho\beta}{c_w}. \tag{4.5}$$

Allen[32] has used equation 4.4 to obtain values of β for dimers consisting of two touching prolate ellipsoids of axial ratio $e = 5$ within a fluid of similar monomeric ellipsoids. In that work an explicit expression was obtained for the excess chemical potential of a dimer composed of two hard ellipsoids in contact in a twisted nematic phase of hard ellipsoids.[129] However, equation 4.4 is not restricted to systems where explicit expressions can be derived for the chemical potential. For example, $\Delta\mu$ is equivalent to the free energy change in converting one mole of chiral solute into its mirror image in the presence of a twisted nematic solvent at infinite dilution. An overview of free energy calculation techniques is given in section 4.2.3 and the methods used to calculate β in this chapter are presented in section 4.4.

4.2.2 Twisted Periodic Boundary Conditions

In order to carry out a helical twisting power calculation using equation 4.4 it is necessary to simulate a uniformly twisted nematic solvent. To do this the twisted periodic boundary conditions of Allen and Masters[130] can be employed (see figure 4.1). Here, molecules in the neighbouring simulation box ($+z$ direction) are rotated through 90 degrees about the z axis with respect to their coordinates and

orientations in the original box, (and those in the neighbouring box in the opposite $(-z)$ direction are rotated through -90 degrees). For the reduced temperatures at which the simulations were conducted, the twist imposed by the periodic box did not have any significant effect on the ordering of the model fluid. Using Monte Carlo simulations of the SRS and GB fluids essentially identical results for the nematic order parameter in an untwisted system and the chiral nematic order parameter (see below) in a 90 degrees twisted system were obtained. The values of these order parameters were in agreement with the molecular dynamics results of chapter 3 for the SRS fluid and with those given in reference[131] for the GB fluid.

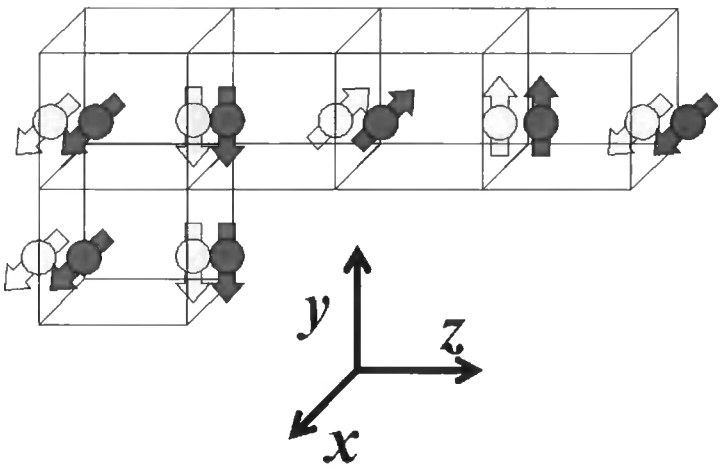

Figure 4.1: Twisted periodic boundary conditions. The diagram shows how the orientation of a molecule passing through the $+z$ direction of the simulation box is rotated by 90 degrees when it enters the periodic box from the -z direction.

Chiral Nematic Order Parameter

The chiral nematic order parameter is obtained by effectively rotating each particle by an angle proportional to its z co-ordinate in the simulation box, and then calculating the order parameter using the standard method described in section 3.2. If θ is the twist imposed on the simulation box ($\pi/2$ in this case), $z(i)$ is the z co-ordinate of molecule i, box$z$ is the length of the simulation box in the z direction, and $\mathbf{e}_{x,y,z}(i)$ is the x, y or z component of the unit vector defining the orientation of

particle i, then new orientations after rotation, $\mathbf{e}_{xnew,ynew,znew}(i)$, are defined by:

$$\mathbf{e}_{xnew}(i) = \mathbf{e}_x(i).\cos(\phi(i)) + \mathbf{e}_y(i).\sin(\phi(i)), \tag{4.6}$$

$$\mathbf{e}_{ynew}(i) = \mathbf{e}_y(i).\cos(\phi(i)) - \mathbf{e}_x(i).\sin(\phi(i)), \tag{4.7}$$

$$\mathbf{e}_{znew}(i) = e_z(i), \tag{4.8}$$

where

$$\phi(i) = \theta \times \left(\frac{z(i)}{\mathrm{box}z}\right). \tag{4.9}$$

This rotation is only a mathematically convenient way of calculating the order parameter for a twisted system within a sub-routine, and the particles are never physically rotated in the actual simulation box.

4.2.3 Free Energy Calculations

The accurate calculation of free energy differences is one of the main aims of both computational and experimental chemists. This is because most of the physical properties of a system depend on its free energy. Now, the excess Helmholtz free energy is given by

$$A = -k_B T \ln Z, \tag{4.10}$$

where Z is the partition function and can be written as

$$Z = \frac{1}{(8\pi^2 V)^N} \int \exp\left[\frac{-E(X)}{k_B T}\right] dX, \tag{4.11}$$

where $E(X)$ is the configurational energy, integrated over the phase space of the system, dX. Following reference,[132] by generating an expression equal to 1

$$1 = \frac{1}{(8\pi^2 V)^N} \int \exp\left[\frac{E(X)}{k_B T}\right] \exp\left[\frac{-E(X)}{k_B T}\right] dX, \tag{4.12}$$

and substituting this expression into equation 4.10 with inversion of the logarithm, the following expression is obtained:

$$A = k_B T \ln \left[\int \exp \left[\frac{E(X)}{k_B T} \right] P(X) dX \right], \tag{4.13}$$

where $P(X)$ is the probability function for the system. This can also be written as

$$A = k_B T \left\langle \exp \left[\frac{E(X)}{k_B T} \right] \right\rangle, \tag{4.14}$$

where the diagonal brackets denote an ensemble average. Expanding equation 4.14 in a Taylor series gives

$$A = \langle E(X) \rangle - \frac{\langle E(X) \rangle^2}{2! k_B T} + ... \tag{4.15}$$

Convergence of this expression will be very slow as higher energy terms, which Monte Carlo and molecular dynamics techniques specifically neglect, are important in the $\langle E(X) \rangle^2$ and higher terms. Hence, calculating the exact free energy from equation 4.14 by simulation is not possible.

For this reason the term 'Free Energy Calculations' normally means the calculation of the free energy difference between two different systems, which is given by

$$\Delta A = -k_B T \left(\frac{Z_1}{Z_0} \right), \tag{4.16}$$

where Z_1 and Z_0 are the partition functions for systems 1 and 0. Using a similar method to that used in deriving equation 4.14, the free energy difference can be expressed as

$$\Delta A = -k_B T \ln \left\langle \exp \left[\frac{-\Delta E(X)}{k_B T} \right] \right\rangle_0, \tag{4.17}$$

which means that the free energy difference between systems 0 and 1 can be determined as an ensemble average over representative configurations of system 0. This is a canonical average that can be measured during an ordinary Monte Carlo run (see chapter 2). Thus, ΔA can be determined using computer simulations.

There are many different methods of calculating free energy differences. The most popular of these include free energy perturbation theory,[133] thermodynamic integration,[134,135] particle insertion,[136,137] particle deletion[137,138] and those based on

Bennett's acceptance ratio method.[138,139]

Free Energy Perturbation Theory

In free energy perturbation theory the difference in free energy between two states, namely system A and system B, is given by:

$$\Delta F_{A\rightarrow B} = -k_B T \ln \left\langle \exp \left[\frac{-(E_B - E_A)}{k_B T} \right] \right\rangle_A \tag{4.18}$$

where $(E_B - E_A)$ is the total potential energy difference between the two systems. In practical terms, if we are making a change to a solute molecule in a large volume of solvent then to calculate the free energy difference for this change we only need to calculate the changes in the solute-solvent and the intramolecular solute interactions and not the solvent-solvent interactions. However, if the Hamiltonians of the two systems are significantly different from each other then the convergence of ΔF will be very slow as, using equation 4.18, the free energy difference is calculated as a probability of sampling system B from the ensemble in system A. If this is the case then a simulation with a number of intermediate points between systems A and B can be performed where system A is gradually mutated into system B via the use of a coupling parameter, λ. The coupling parameter scales the geometric and potential function parameters, V, of system A into system B in the following way:

$$V(\lambda) = \lambda V_B + (1 - \lambda) V_A \tag{4.19}$$

where λ is changed from 0 to 1 throughout the simulation in a series of small steps, or windows, often termed λ_i. These intermediate points, defining the free energy pathway, need not have any physical importance, as long as there is good convergence between adjacent simulation windows ensuring an accurate value of the free energy difference is found.

Extensions of the free energy perturbation (FEP) technique include staged particle insertion[136] which is a multi-stage extension of test particle insertion where the free energy difference is calculated for the insertion of a particle into a system, and staged deletion, which is the reverse process to staged insertion. In these sim-

ulations the test particle interaction and size is gradually 'turned-on' (insertion) or 'turned-off' (deletion). Jorgensen and Ravimohan[140] have suggested the method of 'double-wide sampling' where two free energy differences are calculated from one simulation by perturbing the system from the λ_i state to the λ_{i+1} and λ_{i-1} states. In effect, an insertion ($\lambda_i \rightarrow \lambda_{i+1}$) and a deletion ($\lambda_i \rightarrow \lambda_{i-1}$) are attempted at each intermediate point (or window) in the simulation.

Other variants of the FEP approach are Bennett's acceptance ratio method[139] and the weighted histogram analysis method.[138,141,142] In Bennett's method an intermediate reference state is chosen in between each set of λ points in order to maximise the overlap of the probability distributions between the reference and perturbed states by the use of a weighting function. The weighted histogram analysis method uses a single reference state from which FEP calculations are then performed to all of the different λ states.

Thermodynamic Integration

In thermodynamic integration the free energy difference is determined by the integrand:

$$\Delta F_{A \rightarrow B} = \int_0^1 \left\langle \frac{\delta V(\lambda, x)}{\delta \lambda} \right\rangle_\lambda d\lambda. \tag{4.20}$$

However, although this integrand is continuous, it is solved by first evaluating the function at a series of discrete points and then using a numerical integration method, such as the trapezoidal rule, to approximate the integral. The thermodynamic integration and thermodynamic perturbation methods are in principle equivalent at the limit of infinite sampling.[143] Approximations occur in both methods due to the use of numerical integration in the integration approach and because the Hamiltonians of adjacent windows in the perturbation approach do not perfectly overlap.

Comments on Free Energy Calculation Techniques

The accuracy of a free energy calculation is crucially dependent on the technique that is used. Kofke and Cummings provide an excellent review of the more spe-

cific case of determining chemical potentials from computer simulation.[144] They note that any staged free energy perturbation method which involves a 'deletion' component is highly prone to a systematic error. They also comment that an ineffective implementation of staged insertion would be to 'turn on' a test-particle by increasing its energy parameter rather than by increasing its diameter. On a more general point they state, as a condition for obtaining the most accurate results, any free energy/chemical potential calculation should always proceed in the direction of decreasing entropy and that, if intermediate windows are used, then the entropy change between these windows should be the same.

The calculations that are carried out in this chapter use the free energy perturbation method to determine free energy differences. Several ways of carrying out the FEP calculations were attempted and these are described in section 4.4.

4.3 Simulation Model

4.3.1 Simulation Methodology

The quantity $\Delta\mu$ in equation 4.4 can be obtained in a number of ways. One simple pathway involves using statistical perturbation theory[140,145] to grow an enantiomer into an excess of twisted nematic solvent and measuring the free energy change for that process, followed by a comparison between this quantity and that obtained for the same calculation on the enantiomer. In the simplest possible case, the internal energy of the combined solvent/solute system can be written as

$$U_{\mathrm{tot}}(\lambda) = U^{solute} + \sum_{i=1}^{N_{solvent}} \sum_{j<i}^{N_{solvent}} U_{ij}^{solvent} + \sum_{i=i}^{N_{solute}} \sum_{j=1}^{N_{solvent}} U_{ij}^{solvent/solute}(\lambda), \quad (4.21)$$

where U^{solute} is the solute energy (a constant for a rigid solute molecule), $U_{ij}^{solvent}$[41] is the solvent interaction energy (in this case given by the SRS interaction energy in equation 3.1) and $U_{ij}^{solvent/solute}(\lambda)$ is the solute-solvent interaction energy. In equation 4.21, the solute has N_{solute} atoms interacting with $N_{solvent}$ solvent molecules, and a coupling parameter λ, which varies between 0 and 1 controls the insertion of the solute molecule into the solvent system. Several different methods of altering

$U_{ij}^{solvent/solute}(\lambda)$ are investigated in this work (see section 4.4).

4.3.2 Monte Carlo Free Energy Calculations

Following equation 4.18, the free energy difference between two systems, A and B, is given by

$$\Delta F_{BA} = -k_B T \ln \langle \exp(-\Delta E_{BA}/k_B T) \rangle_A \tag{4.22}$$

where ΔE_{BA} is the energy difference between A and B and the brackets $\langle \rangle_A$ indicate an ensemble average over a simulation of system A. Equation 4.22 is only useful for two systems with similar Hamiltonians. Consequently the growth of an enantiomer into the twisted nematic solvent must be carried out in a series of separate simulations, using the dimensionless control parameter $0 \leq \lambda \leq 1$ to gradually perturb the system. λ can be used to perturb the system in different ways, several of which are investigated in this chapter (see sections 4.4.1 and 4.4.2). The total free energy change is summed from the individual components measured during each simulation

$$\Delta F^{solvent/solute} = \sum_{i=1}^{n} -k_B T \ln \left\langle \exp\left[-\left(E_{\lambda_i} - E_{\lambda_{i-1}}\right)/k_B T\right] \right\rangle_{\lambda_i}. \tag{4.23}$$

4.3.3 Solvent-Solute Model

The generalised form for the internal energy of a combined solute/solvent system is given in equation 4.21. In the simulations conducted in this chapter, U^{solute} is the energy of the solute molecule in the MM2 force field,[75] and $U_{ij}^{solvent}$ is the solvent-solvent energy represented by either Gay-Berne[41] potentials (see chapter 2) or soft repulsive spherocylinder[48] potentials. The soft repulsive spherocylinder potential used is identical to that studied in chapter 3 where the spherocylinder particles have a total length to breadth ratio of 5:1. The form of $U_{ij}^{solvent/solute}$ and details of the two solvent systems are given below.

Gay-Berne (GB)-Atom Model

In this work the form of the GB potential studied by de Miguel *et al.*[59] is used. In this form of the potential $\mu = 2$, $\nu = 1$, $\sigma_{ee}/\sigma_{ss} = 3$, and $\epsilon_{ee}/\epsilon_{ss} = 1/5$ (these

terms are defined in chapter 2). Following reference,[146] the parameters $\sigma_0^{GB} = 5.7$ Å and $\epsilon_0^{GB} = 3.32576$ kJ/mol are used. This corresponds to a stable nematic liquid crystalline phase at a reduced density of $\rho^* = 0.32$ and a reduced temperature of $T^* = 0.95$.

The form of $U_{ij}^{solvent/solute}$ used in this work is based on the work of Cleaver *et al.*[147] who derived a generalised potential for two unlike GB molecules. This formalism has recently been applied to systems of hybrid Lennard-Jones/GB mesogens.[148,149] The solvent/solute interaction energy ($U_{ij}^{solvent/solute} = U_{ij}^{LJ/GB}$) is given by:

$$\begin{aligned} U_{ij}^{LJ/GB} &= 4\epsilon_0^{LJ/GB}\left[\epsilon^{LJ/GB}(\hat{\mathbf{u}}_j, \hat{\mathbf{r}}_{ij})\right]^{\mu} \\ &\times \left[\left(\frac{\sigma_0^{LJ/GB}}{r_{ij} - \sigma^{LJ/GB}(\hat{\mathbf{u}}_j, \hat{\mathbf{r}}_{ij}) + \sigma_0^{LJ/GB}}\right)^{12}\right. \\ &\left. - \left(\frac{\sigma_0^{LJ/GB}}{r_{ij} - \sigma^{LJ/GB}(\hat{\mathbf{u}}_j, \hat{\mathbf{r}}_{ij}) + \sigma_0^{LJ/GB}}\right)^{6}\right], \end{aligned} \tag{4.24}$$

where

$$\sigma^{LJ/GB}(\hat{\mathbf{u}}_j, \hat{\mathbf{r}}_{ij}) = \sigma_0^{LJ/GB}\left[1 - \chi\alpha^{-2}(\hat{\mathbf{u}}_j.\hat{\mathbf{r}}_{ij})^2\right]^{-\frac{1}{2}}, \tag{4.25}$$

$$\epsilon^{LJ/GB}(\hat{\mathbf{u}}_j, \hat{\mathbf{r}}_{ij}) = \left[1 - \chi'\alpha'^{-2}(\hat{\mathbf{u}}_j.\hat{\mathbf{r}}_{ij})^2\right], \tag{4.26}$$

$$\sigma_0^{LJ/GB} = \left[(\sigma_0^{GB})^2 + (\sigma_0^{LJ})^2\right]^{\frac{1}{2}}, \tag{4.27}$$

$$\epsilon_0^{LJ/GB} = (\epsilon_0^{LJ}\epsilon_0^{GB})^{\frac{1}{2}}, \tag{4.28}$$

and $\chi\alpha^{-2}$ and $\chi'\alpha'^{-2}$ are given by equations (21) and (38) of reference.[147] The values of σ_0^{LJ} and ϵ_0^{LJ} for each atom type are taken from the van der Waals radii and ϵ^* in the MM2 Hill potential.[75]

Soft Repulsive Spherocylinder (SRS)-Atom Model

In the spirit of the SRS potential, the form for the interaction between a solute atom and a solvent molecule follows equation 3.1, where the distance d_{ij} is the shortest separation between a hard line through the middle of the spherocylinder and the centre of the atomic site. The following combining rules are applied:

$$\sigma_0^{solute/solvent} = \frac{\sigma_0^{atom} + \sigma_0^{solvent}}{2}, \tag{4.29}$$

$$\epsilon_0^{solute/solvent} = \sqrt{\epsilon_0^{atom}\epsilon_0^{solvent}}, \tag{4.30}$$

where ϵ_0^{atom} and ${\sigma_0}^{atom}$ values for each atom type in the solute are taken from van der Waals radii and ϵ^* in the MM2 Hill potential.[75] For $\epsilon_0^{solvent}$ a value has been used that scales the desired reduced temperature, T^*, to 400 K. A value of ${\sigma_0}^{solvent} = 5.7$ Å was used to provide a generic solvent with an overall length ($5{\sigma_0}^{solvent} = 28.5$ Å) that is in the typical range for many nematogens. The SRS solvent used is identical to that studied in chapter 3.

4.4 Simulation Details and Results

Calculations were carried out on the molecules shown in figure 4.2. These same molecules have been used in the earlier study by Cook and Wilson using a Gay-Berne solvent.[31] For each molecule, the equilibrium lowest energy structure was computed by carrying out energy minimisation calculations using the MM2 force-field. This geometry was then turned into a Z-matrix prior to the MC calculations, and the exact geometry of the enantiomer was obtained by reversing the signs of the dihedral angles in the Z-matrix. These rigid geometries were then used in the subsequent MC studies. MC simulations were carried out using SRS or GB solvent molecules in a cuboidal cell of dimensions 1:1:2 employing twisted periodic boundary conditions as described in section 4.2.2. In the simulation box, the helical twist occurs about the z axis and the nematic director at any point in space is in the x, y plane. A random rotation/translation of the solute molecule and each of the solvent molecules was attempted during each Monte Carlo cycle. Molecular orientations were represented in terms of quaternions and a random rotation was carried out using the approach described in references[150] and,[151] with move sizes adjusted to give MC acceptance ratios in the range 35-55% during the equilibration phase of the simulation. All simulations were conducted in the NVT ensemble at 400 K.

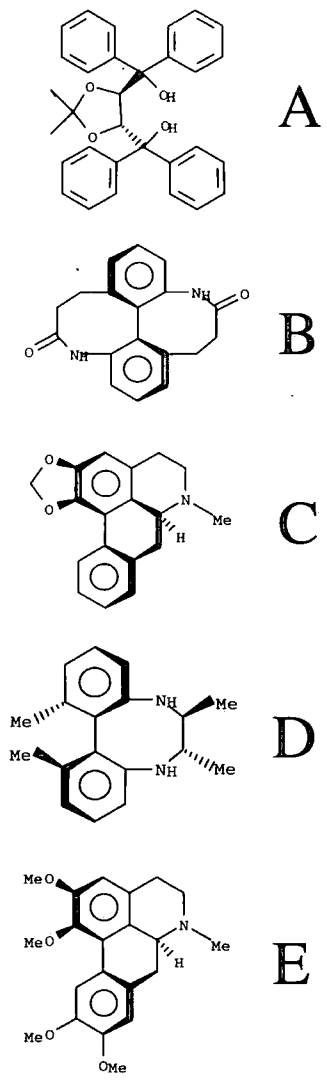

Figure 4.2: Structures of chiral dopant molecules A-E.

4.4.1 Calculations using the SRS solvent system

Two different methods of conducting the free energy perturbation calculations were investigated, namely by scaling the interaction parameters of the solute molecule only (Method A), as used in the original Cook/Wilson technique, and by growing the solute molecule into the simulation box from a point source by scaling both the geometric and interaction parameters of the solute molecule (Method B).

Method A: Free Energy Differences by Scaling Interaction Parameters

These MC simulations were carried out using 505 SRS molecules at a reduced density of $\rho^* = 0.131857$ and a reduced temperature of $T^* = 1.05$. These conditions correspond to a uniform nematic phase with a nematic order parameter of $S_2 = 0.724$ in an untwisted system. Prior to the free energy calculations the solute was introduced into a 'hole' in the solvent, formed by deleting 8 solvent molecules, and the solvent was then equilibrated around the solute molecule for 2×10^5 Monte Carlo cycles. A coupling parameter approach was used to 'turn' on the solute-solvent interactions in the following way:

$$U_{ij}^{solvent/solute}(\lambda) = 4\lambda\epsilon_0^{solute/solvent}\left[\left(\frac{\sigma_0^{solute/solvent}}{r_{ij}}\right)^{12} - \left(\frac{\sigma_0^{solute/solvent}}{r_{ij}}\right)^{6}\right] \quad (4.31)$$

20 λ steps were carried out for each enantiomer (40 λ steps in total for each material). The free energy change was found to be greatest for the initial part of the growth procedure so consequently the largest number of λ values were concentrated on the smallest values of λ. This was achieved by choosing λ_i from the cubic $\lambda_i = (i/20)^3$, $i = 1, 20$. It should be noted that the first step in the simulation is effectively ignored as the solute is already present in the solvent. In this method, the free energy difference between the two enantiomers is assumed to be small, for the initial insertion of the solute into the solvent. 5000 MC equilibration cycles and 25000 MC production cycles were employed at each value of λ.

Method B: Free Energy Differences by Scaling Geometric and Interaction Parameters

Following the arguments made in section 4.2.3, the free energy difference calculation should be carried out by scaling the size of the test-particle as well as its energy parameters. For this reason, simulations have also been conducted using the coupling parameter approach where the coupling parameter scales both the geometric and potential function parameters of the solute molecule. In effect the solute molecule is grown into the SRS solvent system from a point source. These simulations were carried out using 513 SRS solvent molecules at a reduced density of $\rho^* = 0.131857$ and a reduced temperature of $T^* = 1.3$ which corresponds to a point in the middle of the nematic range in an untwisted solvent. Prior to the free energy calculations the solvent was well-equilibrated using 2×10^5 Monte Carlo cycles. 20 λ steps were carried out for each enantiomer (40 λ steps in total for each material). 4000 MC equilibration cycles and 20000 MC production cycles were conducted at each value of λ. λ was scaled equally over the 20 λ steps, where $\lambda_i = (i/20)$, $i = 0, 20$, so that the geometric and interaction parameters were simultaneously turned on by equal amounts throughout the simulation. This was achieved by using λ to scale σ_0^{atom} and $\epsilon_0^{solute/solvent}$.

Results and Discussion

The results of the free energy perturbation calculations for the solute molecules in figure 4.2 using methods A and B are given in tables 4.1 and 4.2 respectively. In each case the free energy change is positive on account of the lack of attractive interactions in the model and the disruption in solvent structure caused by the growth of the solute molecule. This contrasts with free energy perturbation calculations for growth in a Gay-Berne (GB) solvent[31] where the overall free energy change is negative. For GB particles the disruption in solvent structure is more than compensated for by the solute-solvent interaction, which is strongly attractive.

In the case of each molecule a preference for one or other of the enantiomers in terms of the magnitude of ΔF is able to be detected. In each case the smallest free energy change corresponds to the enantiomer that is predicted to induce a helical

Molecule	ΔF/ kJ mol^{-1} for configuration in figure 4.1	ΔF/ kJ mol^{-1} for enantiomer
A	13.9±1.5	14.5±1.1
B	6.1±3.0	8.6±1.2
C	9.0±1.2	9.7±1.3
D	9.5±1.5	8.5±1.4
E	10.7±1.4	10.9±1.4

Table 4.1: Results from simulations using the method A free energy calculation technique and the SRS solvent.

Molecule	ΔF/ kJ mol^{-1} for configuration in figure 4.1	ΔF/ kJ mol^{-1} for enantiomer
A	20.3±0.4	20.9±0.5
B	13.0±0.3	13.9±0.5
C	13.8±0.3	15.1±0.4
D	14.1±0.2	13.8±0.2
E	18.3±0.4	18.3±0.4

Table 4.2: Results from simulations using the method B free energy calculation technique and the SRS solvent.

twist in a nematic solvent with the the same twist sense as the periodic box. The errors for ΔF are rather large for method A and this means that the errors associated with the calculated values of $\Delta\mu$ are large also. Calculated values for $\Delta\mu$ are given in table 4.3 and 4.4 for methods A and B respectively, along with HTP values from experiment. Because the SRS solvent is newly studied, there are (unlike the Gay-Berne solvent) no calculations of the twist elastic constant available. $\Delta\mu$ values have been converted to absolute values of β_M by choosing parameters for the molecular mass of the solvent and K_2 such that they give the best fit to the experimental data. Calculated values of β_M have been included in tables 4.3 and 4.4. Table 4.3 also includes values obtained for a Gay-Berne solvent in the original Cook/Wilson study,[31] using a calculated value for the Gay-Berne twist elastic constant.[117]

Graphs showing the total free energy change for the molecules in figure 4.2 and their enantiomers over the course of a simulation for methods A and B are presented in figures 4.3 and 4.4 respectively.

Molecule	$\Delta\mu$/kJ mol^{-1} for method A	β_M(Comp. SRS)/μm^{-1} for method A	β_M(Comp. GB)/μm^{-1}	β_M(Exp.)/μm^{-1}
A	0.6±1.8	+11±31	+99.3	+104
B	2.5±3.2	+69±88	+69.0	+58
C	0.7±1.8	+22±52	+27.9	+24
D	-1.0±2.1	-30±64	-26.7	-21
E	0.2±2.0	+3±45	0	+8

Table 4.3: Results for $\Delta\mu$ and β_M from simulations using method A. A value of $K_2 = 2.66 \times 10^{-11}$ J m^{-1} and a solvent mass of 249.36 a.m.u. (R.M.M. of 4-n-pentyl-4'-cyanobiphenyl) was used to calculate the β_M values.

Molecule	$\Delta\mu$/kJ mol^{-1} for method B	β_M(Comp. SRS)/μm^{-1} for method B	β_M(Exp.)/μm^{-1}
A	0.61±0.64	+17±18	+104
B	0.97±0.56	+43±25	+58
C	1.30±0.50	+61±23	+24
D	-0.27±0.28	-13±14	-21
E	0.02±0.55	+1±20	+8

Table 4.4: Results for $\Delta\mu$ and β_M from simulations using method B. A value of $K_2 = 1.63 \times 10^{-11}$ J m^{-1} and a solvent mass of 249.36 a.m.u. (R.M.M. of 4-n-pentyl-4'-cyanobiphenyl) was used to calculate the β_M values.

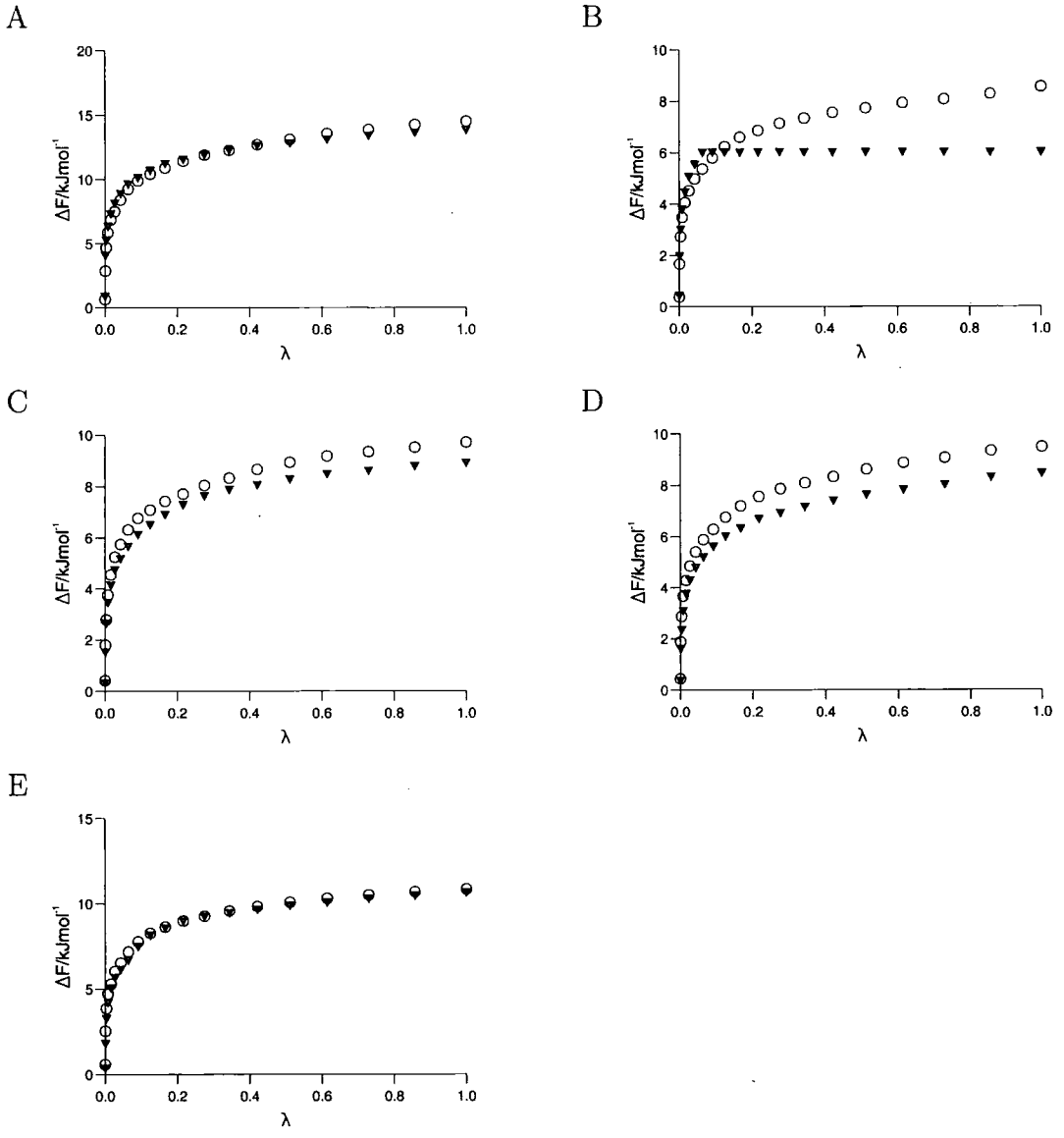

Figure 4.3: Graphs showing the total free energy change for molecules A-E and their enantiomers throughout the simulation where λ scales the interaction parameter, $\epsilon_0^{solute/solvent}$, only (method A). The triangles represent the enantiomer which produces a right-hand twist in the twisted nematic phase and the circles represent the enantiomer which produces a left-hand twist in the twisted nematic phase.

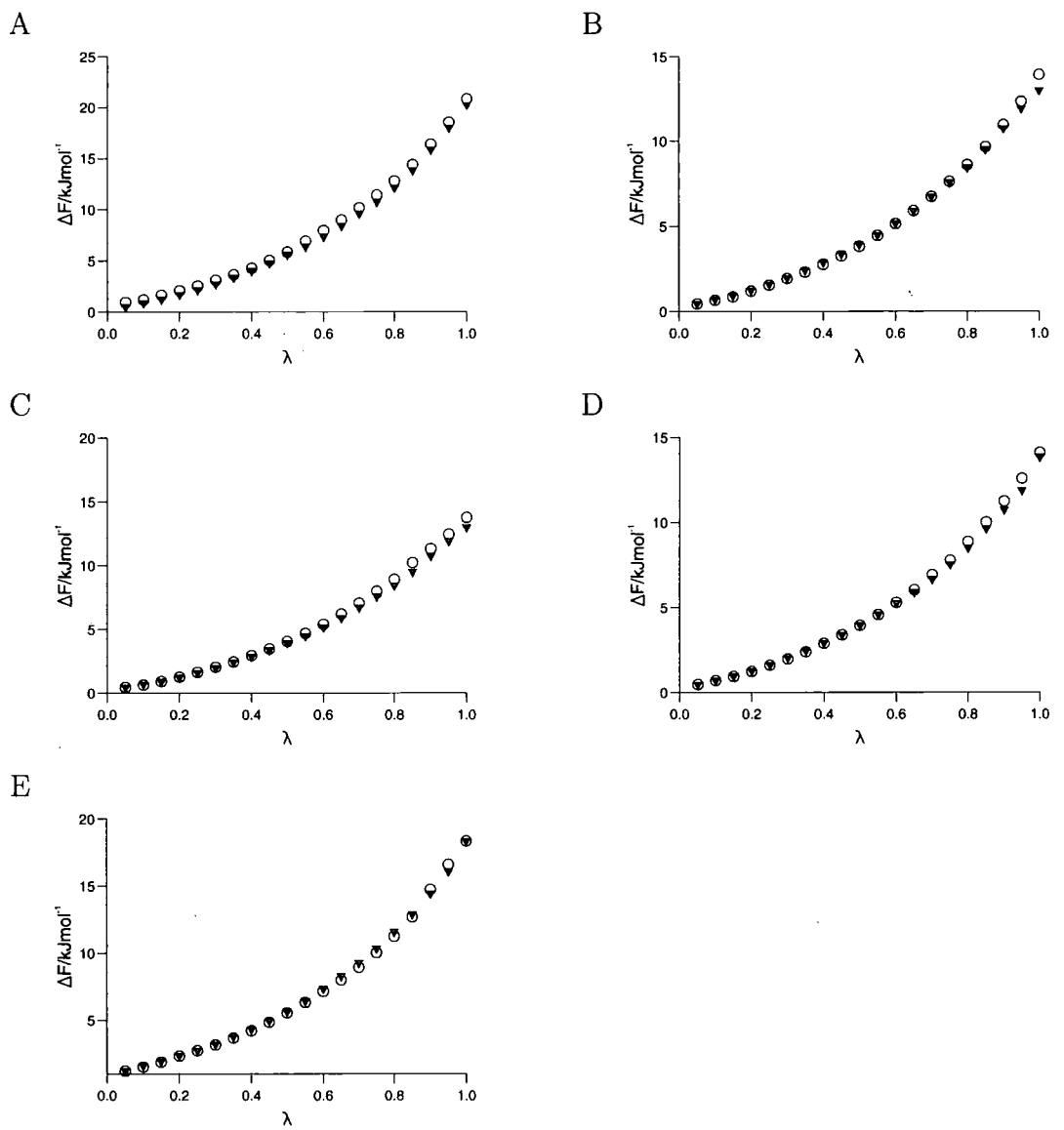

Figure 4.4: Graphs showing the total free energy change for molecules A-E and their enantiomers throughout the simulation where λ scales the geometric and interaction parameters, σ_0^{atom} and $\epsilon_0^{solute/solvent}$ (method B). The triangles represent the enantiomer which produces a right-hand twist in the twisted nematic phase and the circles represent the enantiomer which produces a left-hand twist in the twisted nematic phase.

The results for molecule A using both methods is particularly poor. Subsequent studies in chapters 5 and 6 have shown that the HTP/chirality is highly dependent on the configuration of rings in these molecules (see sections 5.5.4 and 6.3.1). In general, the results for method A are slightly better than those from method B when compared with the experimental HTPs, although the statistical errors using method B are better than those from method A. The sources of statistical errors in the free energy techniques can be examined by analysing the forms of the total free energy change graphs in figures 4.3 and 4.4.

For method A simulations, most of the total free energy change for the simulations occur between $\lambda = \left(\frac{1}{20}\right)^3 \rightarrow \left(\frac{11}{20}\right)^3$ and, after this initial steep rise in free energy, the curve becomes very flat. This suggests that the initial steps in the simulation are the most important and also the most erroneous due to the large free energy changes involved between each step. The first step in all of these simulations appears to be particularly poor. This is probably due to inadequate sampling of the first forward step from $\lambda = \left(\frac{1}{20}\right)^3 \rightarrow \left(\frac{2}{20}\right)^3$. For the method B simulations, the free energy change curves are much smoother and the different λ steps appear to have equal importance in determining the overall free energy change for the insertion of the solute molecule into the SRS twisted nematic system.

For the SRS solvent the predictions for the magnitude of β_M are less impressive than those for the Gay-Berne system using method A. This is most likely to be because the errors for the free energy calculations are much larger for the SRS solvent: the double-wide sampling technique used for a Gay-Berne solvent in reference[31] is not suitable for a harder SRS potential, and the errors in ΔF values must be addressed if this fluid is to be used to provide quantitative predictions for HTPs. In addition the work in reference[31] used double the number of λ steps in the free energy calculation and the simulations were also run for longer at each λ step.

However, there are a number of factors which potentially make the SRS mesogen a good solvent for use in these free energy calculations. Firstly, the SRS potential is 2-3 times computationally cheaper than the Gay-Berne potential. Secondly, the free energy changes for the SRS fluid are not complicated by the long-range attractions of the Gay-Berne potential. Thirdly, it is likely that values of $\Delta\mu$ should be larger for

the SRS fluid than for GB particles in reference,[31] because the longer spherocylinder particles should have a greater nematic twist elastic constant for the state-points studied. However, the latter could be remedied by use of longer Gay-Berne systems or parameterizations of the Gay-Berne potential with larger twist elastic constants. K_2 has yet to be measured independently for the spherocylinder fluid, but could be obtained from monitoring of wavevector-dependent fluctuations in the ordering tensor.[117]

The SRS solvent does have several disadvantages when compared to the GB solvent. Firstly, the GB solvent is able to maintain a more uniform twist over the full length of the simulation box. Secondly, the SRS solvent system is prone to untwisting during simulations when a chiral molecule is inserted. This occurred in approximately one in every three simulations, resulting in the simulations being abandoned and re-run. Here it should be noted that the twisted nematic phase is only meta-stable and the lowest free energy state at the temperatures and densities studied is the nematic phase. This is also the case for the GB solvent but, over a number of simulations, the SRS system has been found to be much less stable. Thirdly, the GB mesogen contains longer-range attractive forces that could be important in ordering liquid crystal molecules around a chiral dopant and in the transmission of chirality from the chiral molecule to the mesophase.

4.4.2 Alternative Methods for Calculating the Free Energy Difference

In order to investigate the optimum pathway for the free energy calculations and to try and reduce the statistical error in the simulations, further studies were carried out using the GB solvent system originally used by Cook and Wilson.[31] Three alternative methods are attempted and the findings are applied to a final set of simulations using the SRS solvent.

Method C: Free energy differences by linear scaling of the geometric and interaction parameters

This method is analogous to that used in method B of the SRS solvent simulations, with the main difference being the separate scaling of the geometric and interaction parameters over different halves of the simulation. Of particular interest in these simulations was which steps gave rise to the largest errors in the free energy difference calculations.

To scale the geometric and interaction parameters in the potential two different lambda parameters were used, λ_i^σ and λ_i^ϵ respectively. If there are n lambda-steps in the simulation then $\lambda_i = i/n$ at lambda-step i. λ_i^σ and λ_i^ϵ can then be defined as:

$$\lambda_i^\sigma = \begin{cases} 0, & i = 0 \\ 2\lambda_i, & 1 \leqslant i \geqslant n/2 \\ 1, & n/2 \leqslant i \geqslant n \end{cases}, \tag{4.32}$$

$$\lambda_i^\epsilon = \begin{cases} 0, & i = 0 \\ 0.01, & 1 \leqslant i \geqslant n/2 \\ 2\lambda_{i-n/2}, & n/2 \leqslant i \geqslant n \end{cases}. \tag{4.33}$$

These can then be used to scale the geometric parameters in equation 4.27 by

$$\sigma_0^{LJ}(i) = \lambda_i^\sigma \sigma_0^{LJ}, \tag{4.34}$$

and the interaction parameters in equation 4.28 by

$$\epsilon_0^{LJ/GB}(i) = \lambda_i^\epsilon \epsilon_0^{LJ/GB}. \tag{4.35}$$

The simulations were carried out using 512 GB solvent molecules at a reduced density of $\rho^* = 0.32$ and a reduced temperature of $T^* = 0.95$ which corresponds to a point in the middle of the nematic range in an untwisted solvent. Prior to the free energy calculations the solvent was well-equilibrated using 2×10^5 Monte Carlo cycles. 40 λ steps were carried out for each enantiomer (80 λ steps in total for each material). 5000 MC equilibration cycles and 50000 MC production cycles

were conducted at each value of λ. Chiral molecules B to E in figure 4.2 were studied (molecule A was not used as work conducted in chapter 5 showed that small changes in the conformation of this molecule can give rise to very different values of chirality/HTP).

Method D: Free energy differences by linear scaling of the geometric and quadratic scaling of the interaction parameters

This method follows the approach of method C with the only difference being the values of λ_i^σ and λ_i^ϵ used to control the insertion of the chiral dopant. In this method the following values were used:

$$\lambda_i^\sigma = \begin{cases} 0, & i = 0 \\ 2\lambda_i, & 1 \leqslant i \geqslant n/2 \\ 1, & n/2 \leqslant i \geqslant n \end{cases}, \tag{4.36}$$

$$\lambda_i^\epsilon = \begin{cases} 0, & i = 0 \\ 0.0025, & 1 \leqslant i \geqslant n/2 \\ 2(\lambda_{i-n/2})^2, & n/2 \leqslant i \geqslant n \end{cases}. \tag{4.37}$$

In this approach a very small value of λ_i^ϵ is used during the growth of the σ_0^{LJ} parameter (equation 4.34) to minimise the error in the first step of the simulation. Quadratic scaling of the λ_i^ϵ parameter is used during the second half of the simulation in an attempt to minimise the errors in the initial increase of λ_i^ϵ. The same simulation conditions were used as in method C.

Method E: Free energy differences by linear scaling of the geometric and interaction parameters using backward simulation steps

In this method, to improve the equilibration of the solvent molecules around the solute the simulation is carried out in a reverse process. Prior to the free energy difference calculations the solute molecule is inserted into the solvent and the solute/solvent system is equilibrated for 100000 MC steps. Now, instead of the simulation proceeding from λ-step $n = 1$, the simulation begins at $n = 40$ and is carried

out in reverse. The following parameters were used for λ_i^σ and λ_i^ϵ:

$$\lambda_i^\sigma = \begin{cases} 0, & i = 0 \\ 2\lambda_i, & 1 \leqslant i \geqslant n/2 \\ 1, & n/2 \leqslant i \geqslant n \end{cases}, \tag{4.38}$$

$$\lambda_i^\epsilon = \begin{cases} 0, & i = 0 \\ 0.001, & 1 \leqslant i \geqslant n/2 \\ 2\lambda_{i-n/2}, & n/2 \leqslant i \geqslant n \end{cases}. \tag{4.39}$$

Again the same simulation conditions were used as in methods C and D.

Method F: SRS solvent using backward simulation steps

This approach combines method B and method E for the SRS solvent system. As in method E, a solute molecule is inserted into the solvent and the solute/solvent system is equilibrated for 100000 MC steps prior to the free energy difference calculations. The simulation then proceeds from $n = 40$ to $n = 1$ but the linear scaling approach of method B is used. 40 λ-steps for each enantiomer are used in the calculations and 2000 MC equilibration cycles and 32000 MC production cycles are conducted at each value of λ. For $n = 40 \rightarrow 35$ and $n = 1$, 64000 MC production cycles are conducted as these steps have the largest free energy differences associated with them. Molecules B-D are studied along with two bridged biaryl molecules (labelled 1 and 7) whose structures can be seen below in figure 4.5.

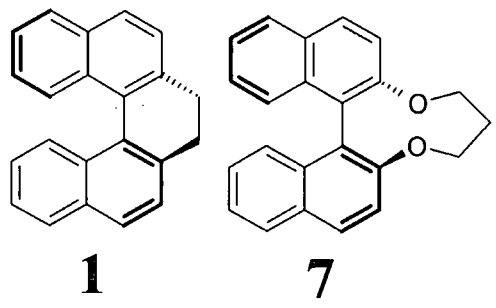

1 **7**

Figure 4.5: Structures of molecules 1 and 7 studied using method F.

Results and Discussion

The results from the simulations using methods C, D, E and F can be seen below in tables 4.7 to 4.10. The results for methods C, D and E are extremely poor, with the wrong sign of twist predicted for some molecules. This suggests that these methods to determine the free energy differences are a bad choice for the GB solvent and that the 'double-wide sampling' method of Jorgensen and Ravimohan,[140] as used by Cook and Wilson,[31] should be applied to this solvent system. For methods C and D, the first step in the simulation had a particularly large error associated with it (average error of ± 0.285 kJ mol^{-1}). This error in the first step was vastly reduced in method E to an average error of ± 0.020 kJ mol^{-1}. The large errors in method E mainly occur during λ-step $n = 21$ of the simulation when λ_i^ϵ is increased from 0.001 to 0.05 (average error of ± 0.24 kJmol^{-1}). Potentially, method E could be used if the scaling of λ_i^ϵ were to be improved (for example by using a quadratic form for the increase of λ_i^ϵ). The simulation could also be altered to run for longer MC steps at λ-steps with particularly large errors. The errors encountered for methods C-E using the GB solvent are clearly far too large to provide any reasonable prediction of β_M. As the difference in the chemical potential of the two enantiomers is expected to be no greater than 0.6 kJmol^{-1}, these errors are clearly unacceptable.

Molecule	ΔF/kJ mol^{-1} for config. in figure 4.1	ΔF / kJ mol^{-1} for enantiomer	$\Delta\mu$/kJ mol^{-1} for method C	β_M(Comp. GB)/μm^{-1} for method C	β_M(Exp.)/μm^{-1}
B	26.58±0.58	26.48±0.54	-0.10±0.79	-18.8±148.7	+58
C	26.94±0.48	28.71±0.53	1.77±0.72	+348.7±141.9	+24
D	27.75±0.47	27.32±0.54	-0.43±0.72	-88.8±148.8	-21
E	30.47±0.63	32.75±0.68	2.28±0.92	+353.0±142.5	+8

Table 4.7: Results for the free energy difference calculations using method C and the GB solvent.

Results from method F are far more encouraging. The statistical errors are much better than those for methods A and B using the SRS solvent and the experimental value of β_M is predicted with an average error of $\pm 17\,\mu$m^{-1} (incidentally, this is also the average statistical error in the predicted value of β_M). Compared to the original

Molecule	ΔF/kJ mol^{-1} for config. in figure 4.1	ΔF / kJ mol^{-1} for enantiomer	$\Delta\mu$/kJ mol^{-1} for method D	β_M(Comp. GB)/μm^{-1} for method D	β_M(Exp.)/μm^{-1}
B	25.20±0.48	26.38±0.46	1.18±0.66	+221.8±124.1	+58
C	27.65±0.51	27.36±0.50	-0.29±0.71	-57.1±139.9	+24
D	26.49±0.46	26.66±0.48	0.17±0.66	+35.1±136.3	-21
E	31.06±0.49	31.11±0.65	0.05±0.81	+7.7±125.4	+8

Table 4.8: Results for the free energy difference calculations using method D and the GB solvent.

Molecule	ΔF/kJ mol^{-1} for config. in figure 4.1	ΔF / kJ mol^{-1} for enantiomer	$\Delta\mu$/kJ mol^{-1} for method E	β_M(Comp. GB)/μm^{-1} for method E	β_M(Exp.)/μm^{-1}
B	25.78±0.46	26.06±0.39	0.28±0.60	+52.6±112.8	+58
C	27.52±0.40	27.45±0.52	-0.07±0.66	-13.8±130.0	+24
D	26.99±0.42	26.73±0.38	-0.26±0.57	-53.7±117.7	-21
E	30.73±0.41	31.86±0.40	-1.12±0.58	-172.5±89.3	+8

Table 4.9: Results for the free energy difference calculations using method E and the GB solvent.

Molecule	ΔF/kJ mol^{-1} for config. in fig. 4.1 and 4.5	ΔF / kJ mol^{-1} for enantiomer	$\Delta\mu$/kJ mol^{-1} for method F	β_M(Comp. SRS)/μm^{-1} for method F	β_M(Exp.)/μm^{-1}
B	13.46±0.09	14.15±0.10	0.69±0.13	+77.5±14.5	+58
C	14.76±0.09	14.85±0.11	0.09±0.14	+10.5±16.0	+24
D	13.98±0.10	13.87±0.11	-0.11±0.15	-13.0±17.9	-21
1	14.13±0.09	14.38±0.10	0.25±0.14	+28.6±16.1	+69
7	15.06±0.11	15.85±0.12	0.78±0.16	+78.6±16.0	+80

Table 4.10: Results for the free energy difference calculations using method F and the SRS solvent. A value of $K_2 = 6.50 \times 10^{-12}$ J m^{-1} and a solvent mass of 249.36 a.m.u. (R.M.M. of 4-n-pentyl-4'-cyanobiphenyl) was used to calculate the β_M values.

Cook/Wilson approach, the simulations are approximately four times quicker, but the accuracy is not as good (β_M is predicted with an average error of $\pm 7\,\mu m^{-1}$ using the Cook/Wilson approach for molecules A-E).

4.5 Conclusions

The results presented in this chapter suggest that using the chemical potential difference between enantiomers in a twisted nematic solvent is a useful theoretical approach for the calculation of helical twisting powers. For the materials studied, the correct sign of the helical twisting power has been calculated for the molecules studied, which is an important prediction in its own right. The results obtained for β_M using the optimised free energy pathway and the SRS solvent are not quite as impressive as those from the original Cook/Wilson approach but the results are obtained at 25% of the computational cost (simulation time for the calculation for each enantiomer is approximately two days on a workstation CPU using the SRS solvent). Errors in the magnitude of the calculated β_M using this method are still too large to provide an accurate magnitude of the HTP and require further investigations to improve them to the point where the method could be used for predictive purposes. In addition, the simulation time and the instability of the twisted nematic solvent system are undesirable factors when considering the method for uses in sifting through large databases in search of molecules with high predicted values of β_M.

This method is also unsuitable for the study of relatively flexible chiral dopant molecules where a number of molecular conformations are likely to influence the overall HTP observed experimentally. The simulation time would become prohibitively long as accurate conformational sampling of the solute molecule would need to occur at each intermediate point in the simulation (>2 million MC steps for each λ-step). It would also be interesting to investigate the effects specific solvents and the temperature have on the HTP. When the nature of the nematic solvents used for HTP measurements are chemically different, particularly with reference to differences in their electrostatic interactions, researchers have been able to detect solvent-induced

differences in HTP values. It is even, in extreme cases, possible to obtain different signs for β_M.[26,152] In these cases solvent/solute interactions clearly have an influence on HTPs. A likely scenario here is that particular conformations are chosen preferentially in different solvents and that different conformations can have different β_M values. Investigation of these effects would not be possible using the current method due to the enormous computational cost involved in such a task. For all of these reasons, alternative methods of calculating β_M for chiral molecules have been investigated in chapters 5-7.

Chapter 5

Predictions of Molecular Chirality and Helical Twisting Powers Using Chiral Measures: Rigid Molecules

5.1 Introduction

Chapter 1 introduces the concept of chirality and the helical twisting power (HTP) and in chapter 4, computer simulations are employed that can calculate a predicted HTP from the chemical potential difference between enantiomers. However, these simulations are time consuming (calculations take several days for each enantiomer), have large errors, and require excellent statistics to provide a reasonable prediction of the HTP. In this chapter the scaled chiral index of Neal and co-workers[34–36] and the chirality order parameter approach of Nordio *et al.*[27–30,153–156] are applied to chiral molecules. These are single molecule techniques that, for a given molecular conformation, can provide a rapid calculation of chirality/HTP. Due to their computational cheapness, these methods are of great interest as they could be used to rapidly screen large numbers of chiral molecules for high HTP values prior to synthesis. Previous work by Nordio, Ferrarini and co-workers[27–30,153–156] has shown that the chirality order parameter is able to make reasonable predictions of the helical twisting power for a number of relatively rigid chiral molecules, but the scaled chiral index has not previously been applied to predictions of HTPs.

The chapter is arranged as follows: in section 5.2 the surface chirality model and the chirality order parameter are presented, and in section 5.3 the scaled chiral index is introduced. Computational details for the calculation of the two chiral measures for different molecules are given in section 5.4. The results for the application of the chiral measures to various molecules are presented and discussed in section 5.5. Finally, in section 5.6 conclusions are drawn.

5.2 Surface Chirality Model and the Chirality Order Parameter

In the surface chirality model developed by Nordio, Ferrarini and co-workers[27–30,153–156] the helical twisting power, β_M, at a temperature T, is obtained from

$$\beta_M = \frac{RT\varepsilon\chi}{2\pi K_{22}\nu_m}, \tag{5.1}$$

where ε, ν_m and K_{22} are respectively, the strength of the orienting potential, the molar volume of the nematic solution and the twist elastic constant of the solvent. The quantity χ is defined as the chirality order parameter and describes the coupling between the chiral surface of the molecule and its orientational ordering. Positive values of χ lead to a right handed twisted nematic being induced in the liquid crystal host. The theory is based upon the assumption that the alignment of a solute molecule in a locally nematic environment can be determined purely from the molecular shape of the solute, and that the chiral shape of a molecule is able to exert a torque on the local nematic director over distances many times its molecular length due to the elastic properties of the nematic phase.

χ can be obtained for any molecule from a calculation of 3 tensors, the surface tensor, **T**, the helicity tensor, **Q**, and the ordering matrix, **S**. Given a molecular surface made up from a number of points (surface elements), numerical integration over surface points yields the surface tensor

$$T_{ij} = \frac{-3\int_S s_i s_j dS + S\delta_{ij}}{\sqrt{6}}, \tag{5.2}$$

where δ_{ij} is the Kronecker delta, **s** is a unit vector along the outer normal of the molecular surface element dS and S is the total surface area. Diagonalization of **T** yields the components (T_{xx}, T_{yy}, T_{zz}) that define the tendency of the molecular principal axes to align parallel (T_{zz}) and perpendicular (T_{xx}, T_{yy}) to the nematic director. Numerical integration over the molecular surface also yields the helicity tensor

$$Q_{ij} = -\left(\frac{3}{8}\right)^{\frac{1}{2}} \sum_{k,l} \int_S \left[r_k s_l \left(\varepsilon_{ikl} s_j + \varepsilon_{jkl} s_i\right)\right] dS, \tag{5.3}$$

where ε_{ijk} is the Levi-Civita symbol and **r** is a vector from the origin of the molecular axis to a surface element dS. The helicity centre, r^H, can be calculated from **Q** (see reference[30]), and the helicity tensor recalculated using r^H as the origin in equation 5.3. Finally, **Q** can be calculated in the principal axis system of the **T** tensor and the diagonal components (Q_{xx}, Q_{yy}, Q_{zz}) are used in the calculation of χ.

The orientational behaviour of the solute molecule within the liquid crystal phase can be calculated by defining an orienting potential

$$\frac{U(\Omega)}{k_B T} = \varepsilon \int_S P_2(\mathbf{n}.\mathbf{s}) dS, \tag{5.4}$$

where $U(\Omega)$ is the orienting potential at the molecular orientation Ω, P_2 is the second Legendre polynomial and **n** is the nematic director (taken along the Z-axis). Equation 5.4 is analogous to the surface anchoring potential which has been used to determine the orientations of liquid crystal molecules in bulk nematics.[157–160] The Cartesian components of the ordering matrix **S** can be obtained by calculating

$$S_{ij} = \int \frac{(3 l_{Zi} l_{Zj} - \delta_{ij})}{2} P(\Omega) d\Omega, \tag{5.5}$$

where l_{Zi} is the cosine of the angle between the Z laboratory axis and the i molecular axis and $P(\Omega)$ is the orientational distribution function defined by

$$P(\Omega) = \frac{\exp\left[-U(\Omega)/k_B T\right]}{\int \exp\left[-U(\Omega)/k_B T\right] d\Omega}. \tag{5.6}$$

Finally, the chirality order parameter can be obtained as

$$\chi = -\left(\frac{2}{3}\right)^{\frac{1}{2}} \left(Q_{xx}S_{xx} + Q_{yy}S_{yy} + Q_{zz}S_{zz}\right), \tag{5.7}$$

where the components S_{ii} are obtained by expressing $\mathbf{S}$ in the principal axis system of the surface tensor $\mathbf{T}$.

5.3 Scaled Chiral Index

The scaled chiral index is based on a mathematical description of molecular chirality proposed by Osipov *et al.*[33] In this formulation they define an isotropic chirality index, G_0, where:

$$G_0 = \frac{1}{3}\int d\mathbf{r}_1 d\mathbf{r}_2 d\mathbf{r}_3 d\mathbf{r}_4 \rho(\mathbf{r}_1)\rho(\mathbf{r}_2)\rho(\mathbf{r}_3)\rho(\mathbf{r}_4) \times \frac{\left[(\mathbf{r}_{12}\times\mathbf{r}_{34}).\mathbf{r}_{14}\right](\mathbf{r}_{12}.\mathbf{r}_{23})(\mathbf{r}_{23}.\mathbf{r}_{34})}{(r_{12}r_{23}r_{34})^n r_{14}^m},$$

and $\mathbf{r}_i$ ranges over the volume occupied by the molecule, ρ can be a quantity associated with the molecule, $\mathbf{r}_{ij} = \mathbf{r}_i - \mathbf{r}_j$, $\widehat{\mathbf{r}}_{ij} = \frac{\mathbf{r}_{ij}}{r_{ij}}$ and n and m are arbitrary integers. Neal *et al.* extended this formulation for general molecular structures by calculating a scaled chiral index,[34] defined as:

$$G_{0S} = \frac{1}{3}\frac{4!}{N^4} G_0,$$

that converges towards a fixed value with increasing number of points, N. The discrete form of the isotropic scaled chiral index is given by:

$$G_{0S} = \frac{1}{3}\frac{4!}{N^4}\left[\sum_{i,j,k,l=1}^{N} \omega_i\omega_j\omega_k\omega_l \frac{\left[(\mathbf{r}_{ij}\times\mathbf{r}_{kl}).\mathbf{r}_{il}\right](\mathbf{r}_{ij}.\mathbf{r}_{jk})(\mathbf{r}_{jk}.\mathbf{r}_{kl})}{(r_{ij}r_{jk}r_{kl})^n r_{il}^m}\right] \tag{5.8}$$

where the sum includes the contribution of all permutations of four points (atoms), $\mathbf{r}_i$ is the position of atom i, $\mathbf{r}_{ij} = \mathbf{r}_i - \mathbf{r}_j$, N is the number of atoms, and the weighting factors $\omega_{i,j,k,l}$ can be a physical quantity associated with the point/atom. The case where $n = 2$ and $m = 1$ is considered, corresponding to a dimensionless index, and the weighting factors are set to $\omega_{i,j,k,l} = 1$, although alternatively they could be set

to any representative physical quantity to give extra weight to certain points. G_{0S} is invariant under rotation and translation, changes sign on reflection and is zero for achiral objects.

5.4 Computational

For each of the chiral molecules studied in this chapter, the *CAChe* molecular modelling package[161] is used to calculate the energy minimised structure in the MM3 force-field.[76] Given an energy minimised structure, the chirality order parameter and the scaled chiral index are then calculated using the methods described in sections 5.4.1 and 5.4.2 respectively. The results and comparisons with experimental helical twisting powers for a variety of chiral molecules are presented in section 5.5.

5.4.1 Calculation of the chirality order parameter

The calculation of the chirality order parameter is a multi-step process that requires the calculation of several tensors, namely the surface and helicity tensors and the ordering matrix. The practical considerations required in the determination of each of these quantities are detailed below and the FORTRAN90 code used to calculate the chirality order parameter is included in appendix A (section A.2.1).

Calculation of the surface tensor

The surface tensor, **T**, is defined in equation 5.2 and represents the anisometry of the molecular surface. In order to calculate **T** it is necessary to represent the molecular surface by a number of discrete points on the surface, each point represented by a vector, **r**, from the origin of the molecular axes and a corresponding unit vector along the outer normal of the molecular surface, **s**. To determine the molecular surface, with corresponding vector normals to the surface, from an input co-ordinate file, the Simple Invariant Molecular Surface (SIMS) routine of Vorobjev and Hermans[162] is used that has been shown to produce good representations of molecular surfaces. The SIMS routine also calculates the area on the surface that each dot represents, dS. Given these values the calculation of the 3x3 **T** matrix from equation 5.2 is

simple. Diagonalization of the $\mathbf{T}$ matrix yields the values T_{xx}, T_{yy} and T_{zz} along with three corresponding eigenvectors which are grouped in a 3x3 eigenvector matrix which are denoted $\mathbf{T}_{evec}$. These are now defined as the molecular principal axes. The choice of which value corresponds to the x, y or z molecular axis is arbitrary for the calculation of the chirality order parameter. However, as a standard, the largest positive diagonalized element represents the molecular axis with the most tendency to align along the nematic director and is denoted as T_{zz}.

Calculation of the helicity tensor

The helicity tensor, $\mathbf{Q}$, defined in equation 5.3, is dependent on the origin used to define the position of each point on the molecular surface, $\mathbf{r}$. For comparison between many different molecules it is therefore vital to have a standard origin defined in all cases. The origin that is used is known as the helicity centre, H. In order to define the helicity centre it is necessary to define the helicity tensor as:

$$\mathbf{Q} = \sqrt{\frac{3}{8}}\,(\mathbf{q} + \widetilde{\mathbf{q}})\,, \tag{5.9}$$

where

$$\mathbf{q} = -\int_S \mathbf{r} \times \mathbf{s} \otimes \mathbf{s}\, dS, \tag{5.10}$$

and

$$\widetilde{\mathbf{q}} = \int_S \mathbf{s} \otimes \mathbf{s} \times \mathbf{r}\, dS. \tag{5.11}$$

Now the tensor $\mathbf{q}$ can be decomposed into symmetric ($\mathbf{q}_s$) and antisymmetric ($\mathbf{q}_a$) parts:

$$\mathbf{q}_s = (\mathbf{q} + \widetilde{\mathbf{q}})/2, \tag{5.12}$$

$$\mathbf{q}_a = (\mathbf{q} - \widetilde{\mathbf{q}})/2, \tag{5.13}$$

and it can be shown that in every molecule there is a unique point that, if used as the origin to define $\mathbf{r}$, the antisymmetric parts, $\mathbf{q}_a$, completely vanish. This point is termed the helicity centre, H. To determine H, $\mathbf{q}_a$ is calculated using any origin, O, in the molecular frame. This is referred to as $\mathbf{q}_a^O$. Now, the transformation law for

translation of the origin from point O to point O' must also be noted and is given by:

$$2\mathbf{q}_a^O = 2\mathbf{q}_a^{O'} + \left[(\mathbf{r}^{OO'} \times \mathbf{t}) + (\mathbf{t} \times \mathbf{r}^{OO'})\right],$$

where

$$\mathbf{t} = -\int_S \mathbf{s} \otimes \mathbf{s}\, dS, \tag{5.14}$$

and $\mathbf{r}^{OO'}$ is the vector from point O to point O'. As $\mathbf{q}_a^H$ is zero for all components, by definition, then three equations with three unknowns can be set up and solved to find $\mathbf{r}^{OH}$. These equations are:

$$2(\mathbf{q} - \widetilde{\mathbf{q}})_{xy} = (r_y^{OH} t_{zy} - r_z^{OH} t_{yy}) + (t_{xz} r_x^{OH} - t_{xx} r_z^{OH}), \tag{5.15}$$

$$2(\mathbf{q} - \widetilde{\mathbf{q}})_{xz} = (r_y^{OH} t_{zz} - r_z^{OH} t_{yz}) + (t_{xx} r_y^{OH} - t_{xy} r_x^{OH}), \tag{5.16}$$

$$2(\mathbf{q} - \widetilde{\mathbf{q}})_{yz} = (r_z^{OH} t_{xz} - r_x^{OH} t_{zz}) + (t_{yx} r_y^{OH} - t_{yy} r_x^{OH}). \tag{5.17}$$

These equations were solved to find r_x^{OH}, r_y^{OH} and r_z^{OH} using the *Maple* mathematical computer package[163] and the solutions can be found in appendix A (section A.1). Having found $\mathbf{r}^{OH}$, and thus H, the origin can be set at the helicity centre and the helicity tensor, $\mathbf{Q}$, can be calculated. The helicity tensor in the principal frame of the surface tensor, $\mathbf{Q}_{prin}$, is found from:

$$\mathbf{Q}_{prin} = (\mathbf{T}_{evec})^{-1} \mathbf{Q} (\mathbf{T}_{evec}) \tag{5.18}$$

and the diagonal components of $\mathbf{Q}_{prin}$ yield Q_{xx}, Q_{yy} and Q_{zz} required for the calculation of the chirality order parameter.

Calculation of the ordering matrix

The calculation of the ordering matrix, $\mathbf{S}$, is done using the formula in equation 5.5. This requires an evaluation of the orienting potential, $U(\Omega)$, at various molecular orientations, Ω. Following reference,[30] in a twisted nematic phase with a helical pitch P, and wavevector $q = 2\pi/P$ in a laboratory reference frame (X, Y, Z), where the Y and Z axes are defined as parallel to the helical axis and the nematic

director respectively, the orienting potential in equation 5.4 becomes:

$$\frac{U(\Omega)}{k_B T} = -\varepsilon \left(\frac{3}{2}\right)^{\frac{1}{2}} \sum_{i,j} l_{Zi}(T_{ij} - qQ_{ij}) l_{Zj}, \tag{5.19}$$

where l_{Zi} is the cosine of the angle between the Z laboratory axis and the i molecular axis. For each molecular orientation equation 5.19 is used to calculate the orienting potential, setting the wavevector $q = 0$ for the limit of the pitch of the cholesteric phase being much larger than the dimensions of the molecule studied, and using T_{ij} already calculated from equation 5.2. To evaluate $P(\Omega)$ (equation 5.6), and hence $\mathbf{S}$, a double integration over the β and γ Euler angles is performed using 1000 points for each angle.[164] Calculation of $l_{Zi,j}$ is simple given a specific molecular orientation. Finding the ordering matrix in the principal axis system of the surface tensor, $\mathbf{S}_{prin}$, is found as in equation 5.18:

$$\mathbf{S}_{prin} = (\mathbf{T}_{evec})^{-1} \mathbf{S} (\mathbf{T}_{evec}), \tag{5.20}$$

and its diagonal components are S_{xx}, S_{yy} and S_{zz}.

Determination of χ

The chirality order parameter, χ, is calculated from equation 5.7 as Q_{xx}, Q_{yy} and Q_{zz} have been determined from equation 5.18 and S_{xx}, S_{yy} and S_{zz} from equation 5.20. It is noted that χ is positive for a right handed chiral molecule and negative for a left handed chiral molecule and its value is directly proportional to the magnitude of the HTP, β_M.

Parameterisation of model

The value of the chirality order parameter, for a given molecular conformation, is dependent on the molecular surface. In the SIMS routine,[162] the molecular surface is generated by a rolling sphere algorithm. Here, a *solvent probe* sphere with a radius r_{probe} is rolled over the van der Waals sphere representation of the molecule and the *probe* sphere maps out the solvent-excluded volume of the molecule. There are

two parameters that can be used to vary the molecular surface generated for a fixed molecular conformation, namely the number of points used to represent the surface and the value of r_{probe}.

Values of χ were calculated at a number of surface point densities from 1 to 12 $Å^{-2}$ for a number of molecules. Convergence of χ was found to occur for all molecules at surface point densities between 6 and 8 $Å^{-2}$. In order to ensure an accurate molecular surface is generated for all molecules, a surface point density of 10 $Å^{-2}$ (typically >2000 surface points per molecule) is employed in all the calculations carried out in this chapter.

The rolling *probe* sphere maps out a solvent accessible molecular surface. Therefore, a value of r_{probe} should be chosen that represents realistic nematic solvent molecules. Ferrarini *et al.* have studied the effect of changing r_{probe} on χ.[165] They comment that a value of $2.5 \leq r_{probe} \geq 5.0$ Å should be used to represent the rolling sphere. They justify this value by considering the typical size of substituents in nematic solvents, such as the methyl group, and also because the value of the ordering matrix, **S**, has only a weak dependence on r_{probe} in this range. The latter point is important as the order parameter (closely related to **S**) for nematic solvents should not be dependent on the value of r_{probe} used. For the calculations in this chapter, a value of $r_{probe} = 2.5$ Å is used.

5.4.2 Calculation of the scaled chiral index

Compared with the determination of the chirality order parameter, the scaled chiral index is relatively simple to calculate. Given an energy minimised molecular structure, where the exact positions of the atoms are known, G_{0S} is calculated from equation 5.8. It is noted that G_{0S} is negative for right-handed molecules. Therefore, values of $-G_{0S}$ are quoted throughout this chapter. The FORTRAN90 code used to calculate the scaled chiral index is included in appendix A (section A.2.2).

5.5 Results and Discussion

To provide a quantitative comparison between the two chiral measures, and to examine their applicability to the prediction of helical twisting powers for liquid crystalline chiral dopants, a number of chiral molecules are studied. In section 5.5.1 the two chiral measures are applied to the chiral molecules previously studied in chapter 4. A more extensive study of a series of rigid molecules: bridged biaryl[166] and helicene derivatives[154,167] is undertaken in section 5.5.2. These are molecules where one particular molecular conformation dominates and their experimental helical twisting powers show little temperature dependence. For these reasons, they are an excellent choice to test the theoretical methods used here and will provide a good comparison with experimental results. In section 5.5.3 a theoretical study of the dependence of the chiral measures on the inter-ring angle in the 1,1' binaphthyl molecule is carried out and in section 5.5.4 the conformational dependence of the chiral measures is further examined for the case of a TADDOL ($\alpha, \alpha, \alpha', \alpha'$-tetraaryl-1,3-dioxolan-4,5-dimethanol) derivative.

5.5.1 Chiral dopants A-E

The first set of molecules that the chirality order parameter and the scaled chiral index are applied to are the chiral molecules studied in the chemical potential difference calculations of chapter 4, whose structures are given in figure 4.2. The results are shown below in table 5.1 and are encouraging. The correct sign of twist is predicted in all five molecules for both methods. From a small sample size of only five molecules it is difficult to assess how well each method predicts the magnitude of the HTP. For this reason, this question is addressed later using a larger sample size in section 5.5.2.

Of interest in the results is the large difference in S_{zz} for molecule B compared to the others, indicating that there is much better ordering of this molecule along the nematic director. Also of note are the large helicity values for molecule A. With greater ordering of molecule A in a nematic solvent, the chirality order parameter would be even larger in magnitude.

Molecule	Q_{xx}/Å^3	Q_{yy}/ Å^3	Q_{zz}/ Å^3	S_{xx}	S_{yy}	S_{zz}	χ / Å^3	$-G_{0S} \times 10^4$	β_M/ μm^{-1}
A	-142	185	-43	0.06	-0.34	0.28	+69.0	+60.4	+104
B	-1	25	-24	-0.23	-0.38	0.61	+19.3	+84.4	+58
C	-58	57	1	0.13	-0.35	0.23	+22.3	+29.6	+24
D	67	-26	-40	0.09	-0.28	0.19	-5.2	-56.4	-21
E	-89	69	20	-0.04	-0.40	0.44	+12.4	+1.3	+8

Table 5.1: Diagonal components of the helicity tensor **Q**, and the ordering matrix **S**, chirality order parameter χ, scaled chiral index G_{0S}, and the experimental helical twisting powers β_M for chiral dopants A-E whose structures are shown in figure 4.2.

Molecule A has a certain degree of flexibility and is studied further in section 5.5.4 to examine the conformational dependence of the two methods.

5.5.2 Bridged biaryl and helicene derivatives

In this section the results from a study of a series of rigid bridged biaryl and relatively rigid helicene derivatives are presented. Bridged biaryl derivatives have been studied experimentally by Gottarelli *et al.*[166] and are of specific theoretical interest as their molecular structures are effectively locked by the ringed structures formed by the 2,2' substituents. It should be noted that open derivatives, where the 2,2' substituents are not bonded together, have also been studied experimentally and have been found to have much lower HTPs than the bridged derivatives.[168] This effect is discussed further in section 5.5.3. Helicene derivatives[154,167] are also relatively rigid structures that have a helical shape caused by the steric repulsion between overlapping substituents at either end of the molecule, and so they are also useful for a theoretical comparison of the two methods with experimental results. The bridged biaryl and helicene derivatives studied are shown in figure 5.1 and the results are presented in table 5.2.

To calculate predicted values of β_M in figure 5.2 a scaling factor is used. For the surface chirality model T, ε and K_{22} are taken to be unchanged for all dopants and at low dopant concentrations ν_m tends towards the molar volume of the solvent, so

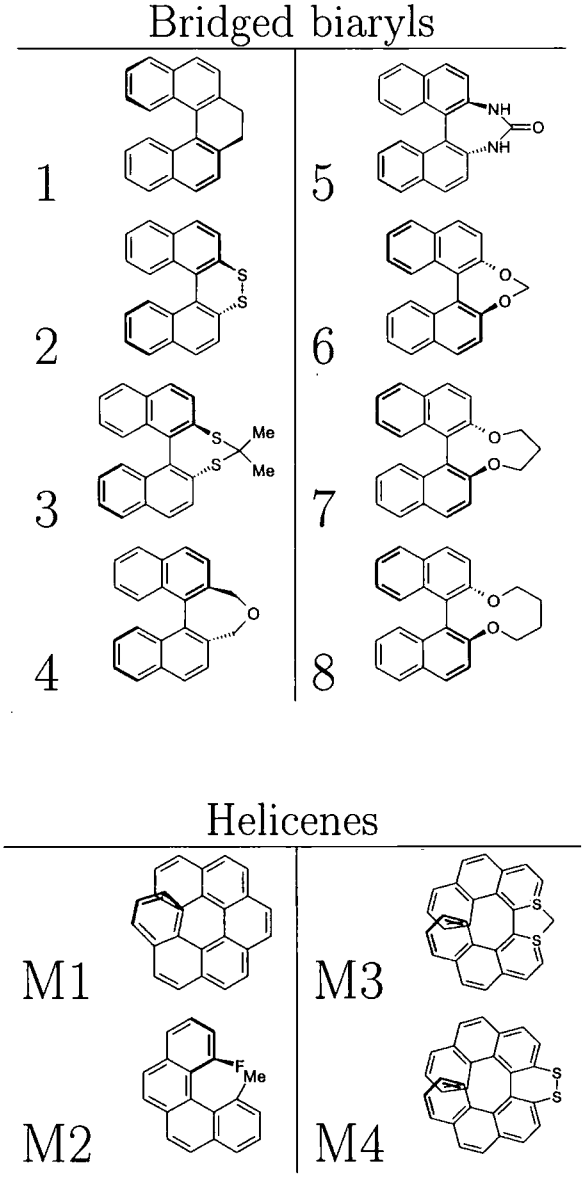

Figure 5.1: Structures of the bridged biaryl (1-8) and helicene derivatives (M1-M4) studied.

Molecule	Q_{xx}/Å^3	Q_{yy}/ Å^3	Q_{zz}/ Å^3	S_{xx}	S_{yy}	S_{zz}	χ / Å^3	$-G_{0S} \times 10^4$	β_M/ μm^{-1}
1	-103	79	24	0.05	-0.37	0.31	+21.9	+74.7	+69
2	90	-67	-23	0.06	-0.38	0.31	-19.2	-109.4	-65
3	24	-85	62	0.03	-0.33	0.31	-39.1	-144.6	-71
4	125	-101	25	-0.02	-0.32	0.35	-17.1	-65.9	-55
5	92	-63	-29	0.12	-0.38	0.26	-22.4	-100.6	-21
6	-116	92	25	0.02	-0.35	0.33	+21.6	+97.8	+85
7	-137	93	45	0.06	-0.31	0.26	+21.0	+118.3	+80
8	-124	67	57	0.14	-0.33	0.19	+23.4	+148.8	+79
M1	69	-68	-1	0.04	-0.39	0.36	-23.6 (-36)	-106.6	-55
M2	61	-44	-17	-0.04	-0.37	0.40	-5.8 (-12)	-17.8	-9
M3	37	-55	18	0.05	-0.39	0.34	-23.8 (-43)	-86.4	-20
M4	41	-50	9	-0.01	-0.39	0.40	-18.2 (-25)	-31.0	-13

Table 5.2: Diagonal components of the helicity tensor **Q**, and the ordering matrix **S**, chirality order parameter χ, scaled chiral index G_{0S}, and the experimental helical twisting powers β_M, taken from Ref.[166,167] for the bridged biaryl and helicene molecules in figure 5.1. Values of χ from Ref.[154] using a probe radius of 0 Å are included in brackets for comparison for molecules M1 to M4.

from equation 5.1 a predicted β_M is determined as:

$$\beta_M = D\chi \tag{5.21}$$

where

$$D = \frac{RT\varepsilon}{2\pi K_{22}\nu_m}. \tag{5.22}$$

Here a value of $D = 2.351$ Å$^{-3}\,\mu m^{-1}$ is found from a best fit to experimental data.[166,167] A predicted β_M for G_{0S} is also predicted as:

$$\beta_M = -JG_{0S} \tag{5.23}$$

where J is a constant found from a best fit to experimental data. Here a value of $J = 0.523\,\mu m^{-1}$ is used.

The results in figure 5.2 show good agreement with experimental findings. As reported recently,[169] a similar level of agreement between the G_{0S} and χ methods is found. The sign of β_M is correctly predicted in each case for each method, and the

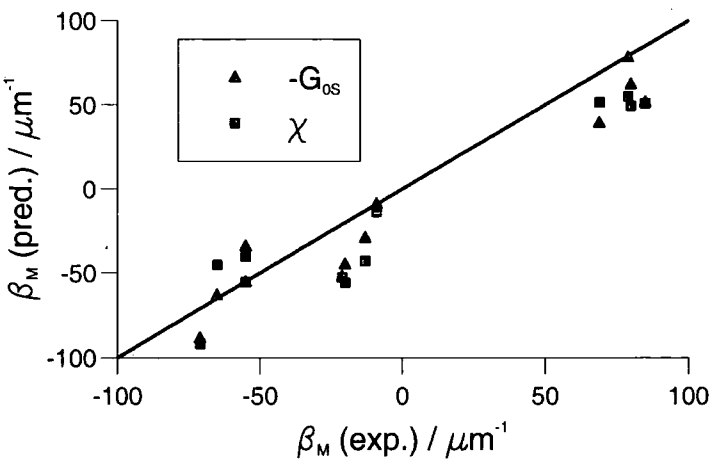

Figure 5.2: The predicted HTP for the bridged biaryl and helicene derivative molecules in figure 5.1 using the chirality order parameter (squares), χ (as defined in equation 5.7), and the scaled chiral index (triangles), -G_{0S} (as defined in equation 5.8), compared to the experimental HTP.

magnitude of β_M is predicted with an average error of $\pm 17\ \mu m^{-1}$ using the scaled chiral index and $\pm 22\ \mu m^{-1}$ using the chirality order parameter. Ferrarini *et al.*[154] have also studied helicene molecules M1→M4. The results presented here differ slightly from those in the previous work due to the size of the probe radius used to generate the molecular surface. It should be noted that when the molecules are considered as an assembly of van der Waals spheres (probe radius of 0 Å) the results obtained are almost identical to those in the Ferraini *et al.* study.

A feature of the scaled chiral index is that the contribution that each point (atom in this case) makes to the final value of $-G_{0S}$ can be monitored. Figure 5.3 demonstrates this for the case of molecule 1 where the shade of the atom represents its contribution to $-G_{0S}$ (shading from blue (low contribution) to red (large positive contribution). In this case the atoms furthest away from the centre of the molecule in the naphthyl rings have the largest contribution to the scaled chiral index.

Figure 5.3: Individual atom contributions to $-G_{0S}$ for bridged biaryl molecule 1 in figure 5.1 (red shade denotes a high contribution and blue shade a low contribution).

5.5.3 The 1,1'-binaphthyl molecule

A theoretical study of the 1,1'-binaphthyl molecule, which is shown in figure 5.4, was undertaken to examine the influence of the torsional angle, ϑ, on the value of the chirality order parameter, χ, and the scaled chiral index, $-G_{0S}$.

The results from the study can be seen in figure 5.5. There are significant differences between the two approaches, most obviously in the sign of $-G_{0S}$ between 0 and 40 degrees and 90 to 180 degrees. It is clear that the scaled chiral index method adopted here using the positions of atoms in the molecule as a basis for describing chirality does not agree with the method used by Ferrarini *et al.*, which uses a molecular surface tensor. Neal *et al.*[169] have recently commented that the scaled chiral index is sensitive to different aspects of chirality than the chirality order parameter. However, it is interesting that the two methods agree in the handedness of chirality in all cases for the bridged biaryl derivatives studied in section 5.5.2. It should be noted that the structures studied for the 1,1'-binaphthyl molecule at ϑ angles close to 0 degrees are physically unrealistic due to the steric repulsion caused by overlapping hydrogen atoms, and it is at small ϑ angles that the handedness of the two methods disagree (ϑ angles for the bridged biaryl derivatives are typically in

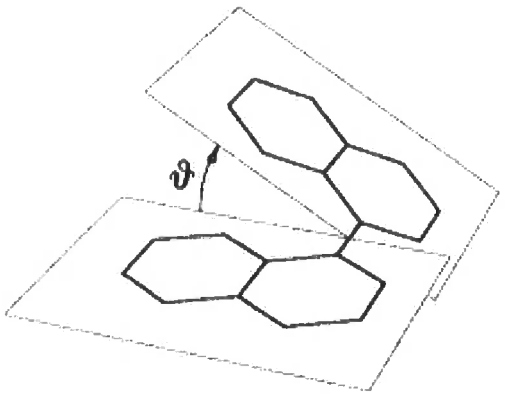

Figure 5.4: The torsional angle ϑ (shown towards positive) in the 1,1'-binaphthyl molecule.

the range $35^o < \vartheta > 65^o$ and none are in the range $\vartheta > 90^o$ where the two methods also disagree on the sign of chirality).

It should be noted that the HTPs of binaphthol derivatives where the 2,2' substituents are not bridged is much lower than for the bridged biaryl derivatives studied in section 5.5.2. As the inter-ring angle is not fixed in the unbridged structure then a large number of different conformations are likely to be sampled and contribute to an overall HTP. In a simple approach, if all conformations between 0^o and 180^o are sampled with the same probability then the overall average chirality/HTP is expected to be very small for the chirality order parameter. The magnitude of chirality/HTP is expected to be slightly larger for the scaled chiral index, but still not as large as for a structure where the inter-ring angle is locked between $35^o < \vartheta > 65^o$.

5.5.4 Conformational dependence of chirality in a TADDOL molecule

To examine further the effect of conformational change on chirality and the helical twisting power, molecule A from chapter 4 and section 5.5.1 is studied more extensively here. Molecule A has considerable structural flexibility around eight internal dihedral angles (see figure 5.6), and consequently has an extremely complex confor-

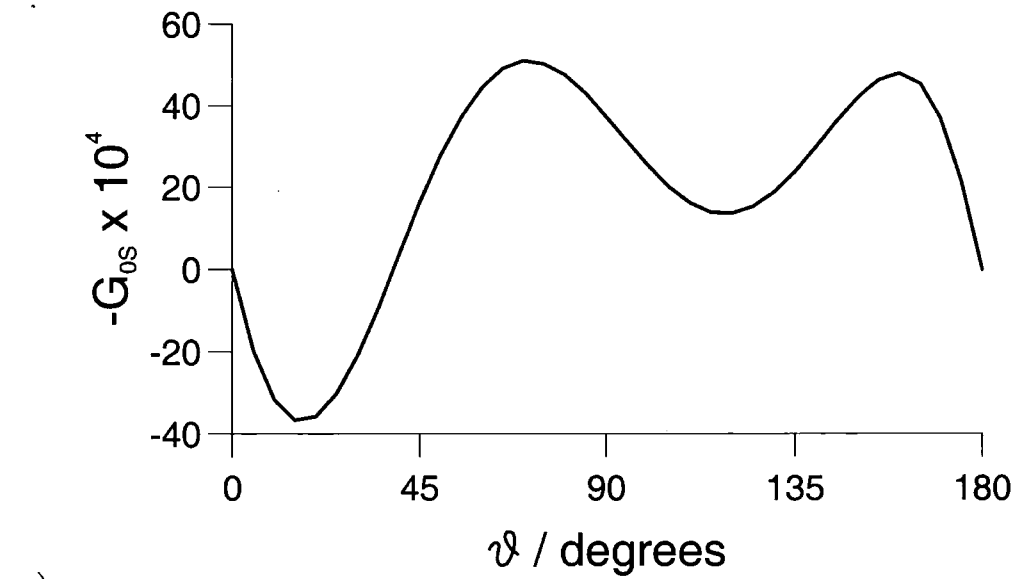

a)

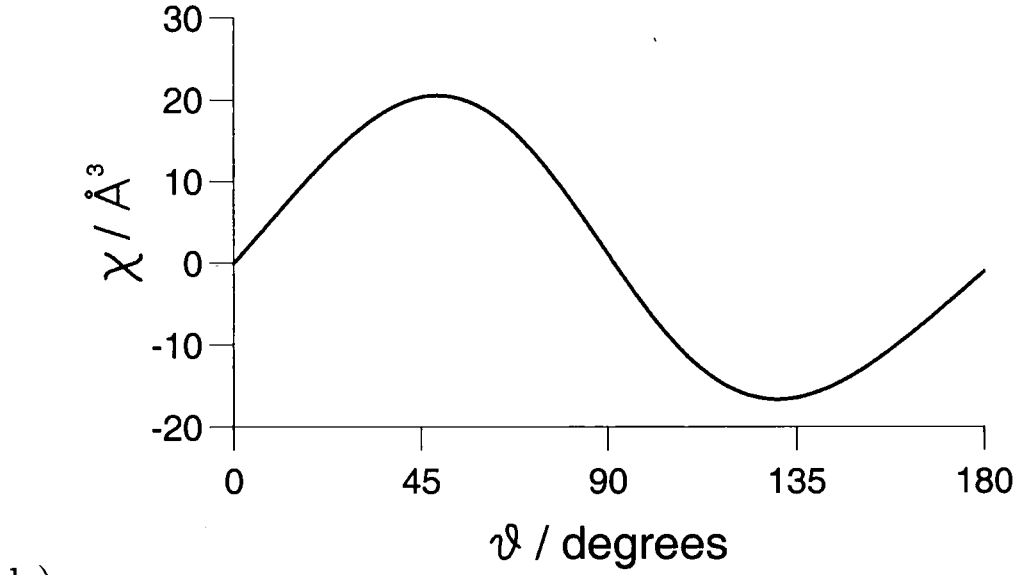

b)

Figure 5.5: a) Scaled chiral index, $-G_{0S}$, as a function of the torsional angle, ϑ, b) chirality order parameter, χ, as function of the torsional angle, ϑ, for the 1,1'-binaphthyl molecule.

mational potential energy surface with many local minima. In this study, twenty

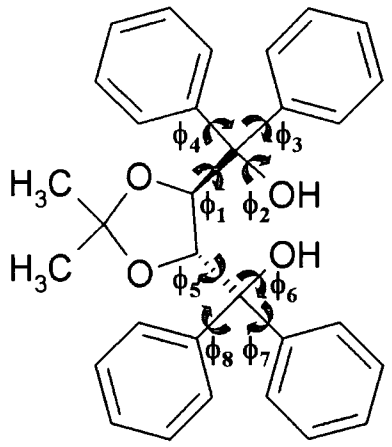

Figure 5.6: Structure of molecule A. Diagram shows the eight dihedral angles, ϕ_{1-8}, which give the molecule its structural flexibility.

conformations that are very close in energy (within 1 kcal mol^{-1}) in the MM3 force-field are considered. In each conformation, intra-molecular hydrogen bonding occurs (ϕ_1 and ϕ_5 are both approximately 180^o), and the main differences between the conformations is due to torsional angles $\phi_{3-4,7-8}$ (ϕ_2 and ϕ_6 determine the positions of the hydrogens in the OH groups, but these do not significantly affect the calculated values of chirality). Table 5.3 shows results of calculations of the two chiral measures, as well as the energy of the conformation in the MM3 force-field and the values of torsional angles $\phi_{3,4,7,8}$.

The results show a very good correlation between the sign and the magnitude of the two chiral measures for each different conformation. There is also a direct correlation between dihedral angles $\phi_{3,4,7,8}$ and the chirality of the conformation. High values of χ and $-G_{0S}$ are calculated for all conformations where both ϕ_4 and ϕ_8 are approximately 0^o or 180^o (noting that due to the symmetry of phenyl rings, torsional angles of 0^o and 180^o are equivalent for $\phi_{3,4,7,8}$) and low chirality is found for all other conformations. Molecule A has an experimental $\beta_M = 104\,\mu m^{-1}$ and so it is possible that high chirality conformations with $\phi_{4,8} \approx 0^o, 180^o$ are preferentially selected in a nematic liquid crystalline solvent.

Conformation	χ/Å^3	$-G_{0S} \times 10^4$	E/kcal mol^{-1}	ϕ_3/deg.	ϕ_4/deg.	ϕ_7/deg.	ϕ_8/deg.
A1	-1.1	+0.2	58.47	324	248	113	358
A2	-5.3	-2.1	58.52	324	246	115	178
A3	-10.7	-1.2	59.36	323	245	112	177
A4	+68.4	+60.1	59.45	281	1	102	346
A5	+52.6	+62.3	59.36	283	0	102	349
A6	+33.8	+59.4	58.92	288	12	102	350
A7	+90.2	+52.2	58.86	286	338	108	343
A8	+3.1	+1.8	58.51	321	258	106	353
A9	-6.2	-2.6	58.42	321	244	120	178
A10	-4.4	-3.9	58.40	323	244	120	179
A11	+3.0	-0.2	58.39	323	266	100	166
A12	-5.5	-1.7	58.48	322	246	116	354
A13	-9.0	-2.7	58.43	323	244	116	177
A14	-1.0	-3.3	58.78	323	246	119	179
A15	-7.3	-2.6	58.40	323	244	115	178
A16	+68.0	+60.4	59.52	283	0	100	347
A17	+65.1	+62.4	59.40	284	0	97	349
A18	-4.7	+1.4	58.58	320	75	103	176
A19	+72.5	+60.6	59.50	280	355	104	349
A20	-8.2	-3.7	58.48	323	244	120	178

Table 5.3: Chirality order parameter, χ, scaled chiral index, $-G_{0S}$, energy in the MM3 force-field of the conformation, and values of the torsional angles ϕ_4 and ϕ_8 for twenty different conformations of the TADDOL molecule in figure 5.6.

This example clearly illustrates the problem of calculating the chirality of a flexible molecule. Conformations that have very similar potential energies can have completely different values of chirality (and hence predicted values of the HTP). For flexible molecules, the macroscopic experimentally measured helical twisting power will be a statistical mechanical average of helical twisting powers resulting from thousands of different conformations sampled by the flexible chiral dopant in the liquid crystalline nematic solvent. This last point is justified by experimental results of doping nematic materials with mixtures of two or more chiral compounds with known HTPs[170] where the HTP is given by:

$$\beta_M = \sum_i x_i \beta_{Mi}, \tag{5.24}$$

where x_i and β_{Mi} are the mole fraction and HTP of dopant i respectively. Flexible molecules, including TADDOL derivatives, are studied in detail in the following chapter where a simulation approach is used to calculate average values of chirality from a statistically significant and independent number of conformations for a chiral molecule.

5.6 Conclusions

Calculations of the chirality order parameter, χ, and the scaled chiral index, $-G_{0S}$, have been performed for a range of relatively rigid chiral molecules. The results from this chapter have demonstrated that, for the molecules studied, χ and $-G_{0S}$ show good agreement with both the sign and magnitude of experimental helical twisting powers for chiral dopant molecules. Coupled with their rapid calculation time (~ 1 s for χ and ~ 10 s for $-G_{0S}$) this makes the methods extremely promising for uses in searching for molecules with high HTPs and for the study of structure-property relationships in rigid structures.

A study of a flexible chiral molecule has shown that different conformations can have vastly different associated chiralities and that many different conformations are likely to contribute to an overall experimentally measured HTP. In order to make

an accurate prediction of the HTP in flexible molecules, all of these conformations must be taken into account.

Chapter 6

Predictions of Molecular Chirality and Helical Twisting Powers Using Chiral Measures: Monte Carlo Simulations of Flexible Molecules

6.1 Introduction

In the previous chapter, the chirality order parameter, χ, of Nordio *et al.*[27–30,153–156] and the scaled chiral index of Neal and co-workers,[34–36] $-G_{0S}$, were shown to provide good predictions of the sign and magnitude of experimental helical twisting powers (HTPs) when applied to a range of chiral molecules. However, the approach described in chapter 5 is only applicable to relatively rigid structures where only one particular molecular conformation is likely to be adopted in the liquid crystalline solvent.

In order to study a range of flexible chiral molecules, the chirality order parameter (section 5.2) and scaled chiral index (section 5.3) measures, used in the previous chapter, are combined with Monte Carlo simulation studies in this chapter. In the description of the chiral measures, equations 5.1 to 5.7 and 5.21 for the surface chirality model and equations 5.8 and 5.23 for the scaled chiral index, are given for a single conformation. However, equations 5.1, 5.21 and 5.23 are equally valid

to calculate an average χ or $-G_{0S}$ from a statistically significant and independent number of conformations of a molecule.

The chapter is organised as follows: the simulation approach used is described in section 6.2. In section 6.3, results for a series of TADDOL ($\alpha, \alpha, \alpha', \alpha'$-tetraaryl-1,3-dioxolan-4,5-dimethanol) derivatives (section 6.3.1), a chiral photochromic dopant with variable HTP (section 6.3.2), a liquid crystalline material that undergoes a temperature induced twist inversion in the cholesteric phase (section 6.3.3), and a series of achiral banana molecules that have been found to act as chiral dopants when added to a cholesteric liquid crystal (section 6.3.4) are presented. In section 6.3.5 a predictive study is carried out to aid in future synthetic strategies for the design of new molecules with high HTPs. Finally in section 6.4, conclusions are drawn as to the strengths and weaknesses of the method, and possible extensions to the work are presented and discussed.

6.2 Computational

To take into account the conformational dependence of χ and $-G_{0S}$ an internal coordinate Monte Carlo (MC) technique is used, where molecules are represented by a Z-matrix. An augmented form of the MM2[75] force field is used that is taken from an initial energy minimisation using the *CAChe* program.[161] Full details of the internal co-ordinate MC program are given in reference[151] and are also discussed in section 2.4.1. Sampling of χ and $-G_{0S}$ is carried out at intervals of 200 MC steps with a new molecular surface generated for each sample. For each molecule and each temperature studied, runs in excess of $2\text{x}10^6$ MC steps are carried out. Checks for convergence of the mean steric energy, χ and $-G_{0S}$ values, and of dihedral angle distributions are carried out in each case. In most cases convergence of averages occurs within $5\text{x}10^5$ MC steps.

It should be noted that the chirality order parameter is an order of magnitude less expensive to calculate than the scaled chiral index for the systems studied and increases with the approximate square of the number of atoms, N, as opposed to N^4 for $-G_{0S}$. The former is therefore better suited for the thousands of individual

calculations required in a full Monte Carlo study of a flexible molecule. Therefore, for the large flexible molecules studied in sections 6.3.3 to 6.3.5 the work includes only calculations of χ values and not $-G_{0S}$ values due to the computational expense of calculating $-G_{0S}$.

Prior to calculations on flexible chiral molecules, a study of the achiral hexane molecule was carried out. Using the approach described above, $\langle\chi\rangle = (-0.00017 \pm 0.00619)$ Å^3 and $\langle -G_{0S}\rangle \times 10^4 = -0.316 \pm 0.178$. Essentially the molecule was found to be achiral using both methods.

6.3 Simulation, Results and Discussion

6.3.1 TADDOL Derivatives

The TADDOL family of molecules are based on the structural core shown in figure 6.1a. TADDOL derivatives have a wide variety of HTPs ranging from around $20\,\mu m^{-1}$ to an extraordinarily large $300\,\mu m^{-1}$ and are relatively soluble in polar solvents making them good candidates for use as chiral dopants.[171,172] They exhibit a high degree of flexibility around torsional angles ϕ_{1-8} (shown in figure 6.1a) giving them considerable conformational freedom. Three TADDOL derivatives are studied with widely different HTPs (figure 6.1b). The simulations are carried out at three temperatures between 300 K and 350 K for each of the molecules using the MC approach described in section 6.2.

Chirality Order Parameter Results and Discussion

Following Ferrarini *et al.*[173] the ordering strength parameter, ε, is approximated to vary as $1/k_BT$ and its value is set as $\varepsilon = 0.05$ Å^{-2} at $T = 300$ K. Results are presented in figure 6.2 with the simulation value of β_M determined as in section 5.4.2 using $D = 2.351$ Å$^{-3}\mu m^{-1}$. For comparison, results for the case where $\varepsilon = 0.05$ Å^{-2} at all temperatures are also presented. The magnitude of the HTP in figure 6.2 is predicted to a good accuracy and the trend of decreasing HTP with increasing temperature is also observed, although the effect is not as pronounced in the simulation. For TADDOLs A and B, the drop in HTP can partly be attributed

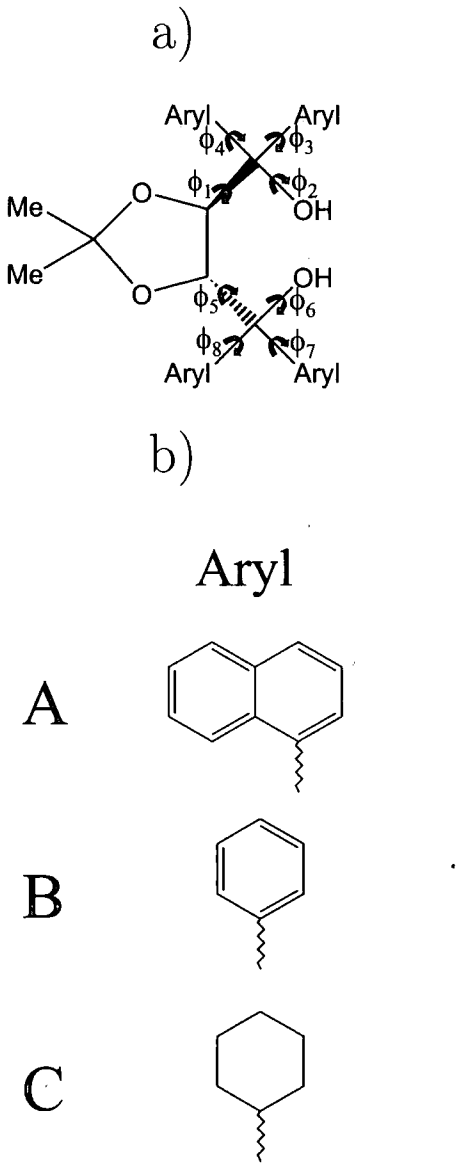

Figure 6.1: a) Basic TADDOL structure showing the flexibility around dihedral angles $\phi_1 \rightarrow \phi_8$, b) TADDOL derivatives A, B, C where the structures shown are the Aryl substituents in figure 6.1a.

to the decrease in ε with temperature, but another effect comes from conformational changes (see below).

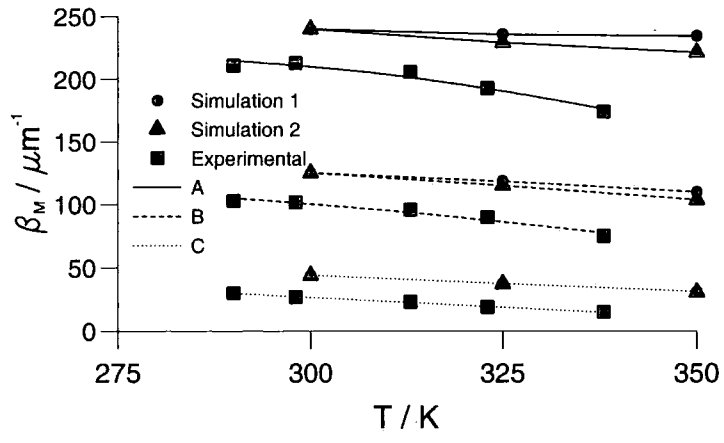

Figure 6.2: Predicted HTPs from simulation results with a constant ordering strength (1) (circles) and with an ordering strength with a $1/k_BT$ dependence (2) (triangles) as a function of temperature compared to experimental findings (squares) from Ref.[171] for TADDOL derivatives A (solid line), B (dashed line) and C (dotted line).

It is important to realise that the technique used samples molecular conformations in the gas phase, and not in the liquid crystal phase where solute-solvent interactions are likely to influence the relative weight of different conformations.[174,175] However, the model can be used to determine what conformations give rise to particularly high chirality order parameters (and hence HTPs) and also examine how a change in temperature influences the selection of these conformations. Figure 6.3a shows how the chirality order parameter varies with the dihedral angle ϕ_8 for structure B at 350 K. (Noting that the behaviour of ϕ_8 is identical to that of ϕ_4.) For ϕ_8 (and ϕ_4) the chirality order parameter varies as a cosine wave with a period of π. Conformations with high chirality are observed at $\sim 0^o$ (α conformations, $315^o \rightarrow 45^o$) and $\sim 180^o$ (γ conformations, $135^o \rightarrow 225^o$) and low chirality at $\sim 90^o$ (β conformations, $45^o \rightarrow 135^o$) and $\sim 270^o$ (δ conformations, $225^o \rightarrow 315^o$). These are consistent with the results in section 5.5.4 for molecule B (it should be noted that TADDOL molecule B is the same as molecule A from chapters 4 and 5). If

conformations α and γ are preferentially selected at lower temperatures compared to β and δ, then this would explain the temperature dependence observed in the simulation and potentially in the experimental system. Table 6.1 shows the relative populations of α, β, γ and δ conformations for structure B between 300 K and 350 K. Table 6.1 clearly shows a trend of decreasing populations of high chirality conformations and increasing populations of low chirality conformations as the temperature decreases. As the temperature increases eventually all conformations will become equivalent. However, it is of interest that high chirality conformations in these TADDOL derivatives dominate in the temperature regime of typical nematic liquid crystalline materials.

	ϕ_8 dihedral angle population / %					
T / K	α	β	γ	δ	$\alpha+\gamma$	$\beta+\delta$
300	43.5	4.5	44.8	7.2	88.2	11.8
325	34.5	9.0	45.6	10.9	80.1	19.9
350	33.8	10.9	43.5	11.8	77.3	22.7

Table 6.1: Relative populations of low and high chirality conformations for structure B.

Dihedral angles ϕ_1 and ϕ_5 are also of interest. The variation of the chirality order parameter with rotation about ϕ_5 for structure B at 350 K can be seen in figure 6.3b. For conformations with ϕ_5 and $\phi_1 \approx 180^o$ intramolecular hydrogen bonding will occur. For other conformations ($\sim 60^o$ and $\sim 300^o$) intramolecular hydrogen bonding is not possible. Figure 6.3b demonstrates that structures with intramolecular hydrogen bonding generally have greater values of χ than non-hydrogen bonding conformations. For the non-hydrogen bonding conformations of structure B, $\langle\chi\rangle \approx 6$ Å^3 whereas for hydrogen bonding conformations $\langle\chi\rangle \approx 55$ Å^3. In the simulations there is also a trend of increasing non-hydrogen bonding conformations as the temperature increases. For example, for structure B at 300 K 95.9% of structures are intramolecular hydrogen bonding conformations, compared to 93.4% at 325 K and 90.4% at 350 K. In experimental systems the preference of selection of hydrogen bonding conformations in different solvents (for example the preferential selection

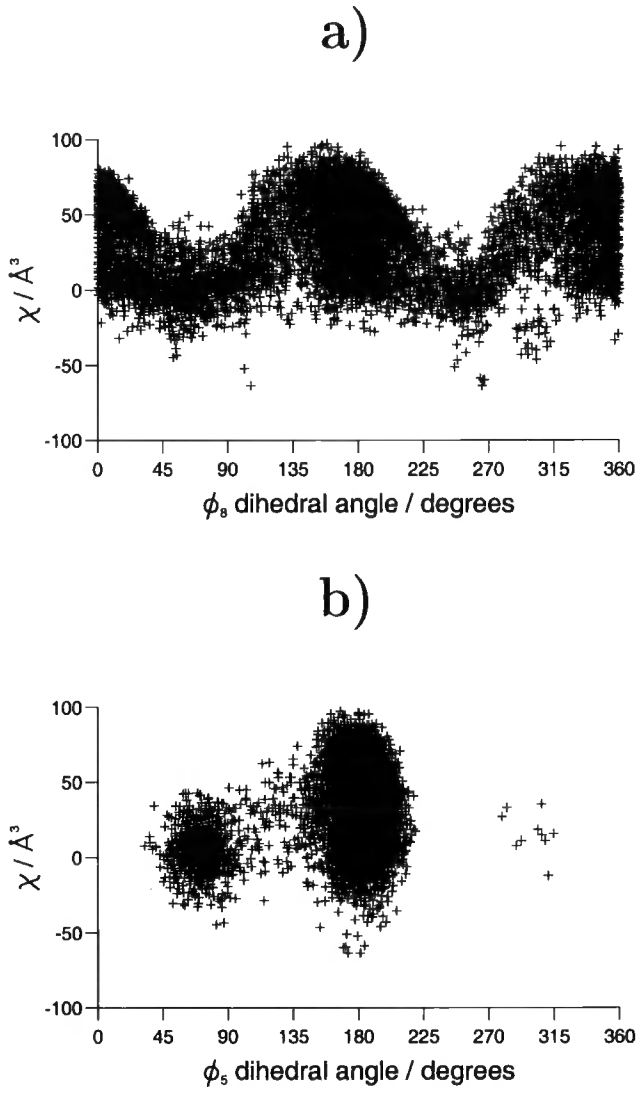

Figure 6.3: Variation of chirality order parameter for structure B at 350 K with a) dihedral angle ϕ_8, b) dihedral angle ϕ_5.

of these conformations in organic non-polar solvents) is expected to have a large impact on the observed HTPs of these systems.

In the experimental system it is likely that the decrease in molecular order of the solvent with temperature will also lead to a decrease in ε, as ε is predicted to be proportional to the order parameter.[173] Together with the solvent effect on conformation, this is likely to contribute most to the difference between experimental and predicted values.

Comparison between χ and $-G_{0S}$

The scaled chiral index, $-G_{0S}$, is also calculated at a number of different temperatures for TADDOL derivative B using the 10000 independent conformations found from the Monte Carlo simulations and at 300 K for derivatives A and C. Results showing the average value of $-G_{0S}$ for the different derivatives compared with χ are shown in table 6.2. For TADDOL derivative B the agreement between the methods

TADDOL	T / K	$\langle\chi\rangle$ /Å^3	$\langle -G_{0S}\rangle$x10^4
A	300	102.09±0.59	43.28±0.19
B	300	53.31±1.05	47.88±1.08
B	325	50.52±1.74	43.13±2.43
B	350	46.86±1.91	40.82±1.88
B	450	34.21±2.56	28.85±2.44
C	300	18.75±1.52	-4.57±0.29

Table 6.2: Comparison between the chirality order parameter, χ, and the scaled chiral index, $-G_{0S}$, for TADDOL derivatives A, B and C.

is very good. This is even more apparent when comparing the values of the chirality measures as a function of dihedral angles $\phi_1 \rightarrow \phi_8$.

Figure 6.4 shows χ and $-G_{0S}$ as a function of $\phi_1 \rightarrow \phi_8$ for derivative B at 450 K. The high temperature is used in order to ensure excellent conformational sampling to facilitate a graphical comparison of the methods. The agreement between χ and $-G_{0S}$ is remarkable, with almost identical behaviour being observed in figure 6.4. However, for TADDOL derivatives A and C the agreement is not as impressive. Of interest is that the scaled chiral index does not appear to be influenced by molecular

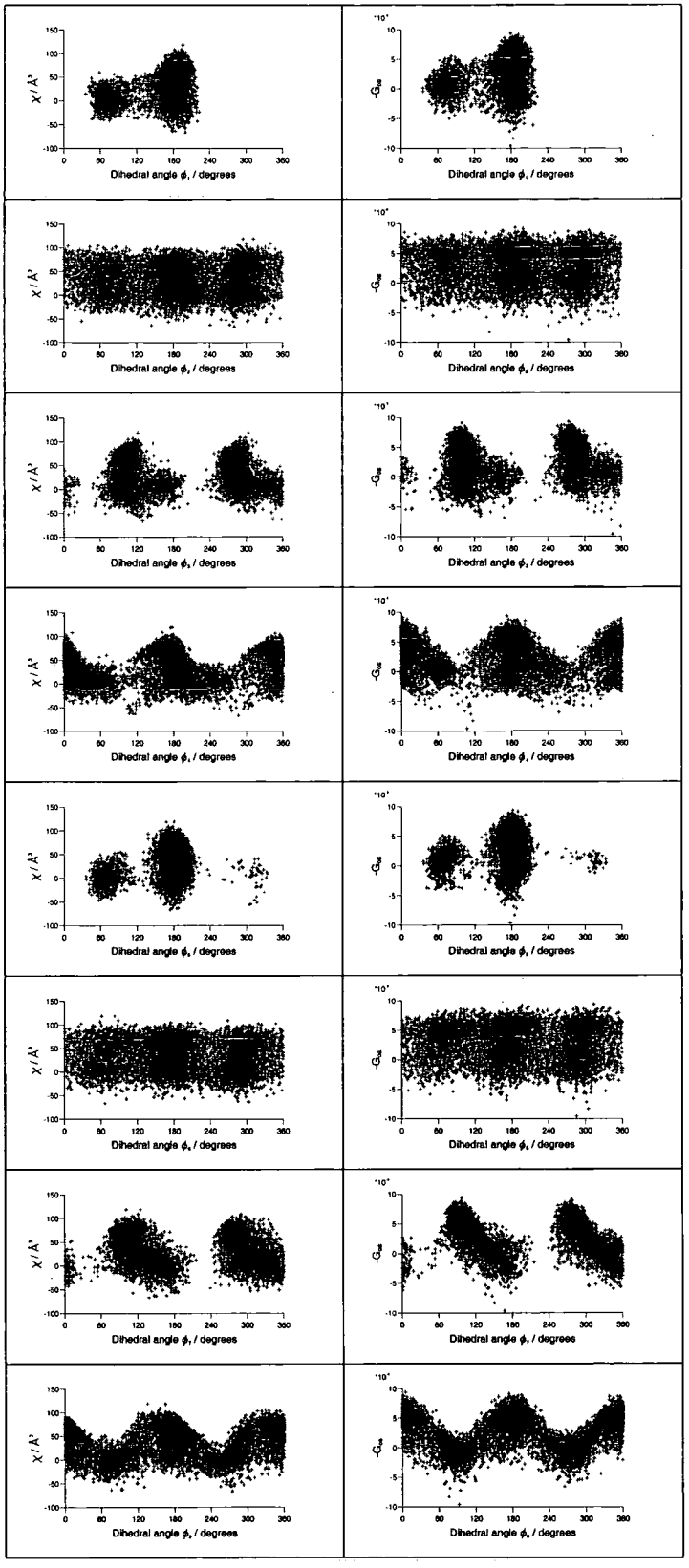

Figure 6.4: The chirality order parameter, χ (calculated using $\varepsilon = 0.05$ Å^{-2}), and the scaled chiral index, $-G_{0S}$, as a function of dihedral angles $\phi_1 \rightarrow \phi_8$ for TADDOL derivative B at 450 K.

extension, unlike the chirality order parameter where longer molecules might be expected to have better ordering in a liquid crystal solvent. Experimentally the HTP of derivative A is approximately twice as large as for derivative B, whereas the scaled chiral index does not vary significantly between the two structures. This is an important weakness if the intention of the calculations is to predict HTPs. It is also curious that the two methods disagree on the sign of chirality for derivative C. This may be due to the different planes of chirality that the two methods sample (see 1,1' binaphthol comparison in section 5.5.3). An important difference in the structure of derivative C compared with A and B is that the rings connected to the TADDOL core are not planar. The comparison between χ and $-G_{0S}$ is continued in section 6.3.2.

6.3.2 Chiral Photochromic Molecule with Variable Helical Twisting Power

In a recent experimental paper by Bobrovsky *et al.*[176] detailed work was conducted on a photosensitive chiral dopant (figure 6.5). The synthesised dopant molecule was found to have an experimental HTP of $\beta_M \approx 45\,\mu m^{-1}$. However, upon exposure to ultra-violet (UV) light the HTP of the dopant was found to decrease significantly. Here, photoisomerisation will occur around a C=C bond forming the Z-E isomer, which can further photoisomerise around the other C=C bond to give the Z-Z isomer (see figure 6.5). The experimental paper does not quote the percentages of each isomer present, but an accurate theoretical study should be able to predict a drop in the HTP as the E-E isomer is photoisomerised.

Gas phase, flexible molecular Monte Carlo simulations are performed on the E-E, the Z-E, and the Z-Z isomers at 400 K. The relatively high temperature ensures excellent conformational sampling, and it should be noted that the calculated value of $\langle\chi\rangle$ does not vary significantly with temperature for these structures. An orienting strength parameter $\varepsilon = 0.05$ Å^{-2} is used to determine the expected HTPs of each of these structures using 10000 conformations from the simulations to calculate an average chirality order parameter, $\langle\chi\rangle$. The average scaled chiral index, $\langle -G_{0S}\rangle$, is also calculated for each isomer and the results are shown in table 6.4. The results

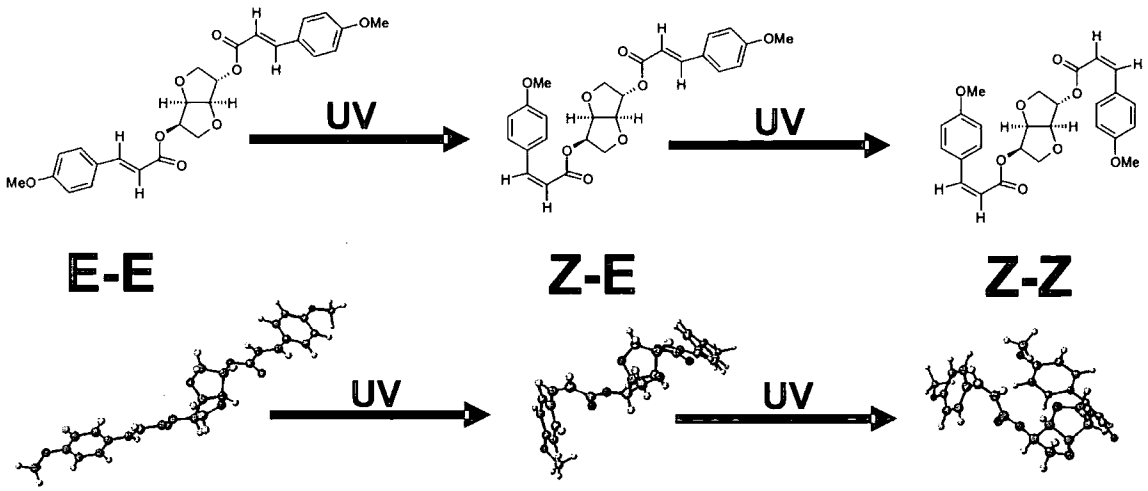

Figure 6.5: Photoisomerisation of an isosorbide chiral dopant when exposed to UV light. Top: Structures of isomers. Bottom: Snapshots from simulation.

Isomer	$\langle\chi\rangle/\text{Å}^3$	$\langle -G_{0S}\rangle \times 10^4$
E-E	49.7±1.6	414.9±3.5
Z-E	8.0±0.9	94.7±3.2
Z-Z	13.8±0.9	42.4±2.0

Table 6.4: Average values of the chirality order parameter and scaled chiral index calculated from simulations for the E-E, the Z-E and the Z-Z isomers of the photochromic isosorbide dopant.

demonstrate that the E-E isomer is theoretically predicted to have a much higher chirality order parameter, and hence HTP, than the Z-E and the Z-Z isomers and therefore explains the drop in HTP upon exposure to UV light. However, the differences between the two methods of calculating chirality is stark and represents a major failure of the scaled chiral index when applied to predicting HTPs. While the chirality order parameter values are of approximately the same order of magnitude as the HTP, the scaled chiral index values are approximately an order of magnitude too high. This contrasts with the results from the rigid molecule study in sections 5.5.2 where the $-G_{0S}$x10^4 values were of approximately the same order of magnitude as the HTP.

It is interesting that the two theories agree well in certain cases (for example, for the case of the rigid bridged-biaryl and helicene derivatives in section 5.5.2 and the remarkable agreement between the two theories for TADDOL derivative B in section 6.3.1) but differ markedly for other systems. There are several reasons why the scaled chiral index may be overestimating the chirality/HTP observed experimentally for the photoisomers studied here. Firstly, the theory does not include any solvent dependent parameters, whereas the surface chirality model is based on a solvent accessible surface with the orienting strength of the medium taken into account in the ε parameter. Secondly, it is possible that the scaled chiral index is sampling planes or aspects of chirality in these systems that do not contribute to the HTP. Thirdly, the index may not be scaling correctly as N becomes large. Recent work[177] has found that contributions to the index from sets of four atoms where one of the atoms is a long distance away from the other three atoms is particularly large. This leads to the intriguing possibility of introducing a cut-off in the calculation of the scaled chiral index.

The remaining studies in this chapter have been conducted using only the surface chirality model to predict chirality/HTPs as all the structures contain a high degree of flexibility and have large N so, not only will the $-G_{0S}$ calculations be computationally expensive, they are also likely to suffer from the same inaccuracies in comparison to the experimental HTP as have been found in the study of the photochromic dopant in this section.

6.3.3 Temperature Dependent Twist Inversion Molecule

In 1992, Goodby *et al.*[178] published experimental findings on the liquid crystalline material S-2-chloropropyl 4'-(4"-n-nonyloxyphenylpropioloyloxy)biphenyl-4-carboxylate which contains a single chiral centre and whose structure is shown in figure 6.6. Their results were surprising and demonstrated that the material underwent an inversion of the helical twist sense in the chiral nematic phase from a left handed twist at lower temperatures to a right handed twist at higher temperatures. They suggested that the helix inverts due to changes in the populations of conformational isomers at different temperatures. However, they were unable to determine the twist senses of individual conformations to confirm their theory for the origin of the twist mechanism.[179] Here the Monte Carlo technique is applied to the material and an attempt to recreate the temperature dependence of the twist-sense and to explain why it occurs are made.

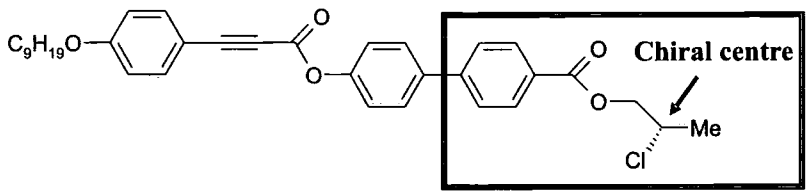

Figure 6.6: Structure of S-2-chloropropyl 4'-(4"-n-nonyloxyphenylpropioloyloxy)biphenyl-4-carboxylate showing the single chiral centre of the molecule. The boxed structure indicates the fragment molecule used in the *ab initio* calculations (a single hydrogen atom is added to the phenyl ring of this structure to complete valence).

An initial investigation into the O-C-C-Cl dihedral angle, around the chiral centre of the molecule, is required as it is known that the MM2 force field does not model dihedral angles of this type correctly. The dihedral angle energy is calculated using density functional theory (DFT) at the B3LYP/6-31G* level for the fragment molecule shown in figure 6.6 and the results are depicted in figure 6.7. The torsional angle is studied at intervals of 15^o and geometry optimisations are carried out at all points. A further geometry optimisation is conducted in each of the three potential wells to ensure the energies of the minima are calculated correctly. The conforma-

tion with the Cl atom *trans* to the core of the molecule (T) is found to be the most stable, followed by the Me group *trans* to the core (G-), with the H atom *trans* to the core ($G+$) being the minima with the highest energy conformations and thus the least favoured of the three potential minima. The calculations differ significantly from those of Goodby *et al.*[179] who found that the H *trans* conformation was more stable than the Me *trans* conformation. However, the latter was carried out using the cruder force field representation within the program CHARMm.[80,81]

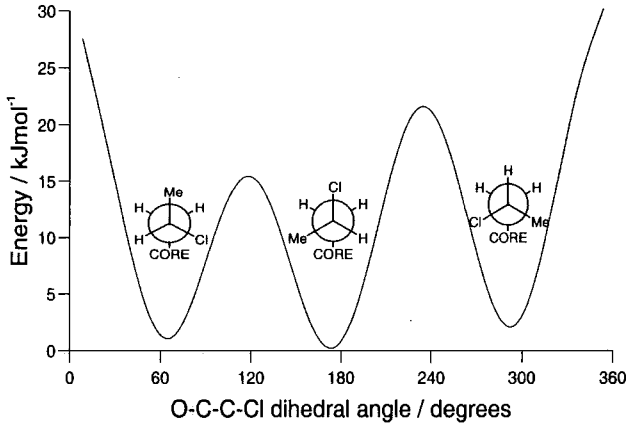

Figure 6.7: Calculated torsional energies for the O-C-C-Cl dihedral angle from DFT calculations at the B3LYP/6-31G* level.

Using the DFT data, the MM2 force field is augmented to reproduce the dihedral angle energy for the O-C-C-Cl dihedral. To do this the dihedral fitting procedure of Cheung *et al.*[54] can be followed, to fit to the torsional terms in the force field. Gas phase, flexible molecular Monte Carlo simulations are then carried out on the molecule at a number of temperatures, and the average chirality order parameter is calculated, along with its standard error, from 10000 conformations from the simulation. In these simulations the orienting strength, ε, is kept constant and its value set to 0.05 $Å^{-2}$ so that changes in the chirality order parameter with temperature can be studied purely as a function of changes in conformational sampling. The results are presented in figure 6.8, and show a twist inversion for the cholesteric liquid crystalline material. The simulations predict the twist inversion to occur at ~530

K whereas in the experimental system the twist inversion occurs at ~414 K. The likely discrepancy here is caused by ignoring the influence of changes in the liquid crystalline environment on conformations and on ε. Despite this, prediction of a sign change in χ is impressive and suggests that the twist inversion can be explained by conformational changes alone.

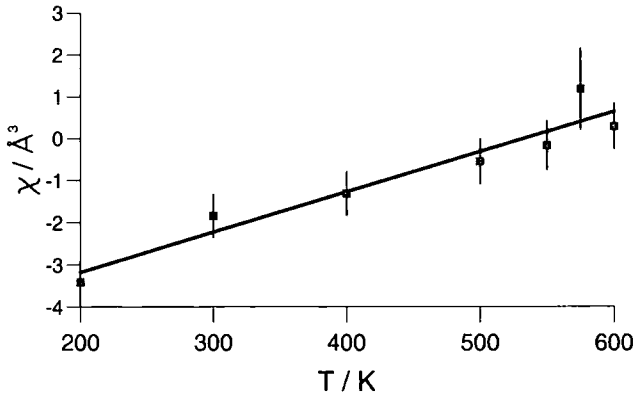

Figure 6.8: The chirality order parameter, χ, as a function of temperature for S-2-chloropropyl 4'-(4"-n-nonyloxyphenylpropioloyloxy)biphenyl-4-carboxylate.

It is now possible to examine the origin of chirality in this molecule and attempt to explain why the twist inversion occurs. A statistical analysis of data for the O-C-C-Cl dihedral at selected temperature points is shown in table 6.5. The relative populations of the *trans*, and two *gauche* states about the O-C-C-Cl dihedral angle are presented along with the average chirality order parameter, χ, for each of the three main states.

From this data it is possible to determine the origin of the twist inversion. At low temperatures, conformations with the O-C-C-Cl dihedral angle in the T position tend to dominate. As these conformations have a net negative chirality associated with them then the overall twist sense of the system is negative. At higher temperatures the population of the T position decreases and those of the $G-$ and $G+$ positions increase, as expected from the DFT. results. The net chirality of the $G-$ conformations is strongly positive and of greater magnitude than the negative con-

	Population / %			$\langle\chi\rangle$ / Å^3		
T / K	*G-*	*T*	*G+*	*G-*	*T*	*G+*
200	18.0	75.4	6.6	7.3	-5.9	-3.9
400	27.3	59.2	13.5	6.5	-4.1	-4.9
550	30.6	53.6	15.8	6.6	-3.4	-2.4
600	31.9	49.5	18.6	5.4	-2.3	-1.4

Table 6.5: Relative populations and chirality order parameters for the three main conformations of the O-C-C-Cl dihedral angle in S-2-chloropropyl 4'-(4"-n-nonyloxyphenylpropioloyloxy)biphenyl-4-carboxylate (O-C-C-Cl dihedral angles $0^o < G- > 120^o, 120^o < T > 240^o, 240^o < G+ > 360^o$).

tributions to chirality of the *T* and *G+* conformations. Thus, as the temperature increases, the negative contribution to chirality from the *T* conformations decreases, the negative contribution from the *G+* conformations increases slightly and the positive contributions from the *G-* conformations increases strongly. Eventually this leads to a helical twist inversion from a left hand (negative χ) twist at lower temperatures to a right hand (positive χ) twist at higher temperatures. Another trend is also apparent in table 6.5. The magnitude of the average chirality arising from the *G-*, *T* and *G+* conformations decreases as the temperature increases. This effect can be explained by a reduction in the orientational order of the molecule at higher temperatures.

It is apparent from this study that the helix twist inversion can be explained by the different weighting of certain molecular conformations, with their associated chiralities, at different temperatures. Emelyanenko[180] and Osipov *et al.*[181] have developed molecular theories of the helical sense inversion based upon the competition between dispersion and steric interactions in these systems and the biaxiality of molecules. It is noted that while the model used here does not explicitly take into account any of these effects it is still able to account for the helical twist inversion purely on the basis of conformational change.

6.3.4 Achiral Banana-Shaped Molecules

In a recent experimental study, Watanabe *et al.*[22] found that a series of achiral banana-shaped molecules with dodecyl tail groups (figure 6.9), when added to a cholesteric liquid crystal, enhanced the twisting power of the chiral nematic phase. In effect the achiral banana-shaped molecules were acting as chiral dopants. The experimental paper proposes that in a chiral nematic liquid crystal the banana-shaped molecules preferentially select chiral conformations with the same handed twist as the chiral phase, and thus enhance the twist of the cholesteric phase in the same way that a normal chiral dopant would. Here, the three molecules in figure 6.9 are simulated. For these larger systems 4 million Monte Carlo steps are required for convergence of average quantities, and the calculations are carried out at 400 K with an orienting strength parameter $\varepsilon = 0.05$ Å^{-2}. 20000 conformations are used to determine an average chirality order parameter.

S-12-O-PIMB

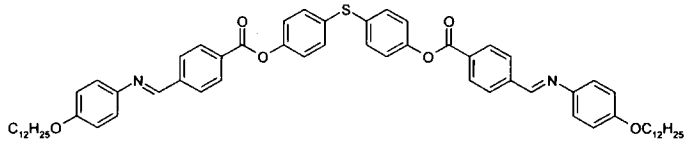

P-12-O-PIMB

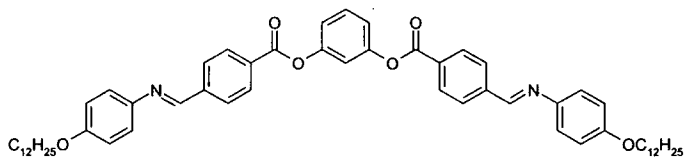

N-12-O-PIMB

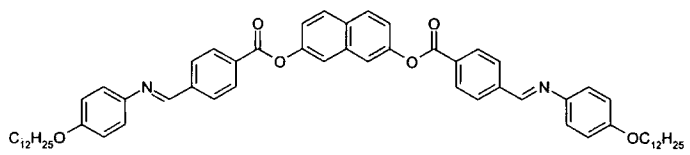

Figure 6.9: Chemical structures of the three achiral banana molecules studied.

As expected, each of the molecules is found to be achiral within the statistical

error of the results ($\langle\chi\rangle = (0.05 \pm 6.58)$ Å^3 for S-12-O-PIMB, $\langle\chi\rangle = (0.25 \pm 3.93)$ Å^3 for P-12-O-PIMB and $\langle\chi\rangle = (-1.99 \pm 11.49)$ Å^3 for N-12-O-PIMB). However, during the simulations the molecules adopted a number of conformations with extremely high magnitudes of chirality associated with them. For example, ~20% of the conformations adopted have $|\chi| \geq 500$ Å^3 and ~2% of the conformations have $|\chi| \geq 1000$ Å^3. It should be noted that χ is not a function of molecular size and that a conformation with $\chi \approx 500$ Å^3 corresponds to $\beta_M \approx 1000\ \mu m^{-1}$, which is much higher than any helical twisting power that has been measured experimentally for chiral systems. Even a small increase in the proportion of left-handed or right-handed chiral conformations sampled by these banana-shaped molecules in the twisted nematic liquid crystal phase would have a relatively large effect on the twist of the system due to the extremely high HTPs of the chiral conformations. Thus, it seems likely in the experiments that the chiral nematic phase is preferentially selecting chiral conformations that twist in the same direction.

6.3.5 Predictive studies of the twisting power of bridged biaryl derivatives to aid in future synthetic strategies

Bridged biaryl/binaphthyl derivatives have been extensively used as chiral dopants that can induce highly twisted nematic mesophases.[166] The origin of chirality in these molecules comes from limited rotation about the 1,1' torsional angle between the two naphthyl planes. Bridging of the molecules effectively locks the torsional angle to approximately 40-60^o, making the molecules chiral. Bridged biaryl/binaphthyl derivatives have been found to have much higher HTPs than unbridged structures, whose 1,1' torsional angles are unconstrained and preferentially adopt conformations where the dihedral angle $\approx 90^o$. A theoretical study by Ferrarini *et al.*[28] and the results in section 5.5.3 for the 1,1' binaphthyl molecule have shown that structures with 1,1' dihedral angles $\approx \pm 45^o$ or $\pm 135^o$ are expected to have higher helical twisting powers, β_M, than other dihedral angles. Recent experimental and theoretical work[156,168] has also found that the HTP of these bridged derivatives increases as the length of substituents on the 6,6' positions of the molecule increases. A rigorous theoretical analysis of the longer and more flexible derivatives was unable to be carried

out in the previous study[156] however, due to the large number of conformations that the molecules are able to adopt. The Monte Carlo simulation approach described previously is ideal for the study of these structures. In this section the effects of adding substituents to the 4,4', the 6,6', and the 7,7' positions of the bridged biaryl molecule in figure 6.10 are examined.

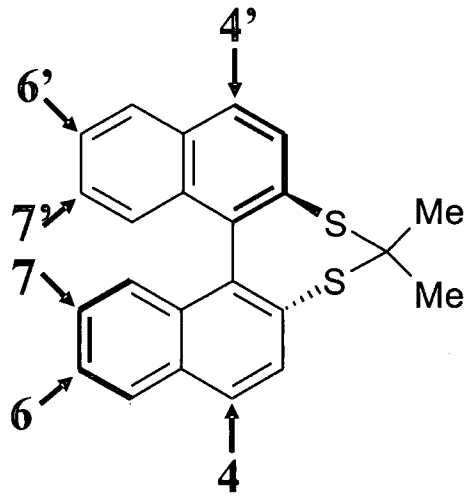

Figure 6.10: Bridged biaryl molecule studied with arrows showing the locations of the 4,4', the 6,6' and the 7,7' positions.

Figure 6.11 shows the substituents studied and table 6.6 gives the details of which substituents are attached in each position for the molecules simulated. The simulation procedure detailed above in section 6.2 is used and 10000 conformations for each molecule contributed to an average chirality order parameter. Results for each of the molecules is shown in table 6.7. The results demonstrate that substitution of the 6,6' position can greatly affect the HTPs of bridged biaryl derivatives. Of particular note are molecules E5 and E6, where substitution of the 6,6' position results in an average chirality order parameter approximately three times larger than the unsubstituted molecule. Molecules E2 and E4 show a reduction in χ compared to the unsubstituted molecule. These molecules differ from the others in the study in that the substitution is generally out of the plane of the naphthyl ring. This shows that molecular extension is not the only factor to take into account when considering the effect on the HTP of adding substituents to bridged biaryl molecules. Also of

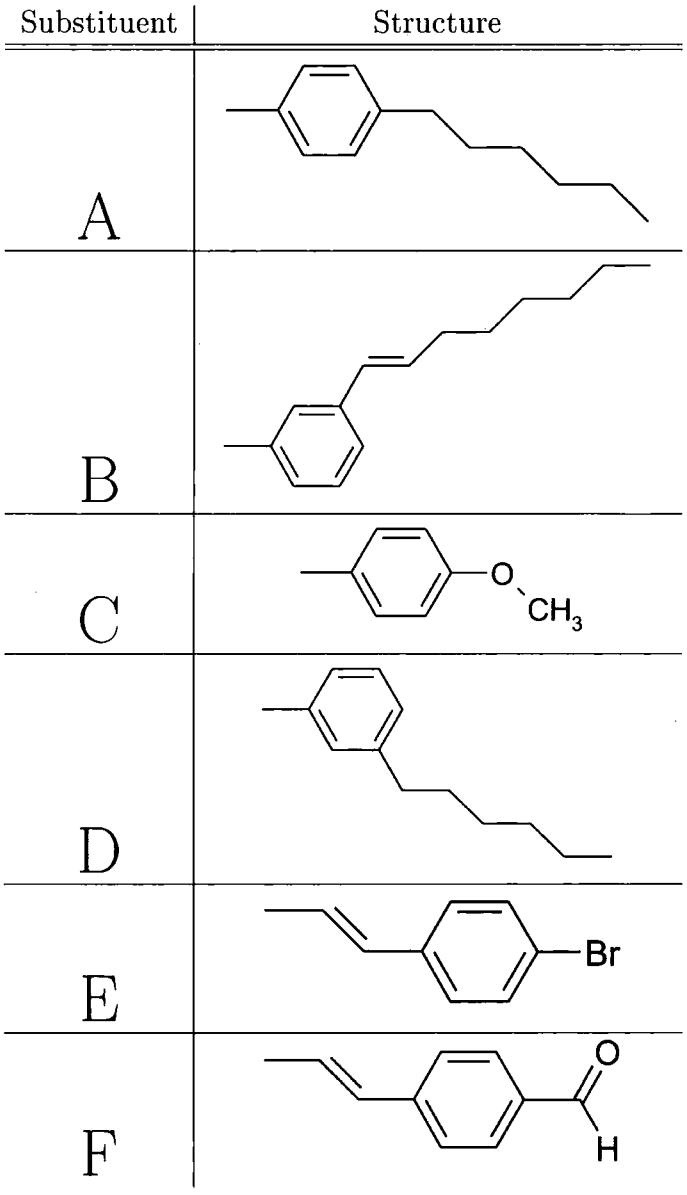

Figure 6.11: Derivatives added in various positions to the bridged biaryl molecule in figure 6.10.

	Position		
Molecule	4,4'	6,6'	7,7'
E0			
E1		A	
E2		B	
E3		C	
E4		D	
E5		E	
E6		F	
E7	A	A	
E8			E
E9	E		E

Table 6.6: Bridged biaryl derivatives studied. Each molecule has the core structure shown in figure 6.10 with substituents from figure 6.11 added to the positions marked.

Molecule	$\langle\chi\rangle/\text{Å}^3$
E0	-39.1
E1	-70.5±0.7
E2	-38.3±10.6
E3	-53.0±1.0
E4	-21.3±2.6
E5	-117.6±1.1
E6	-119.0±1.1
E7	-87.3±1.7
E8	-79.9±2.1
E9	-15.5±4.6

Table 6.7: Average chirality order parameter, χ, obtained from simulations for the nine bridged biaryl molecules whose structures are given in table 6.6. E0 is the rigid unsubstituted molecule.

interest is the effect of substitution in the 4,4' and 7,7' positions. Molecule E8 shows that substitution of the 7,7' position increases χ, but comparison with molecule E5 indicates that substitution of the 6,6' position results in even higher values of χ. In molecule E7, substituents are added to the 4,4' and 6,6' positions. Comparison with molecule E1 demonstrates that for the particular substituent studied, additional substitution of the 4,4' position increases χ. However, for the case of molecule E9, substitution of the 4,4' position in addition to the 7,7' position resulted in a large decrease in χ.

Future work on this class of molecule would clearly be of interest, given the results found here. In particular, results from experimental work would be invaluable. The direction of future theoretical and experimental work on this class of molecule should concentrate on substituents of greater length, look further at the effects of 4,4' substitution and examine the effects of combining 6,6' and 7,7' substitution. With regard to new substituents, biphenyl derivatives of substituents E and F in table 6.11 may be good candidates, not only because of the increase in overall length, but also as they would help order the molecule within the liquid crystalline environment and may improve solubility in a liquid crystal solvent.

6.4 Conclusions and Further Work

In this chapter a molecular Monte Carlo simulation approach, coupled with calculations of the chirality order parameter and the scaled chiral index, has been used to study a range of chiral molecules and systems. The method has been successful in predicting helical twisting powers for flexible chiral dopants, in predicting the temperature dependence of HTPs, and has demonstrated a temperature induced helical twist inversion. Extraordinarily high HTP values for some conformations exhibited by achiral banana molecules have been shown. This in turn suggests that chiral conformations with the same twist sense as the twisted nematic phase are being preferentially selected. The method has also been used in predictive studies of compounds that have not yet been synthesised, and points to possible routes for future synthetic studies.

This work has been restricted to simulations of molecules in the gas phase due to the computational cheapness of this approach and the excellent conformational sampling that can be achieved. It is important to note that a liquid crystalline solvent would be expected to affect the relative weighting of conformations sampled by the molecule, and thus influence the chirality of the system. Indeed, these solute-solvent effects may account for the exaggerated temperature dependence of the HTP in the experimental system compared to the simulations for the TADDOL derivatives and may also explain differences in the predicted and experimental temperatures for helical twist inversion for S-2-chloropropyl 4'-(4"-n-nonyloxyphenylpropioloyloxy)biphenyl-4-carboxylate. The method used here could be adapted to more complicated systems where a liquid crystalline solvent (either coarse-grained[41,48] or fully atomistic) could be included in the simulations. In these cases, different conformations (with different chiralities) are expected to be preferentially selected in different solvents, thus accounting for solvent dependent HTPs. By including a fully atomistic liquid crystal solvent it would then be possible to study the role of electrostatic interactions on the helical twisting power of chiral dopants.

Chapter 7

Calculations of Molecular Chirality from Intermolecular Torques

7.1 Introduction

In a previous computational study by Germano *et al.*,[38] systems of liquid crystalline chiral Gay-Berne (GB) particles were examined. The model potential for the GB particles was comprised of an achiral part from the standard Gay-Berne potential[41] (section 2.2.4) and a chiral part using the form proposed by Memmer and Kuball.[69] They found that values of intermolecular torques in these systems could be directly related to the chiral strength of the constituent molecules. In this chapter, the approach of Germano *et al.*[38] is extended to systems of achiral liquid crystalline particles doped with a single chiral molecule, and the values of intermolecular torques measured in the systems are related to the helical twisting powers of the chiral dopant molecules.

7.2 Theory

Following Germano *et al.*[38] one can define the total potential energy of a system as U_λ, so that it depends on a chirality parameter, λ. λ is a measure of chirality in a system and it is noted that an achiral system has $\lambda = 0$ and enantiomeric systems have opposite signs of λ. The equilibrium pitch wave-number of a system

can similarly be defined as:

$$q_\lambda = \frac{2\pi}{P_0}. \tag{7.1}$$

Comparison with equation 4.1 in chapter 4 shows that q_λ is directly proportional to the microscopic helical twisting power, β, of a chiral dopant molecule:

$$q_\lambda = \frac{4\pi\beta}{V}\left[N_+ - N_-\right], \tag{7.2}$$

where V is the volume of the system and $N_\pm$ are the number of dopant molecules, of opposite handedness, added to the system. Now, following Allen,[32] if a uniformly twisted nematic with a wavevector $k = 2\pi/P$, is doped with small numbers of chiral dopants ($N_\pm$) then the elastic contribution to the free energy arising from distortions to the uniformly twisted state is

$$F_{k,\lambda} = \frac{1}{2}VK_2(k - q_\lambda)^2, \tag{7.3}$$

where K_2 is the twist elastic constant. Now, the free energy difference between enantiomeric phases with equilibrium pitch wave-numbers $q_{\pm\lambda} = \pm q_\lambda$ is

$$\begin{aligned} \Delta F_{k,\pm\lambda} &\equiv F_{k,\lambda} - F_{k,-\lambda} \\ &= \tfrac{1}{2}VK_2\left[(k - q_\lambda)^2 - (k + q_\lambda)^2\right] \\ &= -2VK_2q_\lambda k\,. \end{aligned} \tag{7.4}$$

This expression is equivalent to equation 4.2 that is evaluated in chapter 4 using thermodynamic perturbation theory to calculate the helical twisting power (HTP) of a chiral dopant molecule, where k is the wavevector imposed on the system by twisted periodic boundary conditions.[130]

An alternative method can also be used to calculate q_λ, and hence β, that is based on intermolecular torques. Following de Gennes[158] and Allen and Masters,[130,182] the free energy density gives rise to a torque density, and the torque per unit area can be expressed microscopically as:

$$\frac{\partial F_{k,\lambda}}{\partial k} = \langle \Pi_{zz} \rangle_{k,\lambda}\,, \tag{7.5}$$

where the helical axis is chosen along the z axis and the tensor $\Pi_{\alpha\beta}$ is defined as:

$$\begin{aligned} \Pi_{\alpha\beta} &= -\sum_i r_{i\alpha}\tau_{i\beta} \\ &= -\tfrac{1}{2}\sum_{i\neq j} r_{ij\alpha}\tau_{ij\beta} \\ &= -\tfrac{1}{2}\sum_{i<j} r_{ij\alpha}(\tau_{ij\beta} - \tau_{ji\beta}), \end{aligned} \tag{7.6}$$

where $\alpha, \beta = x, y, z$; $r_{ij\alpha} = r_{i\alpha} - r_{j\alpha}$ is the α component of the centre of mass separation of particles i and j, and $\tau_{ij\beta}$ is the β component of the torque exerted by particle j on particle i.

Following Germano *et al.*,[38] comparison of equation 7.6 with equation 7.3 gives:

$$\frac{1}{V}\frac{\partial F_{k,\lambda}}{\partial k} = K_2(k - q_\lambda). \tag{7.7}$$

Utilising equation 7.5, the case where $k = 0$ leads to the equation

$$-\frac{\langle \Pi_{zz}\rangle_{0,\lambda}}{V} = K_2 q_\lambda \equiv h_\lambda, \tag{7.8}$$

and the case where $k \neq 0$ leads to

$$-\frac{\langle \Pi_{zz}\rangle_{k,\lambda}}{V} = K_2(q_\lambda - k). \tag{7.9}$$

Thus, K_2 and q_λ can be determined from

$$K_2 = \frac{\langle \Pi_{zz}\rangle_{k,\lambda} - \langle \Pi_{zz}\rangle_{0,\lambda}}{Vk}, \tag{7.10}$$

$$q_\lambda = \frac{-k\,\langle \Pi_{zz}\rangle_{0,\lambda}}{\langle \Pi_{zz}\rangle_{k,\lambda} - \langle \Pi_{zz}\rangle_{0,\lambda}}. \tag{7.11}$$

Equation 7.10 was used by Allen and Masters[130] to calculate K_2 in fluids of achiral molecules. However, the quantity of interest in this chapter is the microscopic HTP, β, that is directly proportional to q_λ. From equation 7.8, a single simulation of a chiral molecule in an untwisted nematic ($k = 0$) will yield h_λ, which is directly proportional to q_λ, and thus β.

7.3 Computational and Simulation Details

The approach utilised in this chapter to calculate HTPs for chiral dopant molecules is to use equation 7.8 to determine the factor $K_2 q_\lambda$ by calculating $\langle \Pi_{zz} \rangle_{0,\lambda}$ from a simulation of a chiral molecule in a nematic solvent.

In this chapter, fully atomistic, rigid, energy minimised structures of chiral molecules are simulated in a Gay-Berne liquid crystalline solvent. The solute and solute-solvent model is identical to the one described in chapter 4 for the combined solute-Gay-Berne system. The Gay-Berne (GB) solvent used uses the parameters $\kappa = 3$, $\kappa' = 5$, $\mu = 2$ and $\nu = 1$, which were previously studied by de Miguel and co-workers.[59] As in chapter 4, the simulation constants are set to $\sigma_0^{GB} = 5.7$ Å, and $\epsilon_0^{GB} = 3.32576$ kJ/mol, and a reduced density of $\rho^* = 0.33$ is used that corresponds to a stable nematic liquid crystalline phase with an order parameter $S_2 \approx 0.7$ at a temperature $T = 400$ K. A solvent system of 243 GB particles is used. Throughout this chapter, Monte Carlo (MC) simulations in the NVT ensemble are used as the simulation technique.

The simulations proceed as follows: the solute molecule is initially 'grown' into the solvent using the insertion technique developed in chapter 4, and the system is then equilibrated for 1-2x10^5 MC steps to ensure that the solvent is well ordered around the chiral solute molecule. Production runs of 1.6-2.5x10^7 MC steps are then performed and the tensor Π_{zz} is calculated (see below) at each step. Averages are calculated over blocks of 5x10^5 MC steps, so that between 32 and 50 independent block averages contribute to the overall $\langle \Pi_{zz} \rangle$ for each system studied.

Π_{zz} is determined from equation 7.6. The torque between GB particles is calculated as

$$\tau_{ij} = -\hat{\mathbf{e}}_i \times \frac{\partial U_{ij}}{\partial \hat{\mathbf{e}}_i}, \tag{7.12}$$

where $-\frac{\partial U_{ij}}{\partial \hat{\mathbf{e}}_i}$ is the perpendicular component of the 'gorque' acting on particle i from particle j. The torque on the solute molecule is determined as:

$$\tau_i = \sum_{i=1}^{n} \mathbf{d}_i \times \mathbf{f}_i, \tag{7.13}$$

where n is the number of atoms in the molecule, $\mathbf{d}_i$ is the position of atom i in relation to the centre of mass of the molecule, and $\mathbf{f}_i$ is the force acting on molecule i. Equation 7.13 can easily be decomposed into contributions to the torque from individual GB particles for use in equation 7.6, and the torque acting on a GB particle from the molecule is determined from the 'gorque' as in equation 7.12.

In order to improve the averaging of Π_{zz}, the nematic director is constrained to be perpendicular to the z axis. Following Germano *et al.*[38,183] the director is constrained to the xy plane by adding a term proportional to $(Q_{xz}^2 + Q_{yz}^2)$ to the total energy of the system, U_λ, where $\mathbf{Q}$ is the order tensor given by:

$$Q_{\alpha\beta} = \frac{1}{N}\sum_{i=1}^{N}\left(\frac{3}{2}\hat{e}_{i\alpha}\hat{e}_{i\beta} - \frac{1}{2}\delta_{\alpha\beta}\right),$$

where $\hat{\mathbf{e}}_i$ is a unit vector along the main molecular axis of particle i, N is the number of particles, and δ is the Kronecker delta function.

The chiral molecules studied are molecules 1, 4, 7, M1 and its enantiomer, and M4. These molecules are studied using chiral measures in chapter 5 and their structures are shown in figure 5.1. A pure Gay-Berne solvent system containing no chiral dopant is also studied to check that an achiral system has $\langle\Pi_{zz}\rangle_{0,0} \approx 0$.

7.4 Results and Discussion

The results from the study are shown in figure 7.1 where $\langle\Pi_{zz}\rangle_{0,\lambda}$ is plotted against the experimental helical twisting power of the chiral dopants. As predicted from equation 7.8, $\langle\Pi_{zz}\rangle_{0,\lambda}$ has the opposite sign to the helical twisting power (and hence q_λ). In each case, the correct sign of twist is predicted using the method and there is a trend of higher values of $\langle\Pi_{zz}\rangle_{0,\lambda}$ at larger HTP values. The results for the achiral system containing no chiral dopant molecules is also shown in figure 7.1, and within statistical errors, the system was found to be achiral using the method ($\langle\Pi_{zz}\rangle_{0,\lambda} = -0.18 \pm 1.78$).

The results from this study show that the calculation of intermolecular torques in liquid crystalline systems doped with chiral molecules can be used to predict

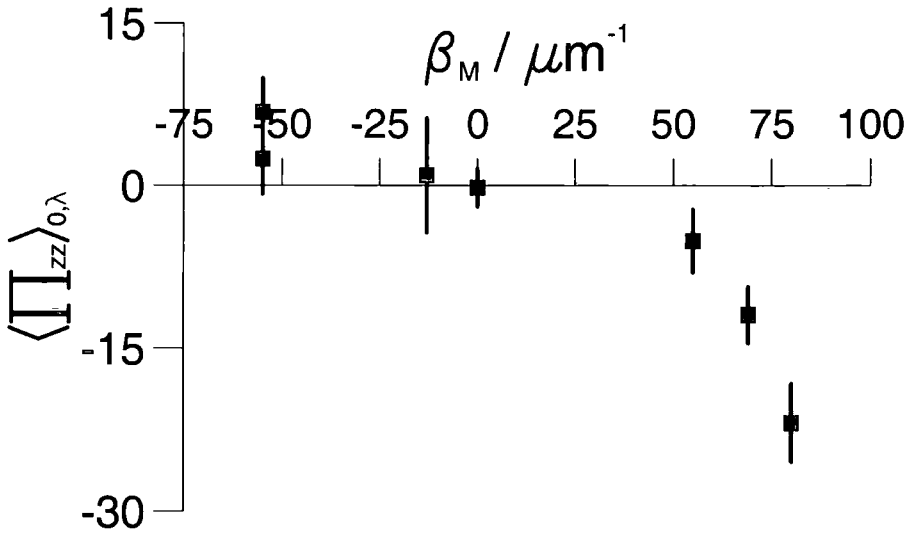

Figure 7.1: $\langle \Pi_{zz} \rangle_{0,\lambda}$ plotted against β_M for six different chiral dopants in a Gay-Berne solvent and for a purely achiral system ($\beta_M = 0$).

the handedness of the twist induced by a chiral molecule and can also yield an approximate measure of the magnitude of the twist. However, the method is subject to large statistical errors. The size of the error in $\langle \Pi_{zz} \rangle$ depends critically on the system size and the length of the simulation. The liquid crystalline solvent system must be small enough to allow the chiral molecule to have a measurable impact on the system above the background 'noise' caused by normal fluctuations in Π_{zz}. However, fluctuations in Π_{zz} are larger for smaller system sizes so the choice of system size used requires careful consideration. The computational cost must also be taken into account in this consideration. Larger system sizes are more computationally expensive, and therefore the collection of statistics is more time consuming. The system size used in this study; namely 243 GB solvent particles and one atomistic chiral molecule, was chosen in an attempt to provide the best balance between these factors.

In the previous computational study by Germano *et al.*,[38] systems of 1024 and 2048 chiral GB particles were examined. However, chirality was imparted on all

molecules in the study and the strength of the chiral potential used was in most cases one or two orders of magnitude larger than would be expected for real molecules. For this reason, much shorter simulation runs could be used in the previous study compared to those presented in this chapter where only one molecule is chiral (6×10^5 MC steps in the previous study compared to $1.6 \rightarrow 2.5 \times 10^7$ MC steps in this chapter).

It should be noted that the general method is extremely flexible and allows for the use of many different system sizes and types. A system that includes several chiral dopant molecules in a generic liquid crystalline solvent of Gay-Berne[41] or soft repulsive spherocylinder[48] particles could be used and would produce a larger, and more measurable twist than the system utilised in this study but would result in an increase in the computational cost caused by simulating another fully atomistic molecule (electrostatic interactions between molecules would also have to be considered). The approach could be extended to allow the chiral molecule to change conformations by utilising the computational methods used and discussed in chapter 6. In addition, the method could also be applied to systems where the liquid crystalline solvent is represented by molecules with atomistic detail. Although these studies would be far too computationally expensive to be considered given the computational power currently available, they may become accessible in the future and would allow studies of solvent dependent helical twisting powers to be undertaken.

7.5 Conclusions

The method of calculating intermolecular torques in liquid crystalline systems containing chiral dopant molecules has been shown to correctly predict the handedness of twist induced by the chiral molecules. The general method could be adapted to systems containing many chiral dopant molecules in a liquid crystalline solvent. To provide a reliable quantitative measurement of the helical twisting power for a chiral dopant molecule, the method requires further refinement to improve the statistical error in the results and to find the optimum ratio of chiral dopant molecules to liquid crystalline molecules used in the simulation system.

Chapter 8

Conclusions

The work presented in this thesis has used computational and theoretical techniques to provide predictions of molecular chirality and helical twisting powers for liquid crystalline chiral dopant molecules.

The first technique used to predict helical twisting powers (HTPs) for liquid crystalline chiral dopants employed Monte Carlo free energy calculations. The work was based on an original computational technique proposed by Cook and Wilson, which involved simulating a chiral nematic phase using a Gay-Berne solvent in a simulation box subject to twisted periodic boundary conditions. A series of Monte Carlo simulations were used to grow an atomistic model of a chiral dopant into this solvent and statistical perturbation theory was used to measure the free energy change for this process. Comparison of the free energy difference obtained from this calculation for a particular enantiomer and its mirror image allows a calculation of the HTP of the chiral dopant to be made. For some initial test molecules this technique was found to correctly predict the sign of the induced twist and, when compared with with experimental work, calculated HTPs with a reasonable degree of accuracy. One of the main problems of the existing technique was its high computational cost. This was mainly due to the computationally expensive Gay-Berne solvent-solvent interactions involved in the simulations. The work presented in chapters 3 and 4 of this thesis concentrated on reducing the computational costs of the method by examining a solvent system with a much cheaper computational model, namely the Soft Repulsive Spherocylinder (SRS) system. Simulations of SRS particles were de-

scribed in chapter 3 and constitute the first detailed study of the SRS potential. The isotropic, nematic and smectic-A phases were found in the phase diagram of SRS particles with a total length to breadth ratio of 5:1 ($L/D = 4$). In chapter 4, the first of the four techniques used for calculating the HTPs of liquid crystal chiral dopants in this thesis was presented. This chapter also includes work that was conducted on improving the accuracy and efficiency of the free energy calculations used in the technique and describes the results of the simulations using a SRS and Gay-Berne solvent. The final simulations conducted using an optimised free energy pathway and the SRS solvent were able to correctly predict the handedness of twist for the chiral dopant molecules studied and provided reasonable estimates of the magnitude of the HTP. Although these are not as impressive as the results from the original Cook/Wilson technique, the computational cost of the method is four times cheaper. The approach has several drawbacks including the computational cost ($\sim$ 2 days for each molecule), the instability of the simulation system, the large statistical errors involved in the approach and the limited applicability of the method (it is only applicable for relatively rigid chiral molecules).

In chapters 5 and 6, the chirality order parameter and the scaled chiral index were applied to a number of chiral dopant molecules and systems. These chiral measures are single molecule techniques that, for a given molecular conformation, can provide a rapid calculation of chirality/HTP. Due to their computational cheapness, these methods are of great interest as they could be used to rapidly screen large numbers of chiral molecules for high HTP values prior to synthesis. In chapter 5, both the scaled chiral index and the chirality order parameter were found to show a good correlation with experimentally determined helical twisting powers for a range of relatively rigid bridged biaryl and helicene derivative molecules. In chapter 6, the two chiral measures were incorporated in Monte Carlo simulations of flexible chiral molecules. The method was applied to a number of systems and, using the chirality order parameter, it was possible to successfully predict helical twisting powers for flexible chiral dopants. The method was also used to predict the temperature dependence of HTPs, to demonstrate a temperature induced helical twist inversion, show extremely high HTP values for some conformations exhibited by achiral banana molecules, and

was used in a predictive study to aid in future synthetic strategies of bridged-biaryl molecules. Of all the techniques used in this thesis, this has been the most successful. Its relatively cheap computational cost (approximately 2-3 hours for each flexible molecule and $\sim$1 s for a rigid structure) makes it particularly attractive for uses in screening chiral dopant molecules prior to synthesis.

In chapter 7 a new approach was used that directly measures the impact of a chiral molecule on a liquid crystal solvent. Using statistical mechanics it is possible to relate the torque a chiral molecule induces in a solvent, as chirality is transferred to the system, to the helical twisting power. These simulations, whilst being computationally expensive and requiring excellent statistics, show that it is possible to predict the correct sign of induced twist for a chiral dopant molecule by measuring intermolecular torques.

Bibliography

[1] F. Reinitzer, Monatshefte fur Chemie **9**, 421 (1888).

[2] O. Lehmann, Krist. **18**, 464 (1889).

[3] L. Gatterman and A. Ritschke, Ber. Dtsch.Chem. Ges. **23**, 1738 (1890).

[4] F. Meyer and K. Dahlem, Liebigs Ann. **320**, 122 (1902).

[5] G. Friedel, Ann. Physique **18**, 273 (1922).

[6] D. Vorlander. *Chemische Kristallographie der Flussigkeiten.* Akadem, Leipzig (1924).

[7] G. W. Gray and J. W. Goodby. *Smectic liquid crystals: Textures and Structures.* Leonard Hill (1984).

[8] S. Chandrasekhar, B. K. Sadashiva and K. A. Suresh, Pramana **9**, 471 (1977).

[9] K. Hiltrop. In H. Baumgartel, E. U. Frank, W. Grunbein and H. Stegemeyer, editors, *Liquid Crystals*, chapter 4. Springer, New York (1994).

[10] W. Thomson. *Baltimore Lectures on Molecular Dynamics and the Wave Theory of Light.* Cambridge University Press (1904).

[11] M. Daumas. *Arago, 1786-1853: la jeunesse de la science.* Paris (1987).

[12] F. Lefort. *Notice sur la vie et les travaux de Biot.* Paris (1867).

[13] L. Pasteur, C. R. Hebd. Sean. Acad. Sci. Paris **26**, 535 (1848).

[14] R. S. Cahn, C. K. Ingold and V. Prelog, Angew. Chem. Int. Ed. **5**, 385 (1966).

[15] P. P. Crooker. In H. S. Kitzerow and C. Bahr, editors, *Chirality in Liquid Crystals*, pages 186–250, Chapter 7. Springer-Verlag, New York (2001).

[16] J. W. Goodby, M. A. Waugh, S. M. Stein, E. Chin, R. Pindak and J. S. Patel, Nature **337**, 449 (1989).

[17] J. W. Goodby, Curr. Opin. Colloid In. **7**, 326 (2002).

[18] G. Pelzl, S. Diele, A. Jakli, C. Lischka and I. W. and. W. Weissflog, Liq. Cryst. **26**, 135 (1999).

[19] A. Jakli, C. L. and. W. Weissflog, G. Pelzl and A. Saupe, Liq. Cryst. **27**, 1405 (2000).

[20] C. K. Lee and L. C. Chien, Liq. Cryst. **26**, 609 (1999).

[21] W. Weissflog, H. Nadasi, U. Dunemann, G. Pelzl, S. Diele, A. Eremin and H. Kresse, J. Mater. Chem. **11**, 2748 (2001).

[22] J. Thisayukta, H. Niwano, H. Takezoe and J. Watanabe, J. Am. Chem. Soc. **124**, 3354 (2002).

[23] P. van de Witte, E. E. Neuteboom, M. Brehmer and J. Lub, J. Appl. Phys. **85**, 7517 (1999).

[24] H. Yang, H. Yamane, H. Kikuchi, H. Yamane, G. Zhang, X. F. Chen and K. Tisato, J. Appl. Polymer Science **73**, 623 (1999).

[25] C. Stützer, W. Weissflog and H. Stegmeyer, Liq. Cryst. **21**, 557 (1996).

[26] S. N. Yarmolenko, L. A. Kutulyas, V. V. Vashchenko and L. V. Chepeleva, Liq. Cryst. **16**, 877 (1994).

[27] A. Ferrarini, G. J. Moro and P. L. Nordio, Liq. Cryst. **19**, 397 (1995).

[28] A. Ferrarini, G. J. Moro and P. L. Nordio, Phys. Rev. E **53**, 681 (1996).

[29] A. Ferrarini, G. J. Moro and P. L. Nordio, Molec. Phys. **87**, 485 (1996).

[30] L. Feltre, A. Ferrarini, F. Pacchiele and P. L. Nordio, Molec. Cryst. Liq. Cryst. **290**, 109 (1996).

[31] M. J. Cook and M. R. Wilson, J. Chem. Phys. **112**, 1560 (2000).

[32] M. P. Allen, Phys. Rev. E **47**, 4611 (1993).

[33] M. A. Osipov, B. T. Pickup and D. A. Dunmur, Molec. Phys. **84**, 1193 (1995).

[34] M. Solymosi, R. J. Low, M. Grayson and M. P. Neal, J. Chem. Phys. **116**, 9875 (2002).

[35] M. Solymosi, R. J. Low, M. Grayson, M. P. Neal, M. R. Wilson and D. J. Earl, Ferroelectrics **277**, 169 (2002).

[36] M. P. Neal, M. Solymosi, M. R. Wilson and D. J. Earl, J. Chem. Phys. **119**, 3567 (2003).

[37] M. A. Osipov and H. G. Kuball, Eur. Phys. J. E **5**, 589 (2001).

[38] G. Germano, M. P. Allen and A. Masters, J. Chem. Phys. **116**, 9422 (2002).

[39] M. J. Cook, Ph.D. thesis, University of Durham (2000).

[40] B. J. Berne and P. Pechukas, J. Chem. Phys. **56**, 4213 (1972).

[41] J. G. Gay and B. J. Berne, J. Chem. Phys. **74**, 3316 (1981).

[42] E. de Miguel, E. M. del Rio, J. T. Brown and M. P. Allen, J. Chem. Phys. **105**, 4234 (1996).

[43] G. R. Luckhurst, R. A. Stephens and R. W. Phippen, Liq. Cryst. **8**, 451 (1990).

[44] D. Frenkel, J. Phys. Chem. **92**, 3280 (1988).

[45] J. A. C. Veerman and D. Frenkel, Phys. Rev. A **41**, 3237 (1990).

[46] S. C. McGrother, D. C. Williamson and G. Jackson, J. Chem. Phys. **104**, 6755 (1996).

[47] P. Bolhuis and D. Frenkel, J. Chem. Phys. **104**, 6755 (1996).

[48] D. J. Earl, J. Ilnytskyi and M. R. Wilson, Molec. Phys. **99**, 1719 (2001).

[49] K. M. Aoki and T. Akiyama, Molec. Cryst. Liq. Cryst. **262**, 543 (1995).

[50] K. M. Aoki and T. Akiyama, Mol. Sim. **16**, 99 (1996).

[51] K. M. Aoki and T. Akiyama, Molec. Cryst. Liq. Cryst. **299**, 45 (1997).

[52] M. J. Cook and M. R. Wilson, Molec. Cryst. Liq. Cryst. **357**, 127 (2001).

[53] M. J. Cook and M. R. Wilson, Molec. Cryst. Liq. Cryst. **363**, 181 (2001).

[54] D. L. Cheung, S. J. Clark and M. R. Wilson, Phys. Rev. E **65**, art. no. 051709 (2002).

[55] D. L. Cheung, S. J. Clark and M. R. Wilson, Chem. Phys. Lett. **356**, 140 (2002).

[56] J. P. Hansen and I. R. McDonald. *Theory of Simple Liquids*. Academic Press (1986).

[57] A. L. Onsager, NY Acad. Sci. **51**, 627 (1949).

[58] M. P. Allen and D. J. Tildesley. *Computer Simulation of Liquids*, chapter 1. Oxford University Press, Oxford (1987).

[59] E. de Miguel, L. F. Rull, M. K. Chalam and K. E. Gubbins, Molec. Phys. **74**, 405 (1991).

[60] R. Berardi, A. P. Emerson and C. Zannoni, J. Chem. Soc. Faraday Trans. **89**, 4069 (1993).

[61] A. Cuetos, J. M. Ilnytskyi and M. R. Wilson, Molec. Phys. **100**, 3839 (2002).

[62] K. Satoh, S. Mita and S. Kondo, Chem. Phys. Lett. **255**, 99 (1996).

[63] R. Berardi, S. Orlandi and C. Zannoni, Chem. Phys. Lett. **261**, 357 (1996).

[64] R. Berardi, S. Orlandi and C. Zannoni, Int. J. Mod. Phys. C **10**, 477 (1999).

[65] M. P. Neal and A. J. Parker, Molec. Cryst. Liq. Cryst. **330**, 1809 (1999).

[66] M. P. Neal and A. J. Parker, Chem. Phys. Lett. **294**, 277 (1998).

[67] A. P. J. Emerson, G. R. Luckhurst and S. G. Whatling, Molec. Phys. **82**, 113 (1994).

[68] R. Berardi and C. Zannoni, J. Chem. Phys. **113**, 5971 (2000).

[69] R. Memmer, H. G. Kuball and A. Schonhofer, Liq. Cryst. **15**, 345 (1993).

[70] M. A. Bates and G. R. Luckhurst. In M. Mingos, editor, *Structure and Bonding: Liquid Crystals*. Springer-Verlag, Heidelberg (1999).

[71] C. Zannoni, J. Mater. Chem. **11**, 2637 (2001).

[72] N. L. Allinger, Rev. Phys. Org. Chem. **13**, 1 (1976).

[73] O. Burkert and N. L. Allinger. *Molecular Mechanics, ACS Monograph 177*. American Chemical Society,Washington, DC. (1982).

[74] N. L. Allinger, M. T. Tribble, M. A. Miller and D. H. Wertz, J. Am. Chem. Soc. **93**, 1637 (1971).

[75] N. L. Allinger, J. Am. Chem. Soc. **99**, 8127 (1977).

[76] N. L. Allinger, Y. H. Yuh and J. Lii, J. Am. Chem. Soc. **111**, 8551 (1989).

[77] N. L. Allinger, K. S. Chen and J. H. Lii, J. Comput. Chem. **17**, 642 (1996).

[78] N. Nevins, K. S. Chen and N. L. Allinger, J. Comput. Chem. **17**, 669 (1996).

[79] S. J. Weiner, P. A. Kollman, D. A. Case, U. C. Singh, C. Ghio, G. Alagona, S. Profeta and P. Weiner, J. Am. Chem. Soc. **106**, 765 (1984).

[80] M. K. B. R. Gelin, Biochemistry **18**, 1256 (1979).

[81] B. R. Brooks, R. E. Bruccoleri, B. D. Olafson, , D. J. States, S. Swaminathan and M. Karplus, J. Comput. Chem. **4**, 187 (1983).

[82] W. L. Jorgensen, D. S. Maxwell and J. Tirado-Rives, J. Am. Chem. Soc. **118**, 11225 (1996).

[83] W. L. Jorgensen and N. A. McDonald, Theochem - J. Molec. Structure **424**, 145 (1998).

[84] W. D. Cornell, P. Cieplak, C. I. Bayly, I. R. Gould, K. M. M. Jr., D. M. Ferguson, D. C. Spellmeyer, T. Fox, J. W. Caldwell and P. A. Kollman, J. Am. Chem. Soc. **117**, 5179 (1995).

[85] G. Kaminski, E. M. Duffy and T. M. L. Jorgensen, J. Phys. Chem. **98**, 13077 (1994).

[86] N. L. Allinger and D. Y. Chung, J. Am. Chem. Soc. **98**, 6798 (1976).

[87] C. H. Langley, J. H. Lii and N. L. Allinger, J. Comp. Chem. **22**, 1476 (2001).

[88] Y. Kim, J. C. Corchado, J. Villa, J. Xing and D. G. Truhlar, J. Chem. Phys. **112**, 2718 (2000).

[89] N. Nevins, J. H. Lii and N. L. Allinger, J. Comput. Chem. **17**, 695 (1996).

[90] N. Nevins and N. L. Allinger, J. Comput. Chem. **17**, 730 (1996).

[91] N. L. Allinger, K. S. Chen and G. M. A. J. A. Katzenellenbogen, S. R. Wilson, J. Comput. Chem. **17**, 747 (1996).

[92] K. B. Wiberg, J. Am. Chem. Soc. **87**, 1070 (1965).

[93] R. H. Boyd, J. Chem. Phys. **49**, 2574 (1968).

[94] N. L. Allinger, Adv. Phys. Org. Chem. **13**, 1 (1976).

[95] N. Metropolis, A. W. Rosenbluth, M. N. Rosenbluth, A. H. Teller and E. Teller, J. Chem. Phys. **21**, 1087 (1953).

[96] D. Frenkel and B. Smit. *Understanding Molecular Simulations.* Academic Press (1996).

[97] L. Verlet, J. Phys. Chem. **159**, 98 (1967).

[98] W. Swope, H. C. Andersen, P. H. Berens and K. R. Wilson, J. Chem. Phys. **76**, 637 (1982).

[99] M. P. Allen and D. J. Tildesley. *Computer Simulation of Liquids*, chapter 5. Oxford University Press, Oxford (1987).

[100] M. P. Allen and D. J. Tildesley. *Computer Simulation of Liquids*, chapter 3. Oxford University Press, Oxford (1987).

[101] D. Beeman, J. Comp. Phys. **20**, 130 (1976).

[102] H. C. Andersen, J. Chem. Phys. **72**, 2384 (1980).

[103] S. Nosé, Molec. Phys. **52**, 255 (1984).

[104] W. G. Hoover, Phys. Rev. A **34**, 2499 (1986).

[105] H. J. C. Berendsen, J. P. M. Postma, W. F. VanGunsteren, A. DiNola and J. R. Haak, J. Chem. Phys. **81**, 3684 (1984).

[106] S. Toxvaerd, Phys. Rev. E **47**, 343 (1993).

[107] M. R. Wilson. In P. Pasini and C. Zannoni, editors, *Advances in the computer simulations of liquid crystals*, pages 389–415. Kluwer, The Netherlands (2000).

[108] P. Hilbers and K. Esselink. In M. P. Allen and D. J. Tildesley, editors, *Computer Simulations in Chemical Physics*, pages 473–493. Kluwer, The Netherlands (1992).

[109] J. Ilnytskyi and M. R. Wilson, Comp. Phys. Comm. **134**, 23 (2001).

[110] J. Ilnytskyi and M. R. Wilson, Comp. Phys. Comm. **148**, 43 (2002).

[111] Program GBMOL: A replicated data molecular dynamics program to simulate combinations of Gay-Berne and Lennard-Jones sites. Author: Mark R. Wilson, University of Durham, (1996).

[112] M. P. Allen and D. J. Tildesley. *Computer Simulation of Liquids*, chapter 2. Oxford University Press, Oxford (1987).

[113] M. P. Allen and M. R. Wilson, J. Computer-Aided Molec. Design **3**, 335 (1989).

[114] D. M. P. Mingos. *Structure and Bonding: Liquid Crystals*. Springer-Verlag, Berlin, Heidelberg (1999).

[115] J. Ilnytskyi and M. R. Wilson, J. Molec. Liq. **92**, 21 (2001).

[116] M. P. Allen and D. Frenkel, Phys. Rev. A **37**, 1813 (1988).

[117] M. P. Allen, M. A. Warren, M. R. Wilson, A. Sauron and W. Smith, J. Chem. Phys. **105**, 2850 (1996).

[118] M. R. Wilson, M. P. Allen, M. A. Warren, A. Sauron and W. Smith, J. Comput. Chem. **18**, 478 (1997).

[119] M. S. Al-Barwani and M. P. Allen, Phys. Rev. E **62**, 6706 (2000).

[120] W. G. Hoover, Phys. Rev. A **31**, 1695 (1985).

[121] D. Frenkel, H. N. W. Lekkerkerker and A. Stroobants, Nature **332**, 822 (1988).

[122] J. T. Brown, M. P. Allen, E. M. del Rio and E. de Miguel, Phys. Rev. E **57**, 6685 (1998).

[123] S. C. McGrother, A. Gil-Villegas and G. Jackson, J. Molec. Liq. **76**, 171 (1998).

[124] J. S. van Duijneveldt and M. P. Allen, Molec. Phys. **92**, 855 (1998).

[125] J. S. van Duijneveldt, A. Gil-Villegas and M. P. Allen, J. Chem. Phys. **112**, 9092 (2000).

[126] A. Cuetos, B. Martinez-Haya, L. F. Rull and S. Lago, J. Chem. Phys. **117**, 2934 (2002).

[127] A. Cuetos, B. Martinez-Haya, L. F. Rull and S. Lago, J. Chem. Phys. **117**, 11405 (2002).

[128] P. G. de Gennes and J. Prost. *The Physics of Liquid Crystals, 2nd edition*, chapter 6. Oxford University Press (1993).

[129] P. J. Camp, Molec. Phys. **91**, 381 (1997).

[130] M. P. Allen and A. Masters, Molec. Phys. **79**, 277 (1993).

[131] *For a detailed discussion see.* J. T. Brown. Ph.D. thesis, University of Bristol (1996).

[132] G. H. Grant and W. G. Richards. *Computational Chemistry*. Oxford University Press, Oxford (1995).

[133] R. W. Zwanzig, J. Chem. Phys. **22**, 1420 (1954).

[134] J. P. M. Postma, H. J. C. Berendsen and J. R. Haak, Faraday Symp. Chem. Soc. **83**, 55 (1982).

[135] B. L. Tembe and J. A. McCammon, J. Comput. Chem. **4**, 281 (1984).

[136] K. K. Mon and R. B. Griffiths, Phys. Rev. A **31**, 956 (1985).

[137] N. Lu and D. A. Kofke, J. Chem. Phys. **114**, 7303 (2001).

[138] K. S. Shing and K. E. Gubbins, Molec. Phys. **46**, 1109 (1982).

[139] C. H. Bennett, J. Comp. Phys. **22**, 245 (1976).

[140] W. L. Jorgensen and C. Ravimohan, J. Chem. Phys. **83**, 3050 (1985).

[141] S. Kumar, J. M. Rosenberg, D. Bouzbida, R. H. Swendsen and P. A. Kollman, J. Comput. Chem. **13**, 1011 (1992).

[142] S. Kumar, J. M. Rosenberg, D. Bouzbida, R. H. Swendsen and P. A. Kollman, J. Comput. Chem. **16**, 1339 (1995).

[143] W. F. van Gunsteren, X. Daura and A. E. Mark, Helv. Chim. Acta **85**, 3113 (2002).

[144] D. A. Kofke and P. T. Cummings, Molec. Phys. **92**, 973 (1997).

[145] W. L. Jorgensen, J. M. Briggs and M. L. Contreras, J. Phys. Chem. **94**, 1683 (1990).

[146] J. Alejandre, J. W. Emsley and D. J. Tildesley, J. Chem. Phys. **101**, 7027 (1994).

[147] D. J. Cleaver, C. M. Care, M. P. Allen and M. P. Neal, Phys. Rev. E **54**, 559 (1996).

[148] M. R. Wilson, J. Chem. Phys. **107**, 8654 (1997).

[149] C. McBride and M. R. Wilson, Molec. Phys. **97**, 511 (1999).

[150] F. J. Vesely, J. Comput. Phys. **47**, 291 (1982).

[151] M. R. Wilson, Liq. Cryst. **21**, 437 (1996).

[152] G. Gottarelli, G. P. Spada, R. Bartsch, G. Solladie and R. Zimmermann, J. Org. Chem. **51**, 589 (1986).

[153] A. di Matteo, S. M. Todd, G. Gottarelli, G. Solladie, V. E. Williams, R. P. Lemieux, A. Ferrarini and G. P. Spada, J. Am. Chem. Soc. **123**, 7842 (2001).

[154] A. Ferrarini, G. Gottarelli, P. L. Nordio and G. P. Spada, J. Chem. Soc. - Perkin Trans 2 page 411 (1999).

[155] A. Ferrarini and P. L. Nordio, J. Chem. Soc. - Perkin Trans 2 page 455 (1998).

[156] A. Ferrarini, P. L. Nordio, P. V. Shibaev and V. P. Shibaev, Liq. Cryst. **24**, 219 (1998).

[157] A. Rapini and M. Papoular, J. Phys. Colloq. **30 C4**, 54 (1969).

[158] P. G. de Gennes. *The Physics of Liquid Crystals*, chapter 3. Oxford University Press (1974).

[159] F. Brochard and P. G. de Gennes, J. Phys. **31**, 47 (1970).

[160] S. V. Burylov and Y. L. Raikher, Phys. Lett. A **149**, 279 (1990).

[161] *CAChe Satellite: A Chemists Guide to CAChe for Windows*. Oxford Molecular Group Inc. (1995).

[162] Y. Vorobjev and J. Hermans, Biophys. J. **73**, 722 (1997).

[163] *Maple 8: Mathematical computer program.* Waterloo Maple Inc. (2002).

[164] A. Ferrarini, (2002 personal communication).

[165] A. Ferrarini, F. Janssen, G. J. Moro and P. L. Nordio, Liq. Cryst. **26**, 201 (1999).

[166] G. Gottarelli, M. Hibert, B. Samori, G. Solladie, G. P. Spada and R. Zimmermann, J. Am. Chem. Soc. **105**, 7318 (1983).

[167] G. Gottarelli, G. Proni, G. P. Spada, D. Fabbri, S. Gladiali and C. Rosini, J. Org. Chem. **61**, 2013 (1996).

[168] H. J. Deussen, P. V. Shibaev, R. Vinokur, T. Bjornholm, K. Schaumberg, K. Bechgaard and V. P. Shibaev, Liq. Cryst. **21**, 327 (1996).

[169] H. Kamberaj, M. A. Osipov, R. J. Low and M. P. Neal, Molec. Phys. (2003 submitted).

[170] H. G. Kuball and T. Hofer. In H. S. Kitzerow and C. Bahr, editors, *Chirality in Liquid Crystals*, pages 67–100, Chapter 3. Springer-Verlag, New York (2001).

[171] H, B. Weiss, A. K. Beck and D. Seebach, Helvet. Chim. Acta **80**, 2507 (1997).

[172] D. SeebachH., A. K. Beck and A. Heckel, Angew. Chem. Int. Edit. **40**, 92 (2001).

[173] A. Ferrarini, G. R. Luckhurst, P. L. Nordio and S. J. Roskilly, Liq. Cryst. **21**, 373 (1996).

[174] C. McBride, M. R. Wilson and J. A. K. Howard, Molec. Phys. **93**, 955 (1998).

[175] M. R. Wilson and M. P. Allen, Molec. Cryst. Liq. Cryst. **198**, 465 (1991).

[176] A. Y. Bobrovsky, N. I. Boiko and V. P. Shibaev, Mol. Cryst. Liq. Cryst. **363**, 35 (2001).

[177] M. P. Neal, (2003 personal communication).

[178] A. J. Slaney, I. Nishiyama, P. Styring and J. W. Goodby, J. Mater. Chem. **2**, 805 (1992).

[179] M. J. Watson, M. K. Horsburgh, J. W. Goodby, K. Takatoh, A. J. Slaney, J. S. Patel and P. Styring, J. Mater. Chem. **8**, 1963 (1998).

[180] A. V. Emelyanenko, Phys. Rev. E **67**, art. no. 031704 (2003).

[181] A. V. Emelyanenko, M. A. Osipov and D. A. Dunmur, Phys. Rev. E **62**, 2340 (2000).

[182] M. P. Allen and A. Masters, J. Mater. Chem. **11**, 2678 (2001).

[183] G. Germano, (2002 personal communication).

Appendix A

Solutions and Chiral Measure Programs

A.1 Solutions

Determination of the helicity centre in the surface chirality model

The solution to find the vector from an arbitrary molecular origin to the helicity centre, $\mathbf{r}^{OH}$, from the following three simulataneous equations:

$$2(\mathbf{q}-\widetilde{\mathbf{q}})_{xy} = (r_y^{OH}t_{zy} - r_z^{OH}t_{yy}) + (t_{xz}r_x^{OH} - t_{xx}r_z^{OH}), \tag{A.1.1}$$

$$2(\mathbf{q}-\widetilde{\mathbf{q}})_{xz} = (r_y^{OH}t_{zz} - r_z^{OH}t_{yz}) + (t_{xx}r_y^{OH} - t_{xy}r_x^{OH}), \tag{A.1.2}$$

$$2(\mathbf{q}-\widetilde{\mathbf{q}})_{yz} = (r_z^{OH}t_{xz} - r_x^{OH}t_{zz}) + (t_{yx}r_y^{OH} - t_{yy}r_x^{OH}), \tag{A.1.3}$$

is given by:

$$
\begin{aligned}
r_x^{OH} \;=\; & -2\,(-t_{xz}t_{zz}(\mathbf{q}-\widetilde{\mathbf{q}})_{xy} + t_{zy}t_{xz}(\mathbf{q}-\widetilde{\mathbf{q}})_{xz} + t_{yx}t_{xx}(\mathbf{q}-\widetilde{\mathbf{q}})_{xz} \\
& -t_{yz}t_{yx}(\mathbf{q}-\widetilde{\mathbf{q}})_{xy} + t_{zy}t_{yz}(\mathbf{q}-\widetilde{\mathbf{q}})_{yz} - t_{zz}t_{xx}(\mathbf{q}-\widetilde{\mathbf{q}})_{yz} \\
& -t_{zz}t_{yy}(\mathbf{q}-\widetilde{\mathbf{q}})_{yz} - t_{xz}t_{xx}(\mathbf{q}-\widetilde{\mathbf{q}})_{xy} - t_{xx}^2(\mathbf{q}-\widetilde{\mathbf{q}})_{yz} \\
& -t_{xx}t_{yy}(\mathbf{q}-\widetilde{\mathbf{q}})_{yz} + t_{yx}t_{yy}(\mathbf{q}-\widetilde{\mathbf{q}})_{xz}) \\
\div\; & (t_{zy}t_{yz}t_{zz} + t_{xz}^2 t_{zz} - 2t_{zz}t_{xx}t_{yy} + t_{yx}t_{xx}t_{xy} + t_{yz}t_{yx}t_{xz} \\
& +t_{yx}t_{yy}t_{xy} + t_{zy}t_{xz}t_{xy} - t_{zz}t_{yy}^2 + t_{zy}t_{yz}t_{yy} - t_{zz}^2 t_{xx} \\
& +t_{xz}^2 t_{xx} - t_{xx}t_{yy}^2 - t_{xx}^2 t_{yy} - t_{xx}^2 t_{zz} - t_{zz}^2 t_{yy})\,,
\end{aligned}
\tag{A.1.4}
$$

$$
\begin{aligned}
r_y^{OH} \;=\; & -2\,(t_{yy}^2(\mathbf{q}-\widetilde{\mathbf{q}})_{xz} - t_{yy}(\mathbf{q}-\widetilde{\mathbf{q}})_{yz}t_{xy} + t_{yy}t_{zz}(\mathbf{q}-\widetilde{\mathbf{q}})_{xz} \\
& +t_{xx}t_{yy}(\mathbf{q}-\widetilde{\mathbf{q}})_{xz} - t_{xx}(\mathbf{q}-\widetilde{\mathbf{q}})_{yz}t_{xy} + t_{xx}t_{zz}(\mathbf{q}-\widetilde{\mathbf{q}})_{xz} \\
& -(\mathbf{q}-\widetilde{\mathbf{q}})_{xy}t_{yz}t_{zz} - (\mathbf{q}-\widetilde{\mathbf{q}})_{xy}t_{xz}t_{xy} - (\mathbf{q}-\widetilde{\mathbf{q}})_{xy}t_{yz}t_{yy} \\
& -t_{xz}t_{yz}(\mathbf{q}-\widetilde{\mathbf{q}})_{yz} - t_{xz}^2(\mathbf{q}-\widetilde{\mathbf{q}})_{xz}) \\
\div\; & (t_{zy}t_{yz}t_{zz} + t_{xz}^2 t_{zz} - 2t_{zz}t_{xx}t_{yy} + t_{yx}t_{xx}t_{xy} + t_{yz}t_{yx}t_{xz} \\
& +t_{yx}t_{yy}t_{xy} + t_{zy}t_{xz}t_{xy} - t_{zz}t_{yy}^2 + t_{zy}t_{yz}t_{yy} - t_{zz}^2 t_{xx} \\
& +t_{xz}^2 t_{xx} - t_{xx}t_{yy}^2 - t_{xx}^2 t_{yy} - t_{xx}^2 t_{zz} - t_{zz}^2 t_{yy})\,,
\end{aligned}
\tag{A.1.5}
$$

$$
\begin{aligned}
r_z^{OH} \;=\; & -2\,(t_{zy}t_{yy}(\mathbf{q}-\widetilde{\mathbf{q}})_{xz} - t_{zy}(\mathbf{q}-\widetilde{\mathbf{q}})_{yz}t_{xy} + t_{zy}t_{zz}(\mathbf{q}-\widetilde{\mathbf{q}})_{xz} \\
& -t_{xz}t_{zz}(\mathbf{q}-\widetilde{\mathbf{q}})_{yz} - t_{xz}t_{xx}(\mathbf{q}-\widetilde{\mathbf{q}})_{yz} + t_{xz}t_{yx}(\mathbf{q}-\widetilde{\mathbf{q}})_{xz} \\
& -t_{zz}^2(\mathbf{q}-\widetilde{\mathbf{q}})_{xy} - t_{yy}t_{xx}(\mathbf{q}-\widetilde{\mathbf{q}})_{xy} + t_{yx}(\mathbf{q}-\widetilde{\mathbf{q}})_{xy}t_{xy} \\
& -t_{zz}t_{xx}(\mathbf{q}-\widetilde{\mathbf{q}})_{xy} - t_{yy}t_{zz}(\mathbf{q}-\widetilde{\mathbf{q}})_{xy}) \\
\div\; & (t_{zy}t_{yz}t_{zz} + t_{xz}^2 t_{zz} - 2t_{zz}t_{xx}t_{yy} + t_{yx}t_{xx}t_{xy} + t_{yz}t_{yx}t_{xz} \\
& +t_{yx}t_{yy}t_{xy} + t_{zy}t_{xz}t_{xy} - t_{zz}t_{yy}^2 + t_{zy}t_{yz}t_{yy} - t_{zz}^2 t_{xx} \\
& +t_{xz}^2 t_{xx} - t_{xx}t_{yy}^2 - t_{xx}^2 t_{yy} - t_{xx}^2 t_{zz} - t_{zz}^2 t_{yy})\,,
\end{aligned}
\tag{A.1.6}
$$

where each of the terms is described in section 5.4.1.

A.2 Chiral Measure Programs

A.2.1 Chirality Order Parameter

The following is the FORTRAN90 code to calculate the value of the chirality order parameter, χ, for a molecule with n atoms where the co-ordinates of atom i are given by *x(i), y(i), z(i)*, and the van der Waals radius of atom i is given by *radius(i)*. The parameter *chirality* is the value of the chirality order parameter in $Å^3$.

```
!*********************************************************
subroutine tensorcalc(n,x,y,z,radius,chirality)
!*********************************************************

! subroutine to calculate the chirality order parameter
! D J Earl 2002
implicit none
integer i, j, n
character*80 filename
real*8 rx,ry,rz,chirality,chiralityalternate,chiralityTQT,chiralityTQTalternate
real*8 dotprod2,Tdeter,a,b,c
real*8,dimension(3,1000000):: dotcrd,dotnrm
real*8,dimension(1000000):: dotarea
real*8,dimension(3,3):: T,testQ,Tevec,littlet,Qa,QTevec,TinvQTevec,Tevc,Q
real*8,dimension(3,3)::
TQTevec,S,Qevec,STevec,TinvSTevec,TSTevec,TinvTTevec,TinvT
real*8,dimension(3,3):: TTevec,Tco,Tcotrans,Tinv,TinvTevec
real*8,dimension(3):: TQTeval,Seval,Qeval,cross_prod2,TSTeval
integer :: ndots,nrot,LDA
real*8 tmpS1,tmpS2,tmpS3,tmpQ1,tmpQ2,tmpQ3
real*8,dimension(2000) :: x,y,z
real*8,dimension(2000) :: radius
chirality = 0.0d0
! ** calculate molecular surface using SIMS subroutine
call surf_sims(n,x,y,z,radius,dotcrd,dotnrm,dotarea,ndots)
if(ndots.gt.100000)then
write(*,*)' ndots is greater than 100000'
stop
endif
! ** calculate T tensor
call calcT(ndots,dotnrm,dotarea,T,Tevec,littlet)
rx = 0.0d0
ry = 0.0d0
rz = 0.0d0
```

```
! ** calculate Q tensor
call calcQ1(ndots,dotnrm,dotcrd,dotarea,testQ,Tevec,rx,ry,rz,Qa)
! ** calculate rx,ry,rz (vector from origin to helicity centre)
call calcr(littlet,rx,ry,rz,Qa)
! ** calculate Q tensor
call calcQ2(ndots,dotnrm,dotcrd,dotarea,Q,Tevec,rx,ry,rz,Qa,Qeval,Qevec)
cross_prod2(1)=(Qevec(2,1)*Qevec(3,3))-(Qevec(3,1)*Qevec(2,3))
cross_prod2(2)=-((Qevec(1,1)*Qevec(3,3))-(Qevec(3,1)*Qevec(1,3)))
cross_prod2(3)=(Qevec(1,1)*Qevec(2,3))-(Qevec(2,1)*Qevec(1,3))
dotprod2=(cross_prod2(1)*Qevec(1,2))+(cross_prod2(2)*Qevec(2,2))+ &
(cross_prod2(3)*Qevec(3,2))
QTevec(1,1)=Q(1,1)*Tevec(1,1)+Q(1,2)*Tevec(2,1)+Q(1,3)*Tevec(3,1)
QTevec(1,2)=Q(1,1)*Tevec(1,2)+Q(1,2)*Tevec(2,2)+Q(1,3)*Tevec(3,2)
QTevec(1,3)=Q(1,1)*Tevec(1,3)+Q(1,2)*Tevec(2,3)+Q(1,3)*Tevec(3,3)
QTevec(2,1)=Q(2,1)*Tevec(1,1)+Q(2,2)*Tevec(2,1)+Q(2,3)*Tevec(3,1)
QTevec(2,2)=Q(2,1)*Tevec(1,2)+Q(2,2)*Tevec(2,2)+Q(2,3)*Tevec(3,2)
QTevec(2,3)=Q(2,1)*Tevec(1,3)+Q(2,2)*Tevec(2,3)+Q(2,3)*Tevec(3,3)
QTevec(3,1)=Q(3,1)*Tevec(1,1)+Q(3,2)*Tevec(2,1)+Q(3,3)*Tevec(3,1)
QTevec(3,2)=Q(3,1)*Tevec(1,2)+Q(3,2)*Tevec(2,2)+Q(3,3)*Tevec(3,2)
QTevec(3,3)=Q(3,1)*Tevec(1,3)+Q(3,2)*Tevec(2,3)+Q(3,3)*Tevec(3,3)
TinvQTevec(1,1)=Tinv(1,1)*QTevec(1,1)+Tinv(1,2)*QTevec(2,1)+Tinv(1,3)*QTevec(3,1)
TinvQTevec(1,2)=Tinv(1,1)*QTevec(1,2)+Tinv(1,2)*QTevec(2,2)+Tinv(1,3)*QTevec(3,2)
TinvQTevec(1,3)=Tinv(1,1)*QTevec(1,3)+Tinv(1,2)*QTevec(2,3)+Tinv(1,3)*QTevec(3,3)
TinvQTevec(2,1)=Tinv(2,1)*QTevec(1,1)+Tinv(2,2)*QTevec(2,1)+Tinv(2,3)*QTevec(3,1)
TinvQTevec(2,2)=Tinv(2,1)*QTevec(1,2)+Tinv(2,2)*QTevec(2,2)+Tinv(2,3)*QTevec(3,2)
TinvQTevec(2,3)=Tinv(2,1)*QTevec(1,3)+Tinv(2,2)*QTevec(2,3)+Tinv(2,3)*QTevec(3,3)
TinvQTevec(3,1)=Tinv(3,1)*QTevec(1,1)+Tinv(3,2)*QTevec(2,1)+Tinv(3,3)*QTevec(3,1)
TinvQTevec(3,2)=Tinv(3,1)*QTevec(1,2)+Tinv(3,2)*QTevec(2,2)+Tinv(3,3)*QTevec(3,2)
TinvQTevec(3,3)=Tinv(3,1)*QTevec(1,3)+Tinv(3,2)*QTevec(2,3)+Tinv(3,3)*QTevec(3,3)

! calculate the ordering matrix S
call scalc(T,S,Seval,ndots,dotnrm,dotarea)
STevec(1,1)=S(1,1)*Tevec(1,1)+S(1,2)*Tevec(2,1)+S(1,3)*Tevec(3,1)
STevec(1,2)=S(1,1)*Tevec(1,2)+S(1,2)*Tevec(2,2)+S(1,3)*Tevec(3,2)
STevec(1,3)=S(1,1)*Tevec(1,3)+S(1,2)*Tevec(2,3)+S(1,3)*Tevec(3,3)
STevec(2,1)=S(2,1)*Tevec(1,1)+S(2,2)*Tevec(2,1)+S(2,3)*Tevec(3,1)
STevec(2,2)=S(2,1)*Tevec(1,2)+S(2,2)*Tevec(2,2)+S(2,3)*Tevec(3,2)
STevec(2,3)=S(2,1)*Tevec(1,3)+S(2,2)*Tevec(2,3)+S(2,3)*Tevec(3,3)
STevec(3,1)=S(3,1)*Tevec(1,1)+S(3,2)*Tevec(2,1)+S(3,3)*Tevec(3,1)
STevec(3,2)=S(3,1)*Tevec(1,2)+S(3,2)*Tevec(2,2)+S(3,3)*Tevec(3,2)
STevec(3,3)=S(3,1)*Tevec(1,3)+S(3,2)*Tevec(2,3)+S(3,3)*Tevec(3,3)
TinvSTevec(1,1)=Tinv(1,1)*STevec(1,1)+Tinv(1,2)*STevec(2,1)+Tinv(1,3)*STevec(3,1)
TinvSTevec(1,2)=Tinv(1,1)*STevec(1,2)+Tinv(1,2)*STevec(2,2)+Tinv(1,3)*STevec(3,2)
TinvSTevec(1,3)=Tinv(1,1)*STevec(1,3)+Tinv(1,2)*STevec(2,3)+Tinv(1,3)*STevec(3,3)
TinvSTevec(2,1)=Tinv(2,1)*STevec(1,1)+Tinv(2,2)*STevec(2,1)+Tinv(2,3)*STevec(3,1)
TinvSTevec(2,2)=Tinv(2,1)*STevec(1,2)+Tinv(2,2)*STevec(2,2)+Tinv(2,3)*STevec(3,2)
TinvSTevec(2,3)=Tinv(2,1)*STevec(1,3)+Tinv(2,2)*STevec(2,3)+Tinv(2,3)*STevec(3,3)
```

```
TinvSTevec(3,1)=Tinv(3,1)*STevec(1,1)+Tinv(3,2)*STevec(2,1)+Tinv(3,3)*STevec(3,1)
TinvSTevec(3,2)=Tinv(3,1)*STevec(1,2)+Tinv(3,2)*STevec(2,2)+Tinv(3,3)*STevec(3,2)
TinvSTevec(3,3)=Tinv(3,1)*STevec(1,3)+Tinv(3,2)*STevec(2,3)+Tinv(3,3)*STevec(3,3)
chirality=-((2.0d0/3.0d0)**0.5d0)*(TinvSTevec(1,1)*TinvQTevec(1,1)+ &
TinvSTevec(2,2)*TinvQTevec(2,2)+TinvSTevec(3,3)*TinvQTevec(3,3))
return
end

!**********************************************************************
subroutine calcT(ndots,dotnrm,dotarea,T,Tevec,littlet)
!**********************************************************************
implicit none
!** routine to calculate tensor T **
!** local variables
integer i,j,k
real*8 rt6inv,sum,kron,areasum,store,dotprod,dotprod2,size,sumt,size2
real*8,dimension(3,100000):: dotnrm
real*8,dimension(100000):: dotarea
real*8,dimension(3,3):: T, Tevec, littlet,newT
real*8,dimension(3):: Teval, cross_prod, store_vec, cross_prod2
integer :: ndots,option,nrot
!** open output file **
rt6inv = 1.0d0/(6.0d0)**0.5d0
do i=1,3
do j=1,3
T(i,j)=0.0d0
littlet(i,j)=0.0d0
if(i.eq.j)then
kron=1.0d0
else kron=0.0d0
endif
sum = 0.0d0
sumt = 0.0d0
do k=1,ndots
sum = sum + (((3.0d0*dotnrm(i,k)*dotnrm(j,k))-kron)*dotarea(k))
sumt = sumt + ((dotnrm(i,k)*dotnrm(j,k))*dotarea(k))
enddo
T(i,j)=-sum*rt6inv
littlet(i,j)=-sumt
newT(i,j)=T(i,j)
enddo
enddo
!diagonalize matrix
call jacobi(newT,3,3,Teval,Tevec,nrot)
!cross xx with yy eigenvect and dot with zz to see whether RH or LH
!and ensure that it is always RH
cross_prod(1)=(Tevec(2,1)*Tevec(3,2))-(Tevec(3,1)*Tevec(2,2))
```

```
cross_prod(2)=-((Tevec(1,1)*Tevec(3,2))-(Tevec(3,1)*Tevec(1,2)))
cross_prod(3)=(Tevec(1,1)*Tevec(2,2))-(Tevec(2,1)*Tevec(1,2))
size=(cross_prod(1)**2.0d0+cross_prod(2)**2.0d0+cross_prod(3)**2.0d0)**0.5d0
cross_prod2(1)=(Tevec(1,2)*Tevec(3,3))-(Tevec(1,3)*Tevec(3,2))
cross_prod2(2)=-((Tevec(1,1)*Tevec(3,3))-(Tevec(1,3)*Tevec(3,1)))
cross_prod2(3)=(Tevec(1,1)*Tevec(3,2))-(Tevec(1,2)*Tevec(3,1))
size=(cross_prod(1)**2.0d0+cross_prod(2)**2.0d0+cross_prod(3)**2.0d0)**0.5d0
size2=(cross_prod2(1)**2.0d0+cross_prod2(2)**2.0d0+cross_prod2(3)**2.0d0)**0.5d0
dotprod=(cross_prod(1)*Tevec(1,3))+(cross_prod(2)*Tevec(2,3))+ &
(cross_prod(3)*Tevec(3,3))
dotprod2=(cross_prod2(1)*Tevec(2,1))+(cross_prod2(2)*Tevec(2,2))+ &
(cross_prod2(3)*Tevec(2,3))
return
end

!**********************************************************************
subroutine calcQ1(ndots,dotnrm,dotcrd,dotarea,testQ,Tevec,rx,ry,rz,Qa)
!**********************************************************************
implicit none
!** routine to calculate tensor T **
!** local variables
integer i,j,k
real*8 rt3o8,sumq1,sumq2,kron,areasum,store,dotprod,size
real*8 rx,ry,rz
real*8,dimension(3,100000):: dotnrm,dotcrd,scrossr,rcrosss,dotcrdnew
real*8,dimension(100000):: dotarea
real*8,dimension(3,3):: testQ,Qs,Qa,Qevec,littleqsquiggle,littleq
real*8,dimension(3,3):: test,Tevec,Qnew
real*8,dimension(3):: Qeval, cross_prod, store_vec
integer :: ndots,nrot
rt3o8=(3.0d0/8.0d0)**0.5d0
!subroutine to calculate the helicity tensor, Q
!calc. (s x r) terms
do i=1,ndots
scrossr(1,i)=(dotnrm(2,i)*dotcrd(3,i))-(dotnrm(3,i)*dotcrd(2,i))
scrossr(2,i)=-((dotnrm(1,i)*dotcrd(3,i))-(dotnrm(3,i)*dotcrd(1,i)))
scrossr(3,i)=(dotnrm(1,i)*dotcrd(2,i))-(dotnrm(2,i)*dotcrd(1,i))
enddo
!calc. (r x s) terms
do i=1,ndots
rcrosss(1,i)=(dotcrd(2,i)*dotnrm(3,i))-(dotcrd(3,i)*dotnrm(2,i))
rcrosss(2,i)=-((dotcrd(1,i)*dotnrm(3,i))-(dotcrd(3,i)*dotnrm(1,i)))
rcrosss(3,i)=(dotcrd(1,i)*dotnrm(2,i))-(dotcrd(2,i)*dotnrm(1,i))
enddo
!calc. integral of ((s x (s x r) + (s x r) x s)dS)
do i=1,3
do j=1,3
```

```
testQ(i,j)=0.0d0
Qs(i,j)=0.0d0
Qa(i,j)=0.0d0
littleq(i,j)=0.0d0
littleqsquiggle(i,j)=0.0d0
sumq1 = 0.0d0
sumq2 = 0.0d0
do k=1,ndots
sumq1 = sumq1 - ((rcrosss(i,k)*dotnrm(j,k)*dotarea(k)))
sumq2 = sumq2 + ((dotnrm(i,k)*scrossr(j,k)*dotarea(k)))
enddo
littleq(i,j)=sumq1 littleqsquiggle(i,j)=sumq2
Qs(i,j)=(sumq1+sumq2)/2.0d0
Qa(i,j)=(sumq1-sumq2)/2.0d0
testQ(i,j)=Qs(i,j)*rt3o8*2.0d0
Qnew(i,j)=testQ(i,j)
enddo
enddo
!diagonalize matrix
call jacobi(Qnew,3,3,Qeval,Qevec,nrot)
return
end

!**********************************************************************
subroutine calcr(t,rx,ry,rz,q)
!**********************************************************************
implicit none
real*8,dimension(3,3):: t,q
real*8 rx,ry,rz,xx,xy,xz,yx,yy,yz,zx,zy,zz,qxx,qxy,qxz,qyx,qyy,qyz,qzx,qzy,qzz
xx=t(1,1)
xy=t(1,2)
xz=t(1,3)
yx=t(2,1)
yy=t(2,2)
yz=t(2,3)
zx=t(3,1)
zy=t(3,2)
zz=t(3,3)
qxx=q(1,1)
qxy=q(1,2)
qxz=q(1,3)
qyx=q(2,1)
qyy=q(2,2)
qyz=q(2,3)
qzx=q(3,1)
qzy=q(3,2)
qzz=q(3,3)
```

```
rx=-2.0d0*(-xz*zz*qxy+zy*xz*qxz+yx*xx*qxz-yz*yx*qxy+zy*yz*qyz-zz*xx*qyz-
zz*yy*qyz-xz*xx*qxy-xx**2.0d0*qyz-
xx*yy*qyz+yx*yy*qxz)/(zy*yz*zz+xz**2.0d0*zz-
2.0d0*zz*xx*yy+yx*xx*xy+yz*yx*xz+yx*yy*xy+zy*xz*xy-
zz*yy**2.0d0+zy*yz*yy-zz**2.0d0*xx+xz**2.0d0*xx-xx &
*yy**2.0d0-xx**2.0d0*yy-xx**2.0d0*zz-zz**2.0d0*yy)

rz=-2.0d0*(zy*yy*qxz-zy*qyz*xy+zy*zz*qxz-xz*zz*qyz-xz*xx*qyz+xz*yx*qxz-
zz**2.0d0*qxy-yy*xx*qxy+yx*qxy*xy-zz*xx*qxy-
yy*zz*qxy)/(zy*yz*zz+xz**2.0d0*zz-
2.0d0*zz*xx*yy+yx*xx*xy+yz*yx*xz+yx*yy*xy+zy*xz*xy-
zz*yy**2.0d0+zy*yz*yy-zz**2.0d0*xx+xz**2.0d0*xx-xx*yy**2.0d0-xx**2.0d0*yy-
xx**2.0d0*zz-zz**2.0d0*yy)

ry=-2.0d0*(yy**2.0d0*qxz-yy*qyz*xy+yy*zz*qxz+xx*yy*qxz-
xx*qyz*xy+xx*zz*qxz-qxy*yz*zz-qxy*xz*xy-qxy*yz*yy-xz*yz*qyz-
xz**2.0d0*qxz)/(zy*yz*zz+xz**2.0d0*zz-
2.0d0*zz*xx*yy+yx*xx*xy+yz*yx*xz+yx*yy*xy+zy*xz*xy-
zz*yy**2.0d0+zy*yz*yy-zz**2.0d0*xx+xz**2.0d0*xx-xx*yy**2.0d0-xx**2.0d0*yy-
xx**2.0d0*zz-zz**2.0d0*yy)

return
end

!*****************************************************************
subroutine
calcQ2(ndots,dotnrm,dotcrd,dotarea,testQ,Tevec,rx,ry,rz,Qa,Qeval,Qevec)
!*****************************************************************
implicit none
!** routine to calculate tensor T **
!** local variables
integer i,j,k
real*8 rt3o8,sumq1,sumq2,kron,areasum,store,dotprod,size
real*8 rx,ry,rz
real*8,dimension(3,100000):: dotnrm,dotcrd,scrossr,rcrosss,dotcrdnew
real*8,dimension(100000):: dotarea
real*8,dimension(3,3):: testQ,Qs,Qa,Qevec,littleqsquiggle,littleq
real*8,dimension(3,3):: test,Tevec,Qnew
real*8,dimension(3):: Qeval, cross_prod, store_vec
integer :: ndots,nrot
rt3o8=(3.0d0/8.0d0)**0.5d0
do i=1,ndots
dotcrd(1,i)=dotcrd(1,i)-rx
dotcrd(2,i)=dotcrd(2,i)-ry
dotcrd(3,i)=dotcrd(3,i)-rz
enddo
!calc. (s x r) terms
```

```
do i=1,ndots
scrossr(1,i)=(dotnrm(2,i)*dotcrd(3,i))-(dotnrm(3,i)*dotcrd(2,i))
scrossr(2,i)=-((dotnrm(1,i)*dotcrd(3,i))-(dotnrm(3,i)*dotcrd(1,i)))
scrossr(3,i)=(dotnrm(1,i)*dotcrd(2,i))-(dotnrm(2,i)*dotcrd(1,i))
enddo
!calc. (r x s) terms
do i=1,ndots
rcrosss(1,i)=(dotcrd(2,i)*dotnrm(3,i))-(dotcrd(3,i)*dotnrm(2,i))
rcrosss(2,i)=-((dotcrd(1,i)*dotnrm(3,i))-(dotcrd(3,i)*dotnrm(1,i)))
rcrosss(3,i)=(dotcrd(1,i)*dotnrm(2,i))-(dotcrd(2,i)*dotnrm(1,i))
enddo
!calc. integral of ((s x (s x r) + (s x r) x s)dS)
do i=1,3
do j=1,3
testQ(i,j)=0.0d0
Qs(i,j)=0.0d0
Qa(i,j)=0.0d0
littleq(i,j)=0.0d0
littleqsquiggle(i,j)=0.0d0
sumq1 = 0.0d0
sumq2 = 0.0d0
do k=1,ndots
sumq1 = sumq1 - ((rcrosss(i,k)*dotnrm(j,k)*dotarea(k)))
sumq2 = sumq2 + ((dotnrm(i,k)*scrossr(j,k)*dotarea(k)))
enddo
littleq(i,j)=sumq1
littleqsquiggle(i,j)=sumq2
Qs(i,j)=(sumq1+sumq2)/2.0d0
Qa(i,j)=(sumq1-sumq2)/2.0d0
testQ(i,j)=Qs(i,j)*rt3o8*2.0d0
Qnew(i,j)=testQ(i,j)
enddo
enddo
!diagonalize matrix
call jacobi(Qnew,3,3,Qeval,Qevec,nrot)
return
end

!*********************************************************
subroutine scalc(T,S,Seval,ndots,dotnrm_orig,dotarea)
!*********************************************************
IMPLICIT NONE
real*8,dimension(3,100000):: dotnrm,dotnrm_orig
real*8,dimension(100000):: dotarea
real*8,dimension(3,3) :: T, Tnew, S, nominatorsum, Sevec,rotate,Snew
real*8,dimension(3) :: Seval,theta,lz,molx,moly,molz,Tnewlz,cross_prod2
real*8 beta,gamma,magmol,maglab,epsilon,rt6over3,diff,expusum,lzTnewlz
```

```
real*8 negu,expu,delta,molx1sum,molx2sum,molx3sum,dotprod2
integer i,j,k,l,points,ndots,nrot
! lz is the cosine of the angle between the laboratory z and molecular axes
! rot is matrix to rotate axis by Euler angles beta and gamma
! points is the number of points from 0 to 360 degrees for beta and gamma
! that we wish to use to calculate S, the ordering matrix
! molecular axes set to lab. axes for alpha=beta=gamma=0
maglab = 1.0d0
rt6over3 = (6.0d0**0.5d0)/3.0d0
Tnew(:,:) = T(:,:) * rt6over3
epsilon = 0.05 !units of this are per square Angstrom
expusum= 0.0d0
molx1sum=0.0d0
molx2sum=0.0d0
molx3sum=0.0d0
do i=1,3
do j=1,3
nominatorsum(i,j)=0.0d0
enddo
enddo
points = 1000
diff = 2*3.141592654d0/dble(points)
do i=1,points
beta=0.0d0
beta = diff * dble(i)
do j=1,points
gamma=0.0d0
gamma = diff * dble(j)
lzTnewlz=0.0d0
do k=1,3
Tnewlz(k)=0.0d0
do l=1,3
rotate(k,l)=0.0d0
enddo
enddo
rotate(1,1)=(cos(gamma))*cos(beta) rotate(1,2)=sin(gamma)
rotate(1,3)=-(cos(gamma))*sin(beta) rotate(2,1)=-(sin(gamma))*cos(beta)
rotate(2,2)=cos(gamma) rotate(2,3)=(sin(gamma))*sin(beta)
rotate(3,1)=sin(beta) rotate(3,2)=0.0d0 rotate(3,3)=cos(beta)
molx(1)=1.0d0*rotate(1,1) molx(2)=1.0d0*rotate(1,2) molx(3)=1.0d0*rotate(1,3)
moly(1)=1.0d0*rotate(2,1) moly(2)=1.0d0*rotate(2,2) moly(3)=1.0d0*rotate(2,3)
molz(1)=1.0d0*rotate(3,1) molz(2)=1.0d0*rotate(3,2) molz(3)=1.0d0*rotate(3,3)
! calculate cos of angles between lab. z and molecular axes
! as magnitude of lab. and mol. axes vectors are both 1 then just do dot prod
! lz(1) is the cos of angle between the lab. z and molecular x axis
lz(1)=1.0d0*molx(3)
```

```
!as lab z axis = (0,0,1)
lz(2)=1.0d0*moly(3)
lz(3)=1.0d0*molz(3)
! now multiply Tnew with lz
Tnewlz(1)=Tnew(1,1)*lz(1)+Tnew(1,2)*lz(2)+Tnew(1,3)*lz(3)
Tnewlz(2)=Tnew(2,1)*lz(1)+Tnew(2,2)*lz(2)+Tnew(2,3)*lz(3)
Tnewlz(3)=Tnew(3,1)*lz(1)+Tnew(3,2)*lz(2)+Tnew(3,3)*lz(3)
! multiply lz with Tnewlz
lzTnewlz = lz(1)*Tnewlz(1) + lz(2)*Tnewlz(2) + lz(3)*Tnewlz(3)
negu = epsilon*1.5d0*lzTnewlz
expu = exp(negu)
expusum = expusum + expu
do k=1,3
do l=1,3
if(k.eq.l)then
delta=1.0d0
else delta=0.0d0
endif
nominatorsum(k,l) = nominatorsum(k,l) + ((3.0d0*lz(k)*lz(l)-delta)*expu)
enddo
enddo
enddo
enddo
S(:,:) = nominatorsum(:,:) / (2.0d0*expusum)
Snew(:,:)=S(:,:)
call jacobi(Snew,3,3,Seval,Sevec,nrot)
return
end

!*********************************
SUBROUTINE jacobi(a,n,np,d,v,nrot)
!*********************************
!program from numerical recipes to diagonalize a matrix
INTEGER n,np,nrot,NMAX
REAL*8 a(np,np),d(np),v(np,np)
PARAMETER (NMAX=500)
INTEGER i,ip,iq,j
REAL*8 c,g,h,s,sm,t,tau,theta,tresh,b(NMAX),z(NMAX)
do ip=1,n
do iq=1,n
v(ip,iq)=0.
enddo
v(ip,ip)=1.
enddo
do ip=1,n
b(ip)=a(ip,ip)
d(ip)=b(ip)
```

```
z(ip)=0.
enddo
nrot=0
do i=1,50
sm=0.
do ip=1,n-1
do iq=ip+1,n
sm=sm+abs(a(ip,iq))
enddo
enddo
if(sm.eq.0.)return
if(i.lt.4)then
tresh=0.2*sm/n**2 else tresh=0.
endif
do ip=1,n-1
do iq=ip+1,n
g=100.*abs(a(ip,iq))
if((i.gt.4).and.(abs(d(ip))+g.eq.abs(d(ip)))&
.and.(abs(d(iq))+g.eq.abs(d(iq))))then
a(ip,iq)=0.
else if(abs(a(ip,iq)).gt.tresh)then
h=d(iq)-d(ip)
if(abs(h)+g.eq.abs(h))then
t=a(ip,iq)/h t = 1/(2 )
else
theta=0.5*h/a(ip,iq)
t=1./(abs(theta)+sqrt(1.+theta**2))
if(theta.lt.0.)t=-t
endif
c=1./sqrt(1+t**2)
s=t*c tau=s/(1.+c)
h=t*a(ip,iq)
z(ip)=z(ip)-h
z(iq)=z(iq)+h
d(ip)=d(ip)-h
d(iq)=d(iq)+h
a(ip,iq)=0.
do j=1,ip-1
g=a(j,ip)
h=a(j,iq)
a(j,ip)=g-s*(h+g*tau)
a(j,iq)=h+s*(g-h*tau)
enddo
do j=ip+1,iq-1
g=a(ip,j)
h=a(j,iq)
```

```
a(ip,j)=g-s*(h+g*tau)
a(j,iq)=h+s*(g-h*tau)
enddo
do j=iq+1,n
g=a(ip,j)h=a(iq,j)
a(ip,j)=g-s*(h+g*tau)
a(iq,j)=h+s*(g-h*tau)
enddo
do j=1,n
g=v(j,ip)
h=v(j,iq)
v(j,ip)=g-s*(h+g*tau)
v(j,iq)=h+s*(g-h*tau)
enddo
nrot=nrot+1
endif
enddo
enddo
do ip=1,n
b(ip)=b(ip)+z(ip)
d(ip)=b(ip)
z(ip)=0.
enddo
enddo
pause 'too many iterations in jacobi'
return
END
```

A.2.2 Scaled Chiral Index

The following is the FORTRAN90 code to calculate the value of the scaled chiral index, G_{0S}, for a molecule with n atoms where the co-ordinates of atom i are given by *x(i), y(i), z(i).*

```
!*************************************************
subroutine ch_ten(x,y,z,n,g0s_w,tensor)
!*************************************************
implicit none
!program to calculate the Osipov based chirality tensor for a
!molecule given an input pdb file
!David Earl 2001
integer n, i, j, k, l, m
real*8 x(*), y(*), z(*), nreal
```

```
real*8,dimension(5000):: w, tensor
real*8,dimension(3):: vect_ij, vect_kl, vect_il, vect_jk, cross
real*8 dot1, dot2, dot3, r_ij, r_kl, r_il, r_jk
real*8 denom, numer1, sum1
real*8 g0s_w, count real*8 chiral1
g0s_w=0.0d0
sum1=0.0d0 count=0.0d0
nreal=dble(n)
if (n.gt.5000)then
write(*,*)'ch_ten error - n is too big'
stop
endif
do i=1,n
tensor(i)=0.0d0
w(i)=1.0d0 enddo
!loop for calculating tensor
do i=1,n
do j=1,n
do k=1,n
do l=1,n
if(i.ne.j.and.i.ne.k.and.i.ne.l.and.j.ne.k.and.j.ne.l &.and.k.ne.l)then
vect_ij(1)=x(i)-x(j)
vect_ij(2)=y(i)-y(j)
vect_ij(3)=z(i)-z(j)
r_ij=sqrt((vect_ij(1)*vect_ij(1))+(vect_ij(2)*vect_ij(2))+ &
(vect_ij(3)*vect_ij(3)))
!write(*,*)r_ij
vect_kl(1)=x(k)-x(l)
vect_kl(2)=y(k)-y(l)
vect_kl(3)=z(k)-z(l)
r_kl=sqrt((vect_kl(1)*vect_kl(1))+(vect_kl(2)*vect_kl(2))+ &
(vect_kl(3)*vect_kl(3)))
!write(*,*)r_kl
vect_il(1)=x(i)-x(l)
vect_il(2)=y(i)-y(l)
vect_il(3)=z(i)-z(l)
r_il=sqrt((vect_il(1)*vect_il(1))+(vect_il(2)*vect_il(2))+ &
(vect_il(3)*vect_il(3)))
!write(*,*)r_il
vect_jk(1)=x(j)-x(k)
vect_jk(2)=y(j)-y(k)
vect_jk(3)=z(j)-z(k)
r_jk=sqrt((vect_jk(1)*vect_jk(1))+(vect_jk(2)*vect_jk(2))+ &
(vect_jk(3)*vect_jk(3)))
!write(*,*)r_jk
!do the cross products and the scalar products
```

```
cross(1)=(vect_ij(2)*vect_kl(3))-(vect_ij(3)*vect_kl(2))
cross(2)=(vect_ij(3)*vect_kl(1))-(vect_ij(1)*vect_kl(3))
cross(3)=(vect_ij(1)*vect_kl(2))-(vect_ij(2)*vect_kl(1))
!write(*,*)cross
dot1=dot_product(cross,vect_il)
dot2=dot_product(vect_ij,vect_jk)
dot3=dot_product(vect_jk,vect_kl)
!work out numerator term in sum
numer1=w(i)*w(j)*w(k)*w(l)*dot1*dot2*dot3
!write(*,*)numer1
!work out denominator term in sum
denom=((r_ij*r_jk*r_kl)**2.0d0)*r_il
denom = 1.0d0 / denom
!write(*,*)denom
chiral1 = numer1 * denom
!do the sum!
sum1=sum1+chiral1
count=count+1.0d0
tensor(i)=tensor(i)+chiral1
tensor(j)=tensor(j)+chiral1
tensor(k)=tensor(k)+chiral1
tensor(l)=tensor(l)+chiral1
else
continue
endif
enddo
enddo
enddo
enddo
g0s_w=(8.0d0*sum1)/(nreal*nreal*nreal*nreal)
!write(*,*)' g0s_w = ',g0s_w
!write(*,*)' count=',count
!do i=1,n
!write(11,*)' tensor(',i,')= ',tensor(i)
!enddo
return
end
```

Appendix B

Conferences, Presentations, Courses, Seminars and Publications

B.1 Conferences and Presentations

British Liquid Crystal Society Annual Conference

University of Oxford, UK, 19th-21st March, 2001

Work presented in poster format.

7th Merck CASE Conference

Southampton, UK, 23rd-24th April, 2001

Work presented in poster format.

Materials Discussion 4: Molecular Topology in Liquid Crystals

Grasmere, UK, 11th-14th September, 2001

Work presented as a discussion paper (see J. Mater. Chem. **11**, 2672 (2001)).

CCP5 Annual Conference: Liquids and Liquid Interfaces

Warwick University, UK, 16th-19th September, 2001

Work presented in poster format.

British Liquid Crystal Society Winter Workshop

Hull University, UK, 16th-18th December, 2001

8th Merck CASE Conference

Southampton, UK, 8th-9th April, 2002

Work presented in a talk.

International Liquid Crystal Conference

Edinburgh, UK, 30th June-5th July, 2002

Work presented in poster format.

CCP5 Summer School on Molecular Simulation

King's College London, UK, 8th-16th July, 2002

Work presented in poster format.

CCP5 Annual Conference: Advances in Simulations of Molecules and Materials

Durham University, UK, 9th-12th September, 2002

Work presented in poster format.

5th Liquid Matter Conference

Konstanz, Germany, 14th-18th September, 2002

Work presented in poster format.

British Liquid Crystal Society Annual Conference

Cambridge University, UK, 7th-9th April, 2003

Work presented in a talk.

Invited Talk at FOM Institute for Atomic and Molecular Physics (AMOLF)

Amsterdam, Netherlands, 10th April, 2003

Work presented in a talk.

New Challenges in Computational Chemistry

Imperial College, London, UK, 11th April, 2003

Work presented in poster format.

Young Material Modeller's Forum

Daresbury Laboratory, UK, 15th May, 2003

International School of Liquid Crystals 10th Workshop: Computational Methods for Polymers and Liquid Crystalline Polymers

Erice, Sicily, Italy, 16th-22nd July, 2003

Work presented in poster format.

B.2 Courses

Numerical Methods and Data Analysis

Department of Chemistry, Durham University (2001)

Practical Electronic Structure Calculations

Department of Chemistry, Durham University (2001)

Experimental Design

Department of Chemistry, Durham University (2001)

Diffraction and Scattering Methods

Department of Chemistry, Durham University (2001)

Introduction to UNIX

Information Technology Service, Durham University (2001)

FORTRAN Programming

Information Technology Service, Durham University (2001)

B.3 Seminars

11 October 2000: **Recent Developments in Organic LED Technology: Organolanthanide Phosphors**

Speaker: Dr. V. Christou

1 November 2000: **Label-free Detection of Interfacial Chemistry in Scanning Microprobe and Biosensor Formats**

Speaker: Professor M. Thompson

8 November 2000: **Cosmic: a universal, DNA-based language for communicating with aliens and other intelligent lifeforms**
Speaker: Dr. J. P. L. Cox

22 November 2000: **Synthesis of Novel Dendrimers and Hyper Branched Polymers**
Speaker: Dr. W. Haynes

6 December 2000: **Dual Activation Approaches to Electroanalysis: Ultrasound, Microwaves and Laser Activation**
Speaker: Dr. R. Compton

24 January 2001: **Chemical Integrated Circuits: organic synthesis and analysis on a small scale**
Speaker: Dr. A. de Mello

21 February 2001: **Liquid Crystals of All Shapes and Sizes**
Speaker: Professor R. Richardson

28 February 2001: **Modelling Meso- and Molecular Scale Interactions in Polymeric Systems**
Speaker: Professor A. Balazs

30 April 2001: **The Effect of Flexibility on the Phase Diagram of Simple Molecular Models**
Speaker: Dr. C. Vega

14 June 2001: **Conjugated Rigid-Rods as Multifunctional Materials: Applications in Photonics and Molecular and Nanoscale Electronics**
Speaker: Professor T. Marder

14 November 2001: **Supermolecular liquid crystals multipodes and dendrimers**

Speaker: Prof. J. W. Goodby

23 January 2002: **Polymers as building blocks in nanotechnology**

Speaker: Dr. W. Huck

20 March 2002: **Simple and Complex Fluids Under Extreme Confinement**

Speaker: Prof. J. Klein

8 May 2002: **Covalent Effects in 'Ionic' Systems**

Speaker: Prof. P. Madden

30 October 2002: **Enzymes in Aromatic Degradation**

Speaker: Prof. T. Bugg

6 November 2002: **Modelling large uncrystallisable protein structures using X-ray and neutron scattering**

Speaker: Prof. S. Perkins

15 January 2003: **Planned and unplanned routes to bio-active target molecules**

Speaker: Prof. P. Bailey

5 February 2003: **Acetylenes in the Design of Phthalocyanine Analogues and Phenanthroline-based Ligand Systems**

Speaker: Dr. R. Faust

19 March 2003: **Polymer materials in tissue engineering**

Speaker: Prof. K. Shakesheff

25 June 2003: **Durham 3rd Year Postgraduate Symposia: Session 1**

2 July 2003: **Durham 3rd Year Postgraduate Symposia: Session 2**

9 July 2003: **Durham 3rd Year Postgraduate Symposia: Session 3**

B.4 Publications

[1] D. J. Earl, J. Ilnytskyi and M. R. Wilson, Computer simulations of soft repulsive spherocylinders, *Mol. Phys.* **99**, 1719 (2001)

[2] M. R. Wilson and D. J. Earl, Calculating the helical twisting power of chiral dopants, *J. Mater. Chem.* **11**, 2672 (2001)

[3] M. Solymosi, R. J. Low, M. Grayson, M. P. Neal, M. R. Wilson and D. J. Earl, Scaled chiral indices for ferroelectric liquid crystals, *Ferroelectrics* **277**, 483 (2002)

[4] M. P. Neal, M. Solymosi, M. R. Wilson and D. J. Earl, Helical twisting power and scaled chiral indices, *J. Chem. Phys.* **119**, 3567 (2003)

[5] D. J. Earl and M. R. Wilson, Predictions of molecular chirality and helical twisting powers, accepted for publication in *J. Chem. Phys.* (2003)